Thermal and Structural Response Modeling of a Woven Thermal Protection System

by

David Z. Dang

A dissertation submitted in partial fulfillment
of the requirements for the degree of
Doctor of Philosophy
(Aerospace Engineering and Scientific Computing)
in The University of Michigan
2021

Doctoral Committee:

> Professor Carlos E. S. Cesnik, Chair
> Adjunct Professor Iain D. Boyd
> Associate Professor Karthik Duraisamy
> Associate Professor Eric Johnsen
> Dr. Eric C. Stern

David Z. Dang

dzdang@umich.edu

ORCID iD: 0000-0001-5685-7271

To my son Noah

ACKNOWLEDGEMENTS

I am grateful for the guidance that I received throughout my time at the University of Michigan. First and foremost, I would like to acknowledge my Ph.D. researcher adviser and NASA mentor, Prof. Iain Boyd and Dr. Eric Stern, respectively. Prof. Boyd has been supportive of my academic and research pursuits throughout my entire graduate studies, and his guidance has truly been exceptional. Dr. Stern, a research scientist at NASA Ames Research Center, has provided unparalleled insight and motivation for the research conducted throughout my studies. I am also grateful for my other committee members, Profs. Carlos Cesnik, Karthik Duraisamy, and Eric Johnsen for taking the time to serve on my committee.

I am truly grateful to have been awarded a NASA Space Technology Research Fellowship (NSTRF) under Grant No. NNX16AM92H, which has funded me in full since September 2016. The NSTRF has allowed yearly extended visits to NASA centers and access to the experts in the atmospheric entry community. Throughout these visits and contacts, I have been assisted by numerous NASA personnel. I would specifically like to acknowledge Keith Petersen, Dr. Milad Mahzari, and Carl Poteet of the Heatshield for Extreme Entry Environment Technology (HEEET) team at NASA Ames and Langley Research Centers, respectively. These two individuals provided me with the necessary experimental datasets for assessing the simulation models in my research, and provided much-needed insight into the characteristics of the experiments modeled in this work. I would also like to acknowledge the entire Icarus team at NASA Ames, specifically, Drs. Justin Haskins, Joseph Schulz, and

TABLE OF CONTENTS

LIST OF FIGURES

Figure

LIST OF TABLES

ABSTRACT

NASA's future missions include destinations such as Venus, Saturn, and Jupiter, where the heat-intensive environments experienced during atmospheric entry by vehicles or probes often exceed the capability of conventional Thermal Protection System (TPS) materials (e.g., Phenolic Impregnated Carbon Ablator (PICA), Heritage Carbon Phenolic (HCP)). The Woven Thermal Protection System (WTPS), a relatively new concept of ablative TPS design, has been of key interest in the past decade to replace heritage materials. In the design of TPS, characterizing the material's thermal and structural performance is critical. The focus of this dissertation is on improving the modeling of WTPS, in particular, the Heatshield for Extreme Entry Environment Technology (HEEET), a dual layer WTPS composed of an outer recession-resistant layer and inner insulative layer.

The results focus on three aspects. The first aspect is focused on pure thermal response modeling of HEEET in a radiant heating facility. The simulation results are compared to experimental measurements, and improved material and boundary condition models are derived based on the analyses.

The second aspect is focused on pure structural response modeling of the 24 in. HEEET weave under four point bend mechanical loading. The model is assessed using experimental measurements. Initial simulations are performed using stiffness properties derived from a smaller HEEET weave at room temperature. Comparisons between the experimental measurements and simulation results for deformation indicate that the 24 in. recession layer is 130% stiffer than the smaller weave.

The last aspect is focused on coupled thermo-structural response modeling of

HEEET subject to combined mechanical and thermal loading. Discrepancies between simulation predictions and experimental measurements of deformation suggest that significant stiffness degradation is occurring. The subsequent stiffness degradation studies indicate that the stiffness of HEEET is monotonically decreasing in the temperature range being modeled. When using the inferred stiffness reduction factors for coupled thermo-structural modeling, the predictions for strain are in much closer agreement with experimental measurements. Limitations of the studies are discussed, which motivate the need for higher-fidelity experimental tests that can be used to deduce improved models.

CHAPTER I

Introduction

In recent decades, the operation of hypersonic vehicles and atmospheric entry probes has prompted the interests of engineers and scientists worldwide. Hypersonic flight, typically defined as vehicles moving at at least five times the speed of sound, can occur within (e.g., re-entry capsules, hypersonic aircraft, cruise missiles) or out of the Earth's atmosphere (e.g., atmospheric entry probes, surface landers).

For planetary exploration and reentry missions, hypersonic entry probes are ubiquitously used, and entry speeds surpassing 13 m/s is common to planets such as Venus and Saturn. When these probes enter a planetary atmosphere, there exist numerous physicochemical phenomena in the flowfield, on the surface of the vehicle, and in-depth of the material that protects the vehicle.

In the flowfield, a bow shock forms around the frontal region of the vehicle during entry as shown in Fig. 1.1. The temperature behind the shock increases due to the conversion of kinetic to internal energy and may exceed 10,000 K, activating several chemical reactions such as dissociation and ionization. While a significant portion of this thermal energy is convectively dissipated, the remaining energy is incident on the surface of the vehicle, resulting in a chemically reacting boundary layer and multiple surface chemistry processes (e.g., catalysis, oxidation, nitridation), as well as in-depth physicochemical phenomena (e.g., material decomposition, thermal conduction). The

extreme heat environments produced during entry require a well-designed Thermal Protection System (TPS) to shield the vehicle and ensure mission safety.
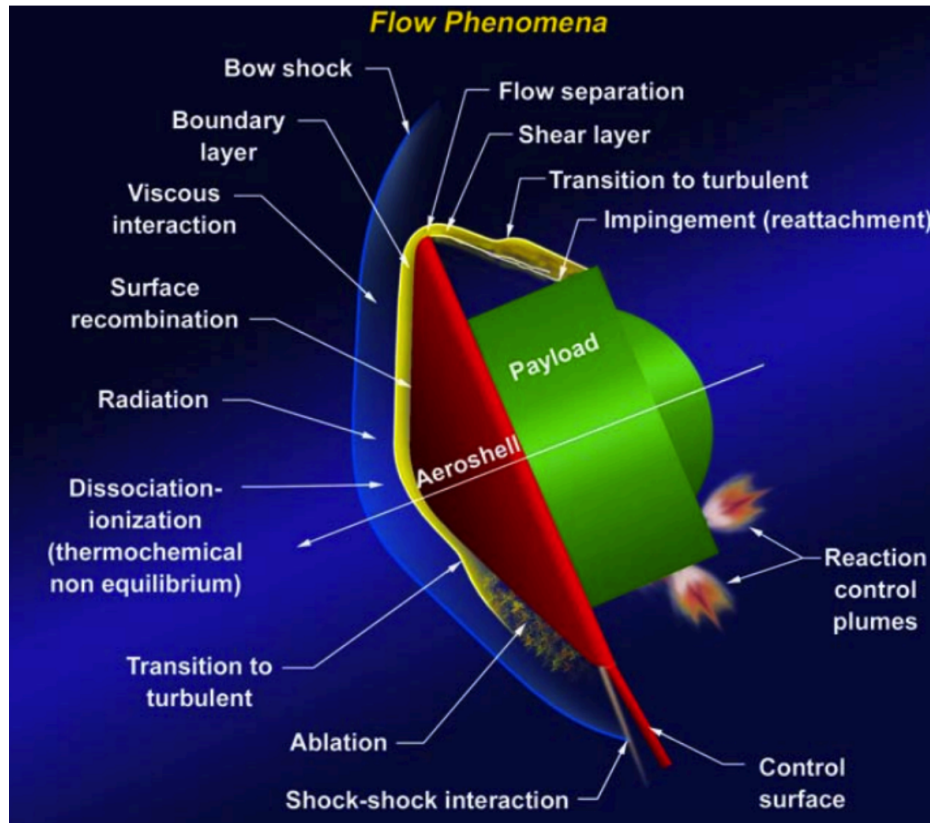
Figure 1.1: Flowfield phenomena during atmospheric entry [1].

Figure 1.2 shows the range of peak heat fluxes encountered in past NASA missions [2]. The vertical axis uses a logarithmic scale. The relatively milder environments include the Mars Viking, which experienced a peak heat flux of approximately 25 $\frac{W}{cm^2}$, and the most extreme missions include the Galileo Probe, which experienced a peak heat flux over 10 times that of the Mars Viking. Generally, a Venus, Jupiter, and Saturn mission will experience a substantially higher heat flux than a Mars or re-entry mission.
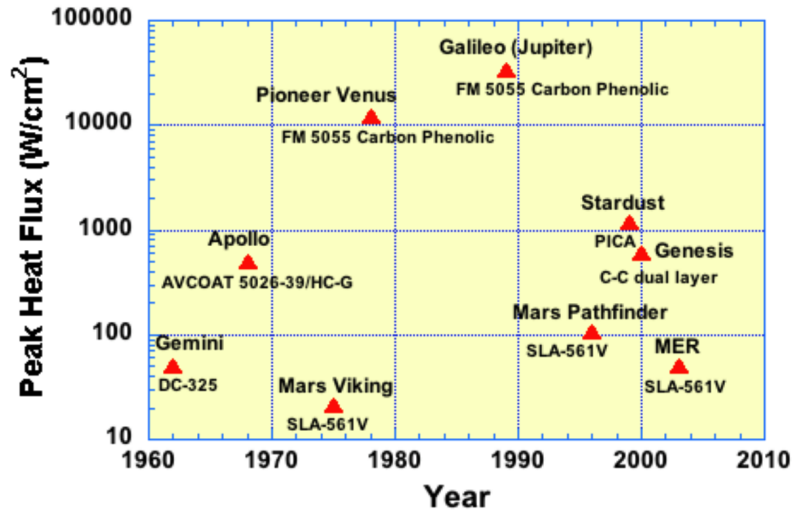
Figure 1.2: Range of peak heat flux for NASA enty missions [2].

1.1 Thermal Protecion System

The TPS is a critical insulative component in many heat-intensive environments, particularly in aerothermal heating scenarios encountered during atmospheric entry, to ensure the integrity of the underlying structure and scientific measurement instruments. It is critical for the performance of TPS to be validated through fight tests, ground tests, and simulation models as it is a single point of failure component. Actual flight testing is the most accurate testing, but it is prohibitively costly, so it is typically not used.

TPS materials can be classified as either ablative or non-ablative [8]. The former class of TPS materials is typically used in extreme conditions and the latter in comparatively more benign environments. The primary energy accommodation mechanisms of both classes of TPS are shown in Figs. 1.3 and 1.4.

Non-ablative, also commonly regarded as "reusable," TPS materials include ceramic tiles, which were used on the Space Shuttle. As shown in Fig. 1.3, a portion of the incident convective heat flux is re-radiated from the heated surface with the remainder conducted into the TPS material. For reusable materials, a high emissivity

3
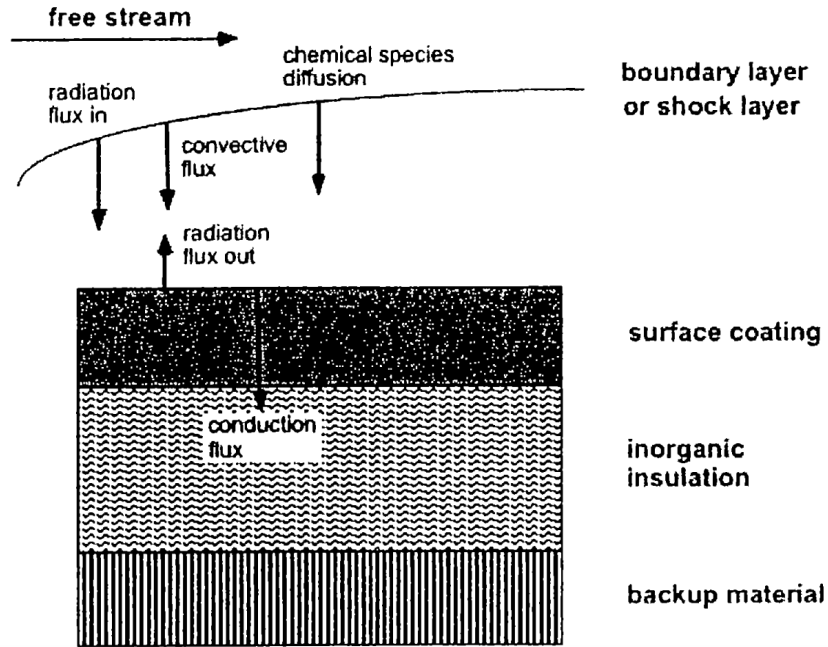
Figure 1.3: Energy transfer mechanisms of reusable TPS [2].
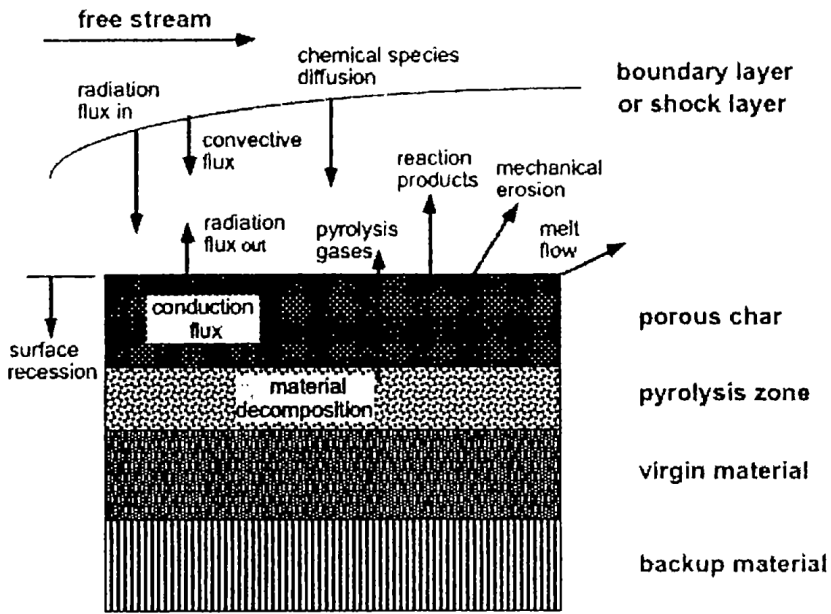
Figure 1.4: Energy transfer mechanisms of ablative TPS [2].

surface coating over the underlying TPS is desired to increase the re-radiated energy and thereby reduce the amount of energy transferred to the vehicle. Low surface

catalycity and thermal conductivity is also desired to minimize the convective and conductive heat transfer, respectively. In addition, a low thermal conductivity TPS material typically results in improved mass efficiency as the TPS does not need to be as thick compared to a higher thermal conductivity material.

In contrast, ablative TPS materials are used in relatively more intense environments and have been the approach to TPS design for all NASA planetary entry probes [2]. The focus of this work is on ablative TPS, specifically decomposing (or pyrolyzing) ablators. Decomposing ablators such as the PICA is a well-studied ablative TPS material and has been successfully employed on missions such as Stardust and the Mars Science Laboratory [9; 10]. PICA was invented at the NASA Ames Research Center in the 1990s [11]. PICA is composed of a low density rigid carbon fiber porous preform that is impregnated with phenolic resin [11]. High temperature curing of the impregnated composite yields a lightweight highly porous material.

Similar to reusable TPS, the convective heat transfer to an ablative TPS induces high surface and in-depth temperatures. However, for ablative TPS, the differentiation is that the temperature increase results in phase changes and thermochemical removal of material from the surface [8], which provide the desired relief of heat load to the in-depth material and the underlying vehicle. For pyrolyzing ablators such as PICA, the phenolic resin decomposes internally (typically endothermically) and produces pyrolysis gas, which flows through the pores of the TPS into the boundary layer, as shown in Fig. 1.4, displacing the hot boundary layer gases away from the vehicle, reducing the convective heat transfer. As the pyrolysis gases flow toward the surface, they are heated by the surrounding internal substructure, and this additional energy transfer phenomenon results in a reduction in the temperature of the substructure. The fully pyrolyzed region of the TPS material is typically referred to as the "char" layer. The creation of this char layer serves as an effective insulator and blocker for radiated heat from the shock layer.

Surface processes, between the TPS material and boundary layer gases, such as endothermic reactions in sublimation and vaporization and exothermic reactions in oxidation and nitridation are also key mechanisms involved in ablative TPS [12; 13; 14]. These processes typically result in surface recession and are fundamental considerations in a wide variety of ablative TPS designs to protect the vehicle from severe heating. Comparatively, the collective set of internal and surface processes of ablative TPS is much more complex than that of reusable TPS, resulting in a substantially more challenging design and validation process.

In addition to the thermal in-depth phenomena, structural effects are also important. Processes such as spallation, cracking, stiffness degradation, and TPS deformation may contribute to mechanical failure or influence thermal performance due to the multi-physics coupling.

While missions such as Stardust and the Mars Science Laboratory have certified the maturity of PICA, NASA's future space exploration missions exceed the performance capabilities of PICA [4]. In the past, fully-dense Carbon Phenolic (CP) was used for extreme entries [15]; however, its high density and thermal conductivity limit such TPS to steep entries, high heat fluxes and pressures, and short entry durations [4]. These limitations pose numerous challenges in certifying the use of Heritage Carbon Phenolic (HCP) in current testing facilities. At shallower entries, HCP is not a feasible alternative, especially when mass efficiency is critical [4]. These obstacles prompted the investigation of alternative ablative TPS concepts that could be tailored to a specific mission, as well as be more sustainable. Among those, 3-D Woven Thermal Protection System (WTPS) has gained interest due to promising results in its design flexibility, and thermal and mass performance, compared with that of heritage technologies [4].

1.2 Mission-specific challenges

The Galileo probe to Jupiter used fully dense carbon phenolic, which is a very conservative approach to TPS design. For steeper entries to Jupiter and, consequently, greater entry velocities (e.g., approximately 55 km/s at 30 deg latitude [2]), the heating rates experienced during entry is expected to exceed the capability of fully dense carbon phenolic TPS used for Galileo. The mass-inefficiency from using fully dense carbon phenolic also results in little mass for science [2].

The Pioneer Venus multiprobe used carbon cloth derived from a specific rayon fabrice produced in the 1970s [2]. This poses a unique challenge as the heritage material is no longer available. While the fully dense carbon phenolic used for Galileo is a potential alternative for Venus missions, it is not a favorable one as it would impose a significant TPS mass penalty [2].

WTPS is a more favorable alternative as it offers tailorability for specific mission scenarios, a characteristic not exhibited by heritage material.

1.3 Woven Thermal Protection Systems

WTPS is typically composed of carbon, silica, and/or phenolic yarns that are arranged using commercially available precisely engineered weaving techniques (Fig. 1.6), with a 3-D or planar architecture. The architecture and material composition of a WTPS may be precisely tailored to meet the requirements of a specific mission. The material can be used in a dry configuration or may be resin-infused for more demanding applications where the benefits of a pyrolyzing ablator are desired. In addition, different densities can be achieved by varying the weave and amount of resin infusion. The tailorability of the material allows the control of many physical variables such as density. Figure 1.5 shows the density for several variations of WTPS and other classical and heritage TPS materials. Unlike fully dense carbon phenolic

and PICA, WTPS encompasses a large range of densities, with the fully dense WTPS exhibiting a density comparable to that of fully dense carbon phenolic and the dry configuration exhibiting a density comparable to that of PICA.
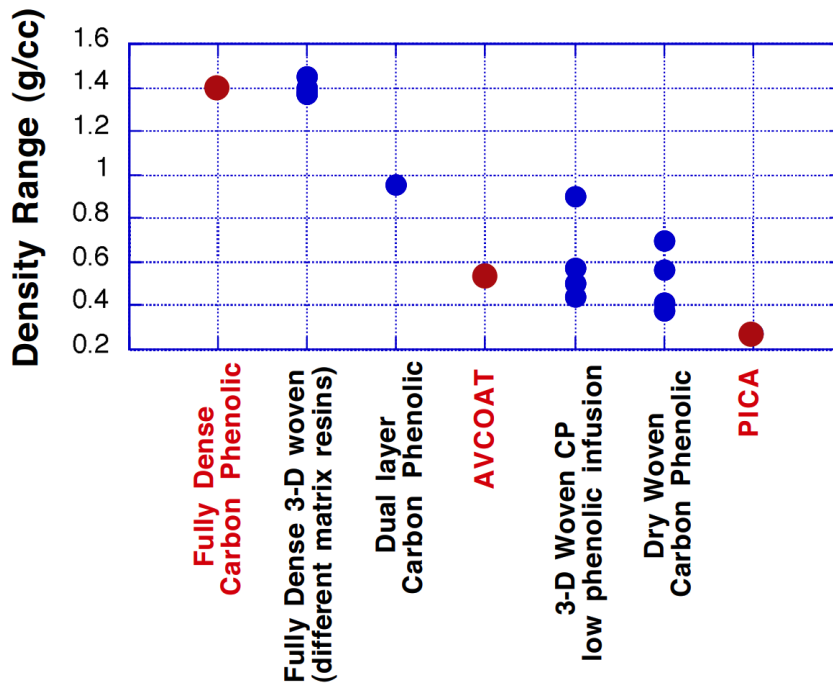
Figure 1.5: Densities of TPS materials [3].

The general manufacturing process for WTPS is shown in Fig. 1.7. Generally, there are two 3-D weave configurations employed for WTPS, a 3-D layer-to-layer weave or a 3-D orthogonal weave. These configurations are shown in Fig. 1.8. The layer-to-layer configuration weaves each layer to the subsequent layer below. The process limits thermal conduction and stiffness in the Through the Thickness (TTT)- or Z-direction. The 3-D orthogonal configuration weaves each fiber through all layers, resulting in comparatively larger TTT stiffness and thermal conductivity.

Multiple experimental studies have been conducted on these materials in facilities such as arc jets, radiant heating facilities, and various other test environments [7]. To date, there has been very limited modeling work conducted for these materials. In order to fully leverage the flexibility of these materials, modeling capabilities specific
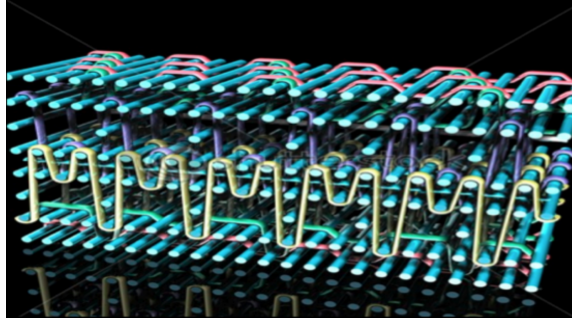
Figure 1.6: Schematic of 3-D WTPS [4].
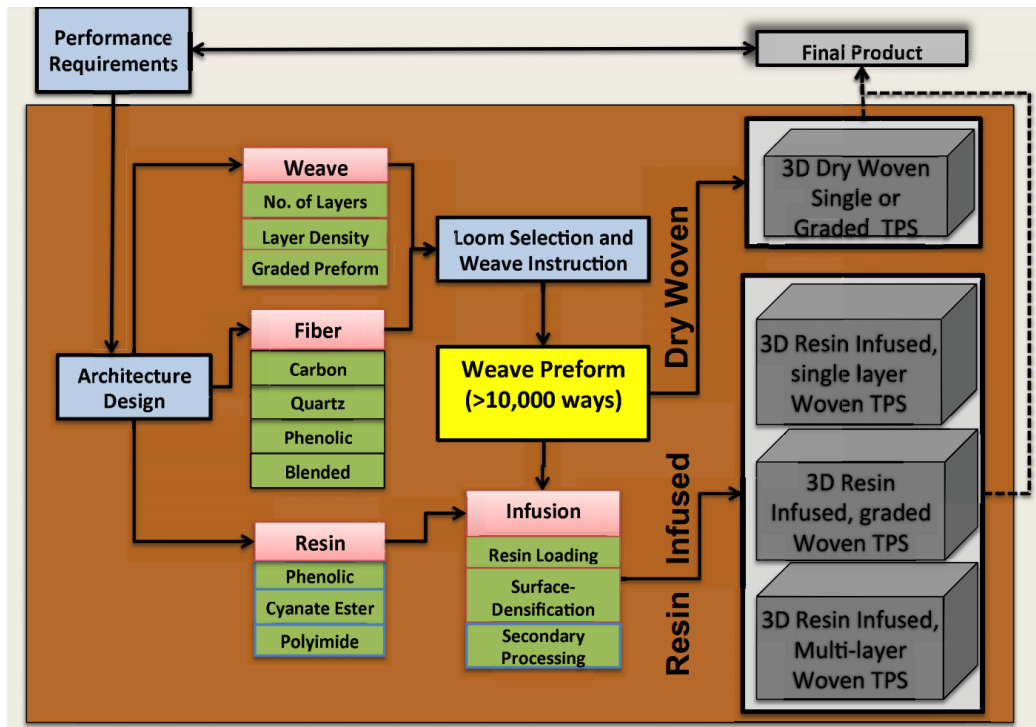
Figure 1.7: Manufacturing process flow for WTPS [3].
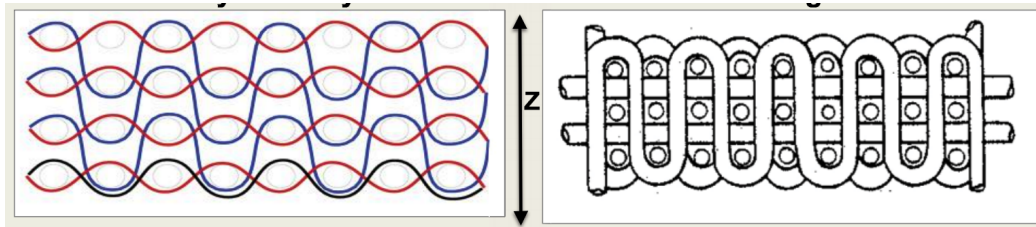
Figure 1.8: 3-D weave configurations [3].

to the woven architecture should be developed to provide insight into the material performance and optimization involved. This is an essential requirement to optimally

deploy WTPS for a specific mission.

The Adaptive Deployable Entry Placement Technology (ADEPT) [5], Heatshield for Extreme Entry Environment Technology (HEEET) [4; 7; 16], and 3D-Multifunctional Ablative TPS (3D-MAT) [3] are three current NASA technology development efforts intended to leverage the promising potential of WTPS.

The ADEPT is a mechanical deployable semi-grid umbrella-like aeroshell entry system consisting of a series of deployable ribs and struts, which are connected by a flexible woven carbon fabric skin [5]. This skin serves as the primary thermal protection component of the TPS [5]. Figure 1.9 shows the three main configurations of ADEPT: stowed (during launch), deployed (during aerocapture and entry), and landing. The flexible WTPS material is folded and stretched in the stowed and stretched configurations, respectively. During the high heat load experienced during the aerocapture, entry, and descent phases, the skin is kept in tension to provide the desired thermal protection. Larger variations of the ADEPT framework, as well as "nano-ADEPT," are currently expected to be used for landing heavier and lighter payloads at Mars and Venus and other destinations.
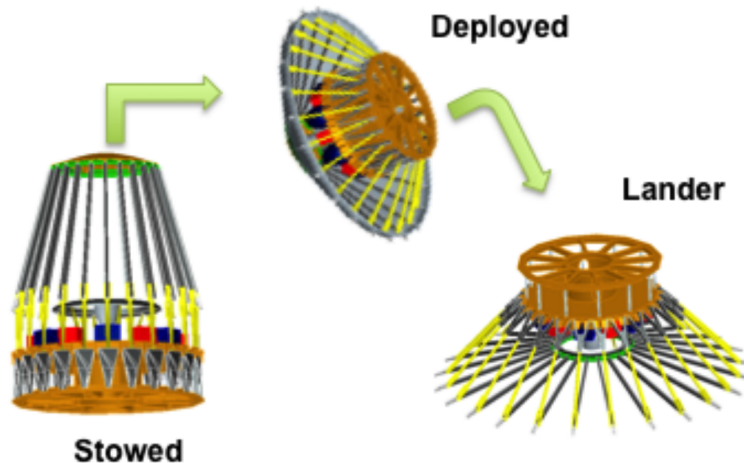
Figure 1.9: Stowed, Deployed, and Lander Configurations of ADEPT [5].

The 3D-MAT is another WTPS [3] and is shown in Fig. 1.10. However, unlike

HEEET and ADEPT, 3D-MAT uses fibers made of quartz rather than carbon. 3D-MAT is currently tailored for the Orion Space Capsule compression pads. Previous TPS materials did not simultaneously meet the structural and thermal integrity desired for the compression pads. Instead, 3D-MAT uses an orthotropic woven quartz material from Bally Ribbon Mills along with resin transfer molding, which satisfy the requirements needed for the compression pads.

Figure 1.10: Flight compression pad made from 3D-MAT [3].

The HEEET is the last of the three referenced NASA technologies that make use of WTPS, and it is the focus of this work. HEEET is designed for planetary exploration missions with more thermally taxing atmospheric entry environments (e.g., Saturn, Venus, Uranus) and has emerged as a replacement for CP. The Mars Sample Return mission [17] is one of the well known applications of HEEET. The 3-D dual-layer HEEET architecture, shown in Fig. 1.12, is composed of two layers. The outer layer is designed to be recession-resistant and is made from a fine, dense weave of carbon yarns. The inner layer is a low density insulating layer, and consists of a blend of carbon and phenolic materials. Both of these layers are infused with low density phenolic resin that fills the pores of the woven substructure, resulting in a rigid TPS. The layers are mechanically interlocked together multi-dimensionally

to construct the overall WTPS [7]. The weaving operation of HEEET is shown in Fig. 1.11. The dual-layer nature further enables the customization of each layer's thickness for specific mission scenarios. For example, for missions where recession is expected to be minimal, a thinner recession layer can be used, and vice versa. HEEET is anticipated to be about 40% more mass efficient than HCP while maintaining the favorable characteristics of a dense TPS [3].
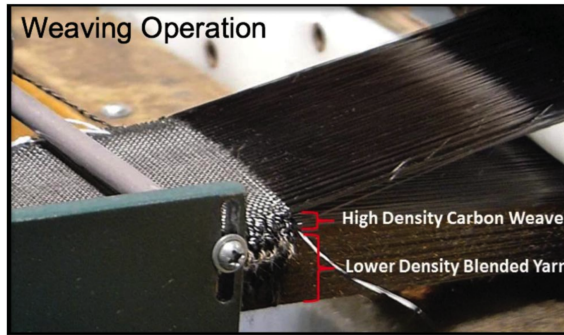
Figure 1.11: Weaving operation of HEEET [6].
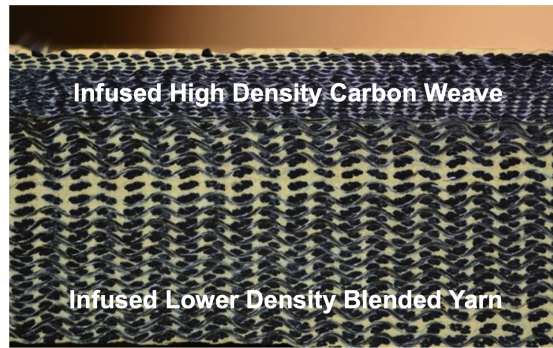
Figure 1.12: HEEET 3-D weave cross-section [7].

HEEET is considered to be a mid-density material. Both layers are of lower density, thermal conductivity, and thermal diffusivity compared to HCP [6]. Room temperature material properties for HEEET and HCP can be found in Table 1 of Ref. [6].

Currently, the HEEET ablator is limited to tiles no longer than 24 in, due to manufacturing limitations. To construct a larger heatshield using HEEET material,

a tiled approach is needed, where each tile is bonded to neighboring tiles. When the tiles are bonded, considerable bond stresses are generated in the bonds between tiles, necessitating the use of softer gap-fillers. These gap-fillers are softened HEEET material manufactured from mechanically conditioning the acreage HEEET material.

1.4   Motivation

In the development cycle of viable TPS, there are two critical components: high enthalpy testing facilities and computational models. Experimental facilities such as arc jets, vacuum chambers, shock tubes, among others, are frequently used for testing. Arc jets typically provide the most representative environment for simulating supersonic, high enthalpy flow. While arc jets can provide a viable experimental model for some realistic TPS flight environments, its inability to generate a combined convective and radiative heating environment is one of its notable limitations. Similar limitations in the ability to generate multiple physicochemical phenomena simultaneously exist for other experimental facilities as well. Comparatively, computational models are less limited and much cheaper; however, in order to gain confidence in the models, their validity must be established. Validity in the current context means that the model is accurately representing physicochemical processes. The process is challenging, as there are not only many uncertainties in the inputs into the models (e.g., material properties, free stream conditions, boundary conditions), but also the appropriateness of the models in accurately capturing physical phenomena (e.g., surface reaction, pyrolysis gas transport, phenolic resin decomposition models).

Historically, to aid the development process of TPS, multiple modeling tools have been developed that focus on thermal and structural response modeling [18; 19; 20; 21] of the TPS material, as well as flowfield modeling using Computational Fluid Dynamics (CFD) codes such as LeMANS, DPLR, and US3D [22; 23; 24] and gas-surface interaction analysis of the TPS. Ground testing is expensive and limited in

its ability to model multiple processes simultaneously, and often times, simulation models are an effective alternative and tool for analysis and design.

In the context of atmospheric entry, CFD codes generally involve additional components not present in traditional within-the-atmosphere CFD modeling. These components are typically related to chemically reacting gases and thermochemical nonequilibrium. CFD codes, when coupled with surface chemistry models and material response codes, provide a powerful tool for analyzing all critical physicochemical components of TPS performance simultaneously. The term "material response code" has been adopted by the TPS community to refer simulation software that models the material's response to the given boundary conditions, with boundary conditions determined from CFD or surface chemistry codes.

Improvements in the computational models are ongoing areas of interest. Many of these efforts have been focused on improving the physical models through the addition of linear or nonlinear terms to classical governing equations (e.g., transient heat conduction, Navier Stokes, continuity equations) or coupling multi-physics simulation models such as in this dissertation. While improvements in physical models are imperative in increasing the predictive capability, these models are still limited by uncertainties and inaccuracies in input parameters, particularly in the material properties. This work seeks to make advancements in both of these areas through coupled multi-physics modeling, as well as inference of material properties.

In this work, reduced-order models in Icarus, a 3-D finite volume material response code under development at the NASA Ames Research Center, [25] are used for modeling material decomposition resulting from the decomposition of the virgin material into gaseous and solid species. A new finite volume elasticity solver is developed as part of this work and coupled to Icarus to model combined thermo-structural phenomena. These simulation codes are applied to HEEET to infer material properties.

For HEEET, the interaction between thermochemical and structural phenomena is

not well-understood. Previous modeling efforts, such as [26; 27], focused on isotropic thermo-structural phenomena for non-woven materials. The current work focuses on the structural, thermal, and coupled thermo-structural response modeling of TPS, tailored specifically for modeling WTPS, to better guide design and experimental testing efforts with higher fidelity predictive capability for materials with directional-dependent properties. The higher level motivation of this thesis is to contribute to future space exploration missions.

There are several unique contributions of the research performed in increasing the fidelity of TPS, specifically HEEET, modeling. First, a temperature-dependent thermal conductivity model is derived using inference based on experimental results and simulation predictions. Next, a room temperature stiffness model is derived for a HEEET weave with no previously known properties. Finally, a stiffness degradation model of HEEET is derived using experimental results and simulation predictions that show stiffness monotonically decreasing as a function of temperature in the temperature range of interest.

1.5 Dissertation Overview

This dissertation is composed of seven chapters. The next two chapters are focused on a detailed presentation of the thermal and structural models used for modeling TPS, the underlying numerical methods used for discretizing the partial differential equation (PDE)-based models, as well as verification and convergence tests of the models. This is followed by three chapters focused on the structural, thermal, and coupled thermo-structural modeling of a HEEET experiment conducted in the Laser Hardened Materials Environmental Laboratory (LHMEL) at Wright Patterson Airforce Base. The final chapter concludes with a summary of the results presented throughout this thesis, as well as a discussion of future work in this space.

CHAPTER II

Mathematical Model and Discretization

In this chapter, the mathematical model and numerical discretization are presented for the thermal and structural analysis of TPSs. First, the structural model for a homogeneous, anisotropic, elastic solid is presented. The governing structural partial differential equations (PDEs) are introduced along with their constitutive relations for elastic materials and small displacements. This is followed by a description of the numerical discretization methods used in the development of a linear elasticity solver as part of this thesis.

Afterwards, a presentation of the mathematical model and numerical discretization is provided for the thermal response analysis of the HEEET. The thermal response analysis is performed using Icarus, a 3-D material response code under development at the NASA Ames Research Center [25]. Icarus uses an unstructured finite-volume discretization of the conservation equations governing the in-depth heat transfer and solid material decomposition within a decomposing material. The remaining subsections detail thermodynamic relationships between state variables and the boundary condition, as well as a brief description of the numerics.

The chapter concludes with a description of the quasi-steady thermo-structural coupling implemented, and the validity of the quasi-steady assumption for the modeling conducted.

2.1 Structural Response Modeling

The governing structural PDEs are introduced along with their constitutive relations for elastic materials and small displacements. The assumption that WTPS materials behave elastically and linearly is an adequate assumption based on tensile testing and small deformations expected during usage.

A focus of this work is developing and coupling an in-house linear elasticity solver to a thermal response solver. To that end, the linear elasticity solver presented here is implemented within the Icarus framework. Icarus is a 3-D finite volume material response code developed at NASA Ames Research Center [25].

2.1.1 Governing Equations

The governing equations for a solid body in motion is the hyperbolic PDE

$$\frac{\partial^2(\rho_s \boldsymbol{u})}{\partial t^2} - \nabla \cdot \boldsymbol{\sigma} = \boldsymbol{F} \tag{2.1}$$

where ρ_s, $\boldsymbol{u}$, and $\boldsymbol{\sigma}$ represent the solid density, displacement vector, and second-order stress tensor, respectively. The right hand side is the body force vector per unit volume, i.e., a source term, and the left hand side is the summation of the acceleration and divergence terms. Fundamentally, these equations, known as the equations of motion, can be derived from a balance of momentum in the three cartesian directions.

Absent of acceleration, as for all TPS modeling performed here, the governing equations reduce to the elliptic set of PDEs

$$-\nabla \cdot \boldsymbol{\sigma} = \boldsymbol{F} \tag{2.2}$$

These governing equations form the classical set of "equilibrium equations" routinely used in the structural mechanics and thermo-structural community. The governing PDEs are closed by the constitutive equation and strain-displacement rela-

tionship:

$$\boldsymbol{\sigma} = \boldsymbol{C} : \boldsymbol{\epsilon} \tag{2.3}$$

$$\boldsymbol{\epsilon} = \frac{1}{2} \left[\nabla \boldsymbol{u} + (\nabla \boldsymbol{u})^T \right] \tag{2.4}$$

where $\boldsymbol{C}$ and $\boldsymbol{\epsilon}$ are the fourth-order stiffness and second-order strain tensors, respectively. The former equation is the generalized Hooke's law relating the unknown stresses and strains for elastic materials. The latter equation is the linear strain-displacement relationship under the assumption of small deformations. By taking advantage of the symmetry of the stress and strain tensors, Eq. (2.3) can be conveniently written using Voigt notation as

$$\boldsymbol{\sigma}' = \boldsymbol{C}' \boldsymbol{\epsilon}' \tag{2.5}$$

where the symmetric second-order tensors, $\boldsymbol{\sigma}$ and $\boldsymbol{\epsilon}$, are cast as first-order tensors, $\boldsymbol{\sigma}'$ and $\boldsymbol{\epsilon}'$, for memory and computational efficiency

$$\boldsymbol{\sigma}' = \begin{bmatrix} \sigma_{xx} & \sigma_{yy} & \sigma_{zz} & \sigma_{yz} & \sigma_{xz} & \sigma_{xy} \end{bmatrix}^T \tag{2.6}$$

$$\boldsymbol{\epsilon}' = \begin{bmatrix} \epsilon_{xx} & \epsilon_{yy} & \epsilon_{zz} & 2\epsilon_{yz} & 2\epsilon_{xz} & 2\epsilon_{xy} \end{bmatrix}^T \tag{2.7}$$

and the fourth-order stiffness tensor, $\boldsymbol{C}$, is reduced to a second-order tensor, $\boldsymbol{C}'$

18

$$
\boldsymbol{C}' =
\begin{bmatrix}
C_{11} & C_{12} & C_{13} & C_{14} & C_{15} & C_{16} \\
C_{21} & C_{22} & C_{23} & C_{24} & C_{25} & C_{26} \\
C_{31} & C_{32} & C_{33} & C_{34} & C_{35} & C_{36} \\
C_{41} & C_{42} & C_{43} & C_{44} & C_{45} & C_{46} \\
C_{51} & C_{52} & C_{53} & C_{54} & C_{55} & C_{56} \\
C_{61} & C_{62} & C_{63} & C_{64} & C_{65} & C_{66}
\end{bmatrix}
\tag{2.8}
$$

The modeling performed here is focused on studying WTPS materials, which are generally orthotropic. For orthotropic materials, the symmetric stiffness tensor reduces to

$$
\boldsymbol{C}' =
\begin{bmatrix}
C_{11} & C_{12} & C_{13} & 0 & 0 & 0 \\
C_{21} & C_{22} & C_{23} & 0 & 0 & 0 \\
C_{31} & C_{32} & C_{33} & 0 & 0 & 0 \\
0 & 0 & 0 & C_{44} & 0 & 0 \\
0 & 0 & 0 & 0 & C_{55} & 0 \\
0 & 0 & 0 & 0 & 0 & C_{66}
\end{bmatrix}
\tag{2.9}
$$

$$
=
\begin{bmatrix}
\frac{1-\nu_{yz}\nu_{zy}}{E_y E_z \Delta} & \frac{\nu_{yx}+\nu_{yz}\nu_{zx}}{E_y E_z \Delta} & \frac{\nu_{zx}+\nu_{yx}\nu_{zy}}{E_y E_z \Delta} & 0 & 0 & 0 \\
\frac{\nu_{yx}+\nu_{yz}\nu_{zx}}{E_y E_z \Delta} & \frac{1-\nu_{xz}\nu_{zx}}{E_x E_z \Delta} & \frac{\nu_{zy}+\nu_{xy}\nu_{zx}}{E_x E_z \Delta} & 0 & 0 & 0 \\
\frac{\nu_{zx}+\nu_{yx}\nu_{zy}}{E_y E_z \Delta} & \frac{\nu_{zy}+\nu_{xy}\nu_{zx}}{E_x E_z \Delta} & \frac{1-\nu_{xy}\nu_{yx}}{E_x E_y \Delta} & 0 & 0 & 0 \\
0 & 0 & 0 & G_{yz} & 0 & 0 \\
0 & 0 & 0 & 0 & G_{xz} & 0 \\
0 & 0 & 0 & 0 & 0 & G_{xy}
\end{bmatrix}
\tag{2.10}
$$

$$\Delta = \frac{1 - \nu_{xy}\nu_{yx} - \nu_{yz}\nu_{zy} - \nu_{xz}\nu_{zx} - 2\nu_{yx}\nu_{zy}\nu_{xz}}{E_x E_y E_z} \qquad (2.11)$$

where ν_{ij} is the Poisson's ratio in the i-j direction. The double subscripts correspond to a contraction in the j-direction due to an extension in the i-direction. G_{ij} and E_i are the modulus of rigidity in the i-j direction and elasticity in the i-direction, respectively.

2.1.2 Numerics

The PDE in the preceding section is discretized using the Finite Volume Method (FVM) [28]. The integral form of Eq. (2.2) can be written as

$$-\iint_S (\boldsymbol{\sigma} \cdot \hat{\boldsymbol{n}})dA = \iiint_V \boldsymbol{F}dV \qquad (2.12)$$

where the divergence theorem is applied to yield the surface integral.

The volume integrals are approximated using the midpoint rule:

$$\iiint \phi dV \approx \phi_i V_i \qquad (2.13)$$

where ϕ represents an arbitrary conservative variable. The surface integral flux term is approximated by a sum of face flux contributions

$$\iint (\boldsymbol{\sigma} \cdot \hat{\boldsymbol{n}})dA \approx \sum_{f=1}^{N_f} \boldsymbol{\sigma}_f |A_f| \hat{n}_f \qquad (2.14)$$

where N_f is the number of faces for the cell being integrated over.

The face stresses are evaluated using Eq. (2.3), where the strain is evaluated at the face. This requires a formulation for the face gradients, which are computed using

weighted linear interpolation between the neighboring cell-centered gradients. The cell-centered gradients are computed using a weighted least squares approximation as it is a well-established and studied method and relatively simple and efficient to implement with approximately second order accuracy (second order accuracy is generally sufficent for TPS modeling[1]).

In the least squares approximation, the displacement field $\boldsymbol{u}(\boldsymbol{x}) = [u(\boldsymbol{x})\ v(\boldsymbol{x})\ w(\boldsymbol{x})]^T$ is represented with some feature mapping $\boldsymbol{\Phi} = \{\phi_i(\boldsymbol{x})\}_{i+1}^m$ given a dataset $\boldsymbol{D} = \{(\boldsymbol{x}_k, \boldsymbol{u}_k)\}_{k+1}^n$. Each component of the displacement vector is written as a linear combination of the feature functions. For example, the u-component is written as

$$u(\boldsymbol{x}) = \sum_{i=1}^m \beta_i^{(u)} \phi_i(\boldsymbol{x}) \tag{2.15}$$

where $\boldsymbol{\beta}^{(u)}$ is the vector of coefficients to be found using least squares. Analogous expressions exist for the components v and w of the displacement vector using the least squares coefficients, $\boldsymbol{\beta}^{(v)}$ and $\boldsymbol{\beta}^{(w)}$, respectively. Absent of mesh motion, the coefficients need to be computed only once and stored at the beginning of the simulation for computational efficiency.

The least squares solution can be written as

$$\boldsymbol{\beta}^{(u)} = (\boldsymbol{X}^T \boldsymbol{W} \boldsymbol{X})^{-1} \boldsymbol{X}^T \boldsymbol{W} \hat{\boldsymbol{u}} \tag{2.16}$$

where $\hat{\boldsymbol{u}} = [u_1\quad u_2\quad \cdots\quad u_n]^T$, the vector representing values for u in the dataset used for the least squares fit. The weighting matrix, $\boldsymbol{W}$, is positive definite where its main diagonal entries are the inverse distances between cells. $\boldsymbol{X}$, the feature matrix,

---

[1]D. Dang, private communication, January 2017

is defined as

$$
\boldsymbol{X} = \begin{bmatrix} \phi_1(\boldsymbol{x}_1) & \cdots & \phi_m(\boldsymbol{x}_1) \\ \vdots & \ddots & \vdots \\ \phi_1(\boldsymbol{x}_n) & \cdots & \phi_m(\boldsymbol{x}_n) \end{bmatrix} \tag{2.17}
$$

By taking the gradient of Eq.(2.15), the gradient formulation for the u-component can be written as

$$
\nabla u(\boldsymbol{x}) = (\boldsymbol{\beta}^{(u)})^T \nabla \boldsymbol{\Phi}(\boldsymbol{x}) \tag{2.18}
$$

and similarly for the v- and w-components. The displacement gradient tensor is therefore

$$
\nabla \boldsymbol{u}(\boldsymbol{x}) = \begin{bmatrix} \nabla u(\boldsymbol{x}) \\ \nabla v(\boldsymbol{x}) \\ \nabla w(\boldsymbol{x}) \end{bmatrix} = \begin{bmatrix} (\boldsymbol{\beta}^{(u)})^T \nabla \boldsymbol{\Phi}(\boldsymbol{x}) \\ (\boldsymbol{\beta}^{(v)})^T \nabla \boldsymbol{\Phi}(\boldsymbol{x}) \\ (\boldsymbol{\beta}^{(w)})^T \nabla \boldsymbol{\Phi}(\boldsymbol{x}) \end{bmatrix} = \begin{bmatrix} \boldsymbol{\beta}^{(u)} & \boldsymbol{\beta}^{(v)} & \boldsymbol{\beta}^{(w)} \end{bmatrix}^T \nabla \boldsymbol{\Phi}(\boldsymbol{x}) \tag{2.19}
$$

where it is compactly written in terms of the least squares coefficients and vectorized features.

The choice of features is dependent on the problem being modeled. A complete set of quadratic and linear features is implemented in the linear elasticity solver. These features corresponds to a second order Taylor series expansion of $u(x, y, z)$

$$
u(x, y, z) = \beta_0 + \beta_1 x + \beta_2 y + \beta_3 z + \beta_4 xy + \beta_5 xz + \beta_6 yz + \beta_7 x^2 + \beta_8 y^2 + \beta_9 z^2 + \xi \tag{2.20}
$$

resulting in the following set of features

22

$$\mathbf{\Phi} = \begin{bmatrix} 1 & x & y & z & xy & xz & yz & \frac{1}{2}x^2 & \frac{1}{2}y^2 & \frac{1}{2}z^2 \end{bmatrix}^T \qquad (2.21)$$

Note that the isosurfaces associated with these features are quadrics. The nonlinear features add little computational complexity and are included as it allows the gradient formulation to be a function of location, which is otherwise not possible with only the linear terms. The location dependence is particularly advantageous when computing face gradients at the boundaries, where Eq. (2.19) can be used simply with the boundary face centroid to compute the face gradient, rather than introducing an alternative formulation for the boundary face gradients or extrapolating the cell-centered gradient of the boundary cell.

2.1.3 Boundary Conditions

Three types of Boundary Conditions (BCs) are implemented in the linear elasticity solver: Dirichlet, Neumann, and Mixed. For structural modeling, these BCs correspond to specified displacement, traction, and both displacement and traction, respectively. The implementation for all three BCs relies on introducing a layer of ghost cells adjacent to the boundary cells of the real domain. This allows for extending the spatial discretization used on the interior cells to the boundary cells, but introduces the need for computing displacements in the ghost cells.

Dirichlet BCs are prescribed directly along the boundary faces such that

$$\boldsymbol{u}(\boldsymbol{x}) = \boldsymbol{u}_{BC}, \quad \boldsymbol{x} \in \Gamma_{\boldsymbol{u}} \qquad (2.22)$$

The most common structural Dirichlet BC is a fixed boundary, where $\boldsymbol{u}_{BC} = 0$. The Neumann BC assigns a specified traction over a portion of the surface

$$T(x) = T_{BC}, \quad x \in \Gamma_u \tag{2.23}$$

where the traction vector is defined as

$$T(x) = \sigma \hat{n} \tag{2.24}$$

The Neumann BC is prescribed at the boundary face of the boundary cell. For the Neumann BC, a layer of ghost cells is introduced in order to maintain the cell gradient discretization used for the interior cells. This also results in a discretization that maintains the spatial order of accuracy, which will be shown empirically to be second order accurate in the next chapter, of the interior cells at the boundary. To do so, an expression for the ghost cell displacements is derived as a function of the interior displacements and applied traction BC. This involves formulating a linear system by using the least squares formulation for gradients, Eq. (2.18), evaluated at the centroid of the boundary cell face, along with the traction-stress relationship, Eq. (2.23). For a given boundary cell with $\hat{N}$ Neumann faces, we can form the following system of equations

$$\begin{bmatrix} T_1 \\ \vdots \\ T_{\hat{N}} \end{bmatrix} = \begin{bmatrix} \sigma_1 \hat{n}_1 \\ \vdots \\ \sigma_{\hat{N}} \hat{n}_{\hat{N}} \end{bmatrix} \tag{2.25}$$

Note that the subscripts denote face values. After substituting in Eq. (2.3) for the stress variables on the right hand side and Eq. (2.18) for the face gradients and simplifying, the following system in terms of displacements is obtained

$$\boldsymbol{T}' = \begin{bmatrix} \boldsymbol{T}_1 & \cdots & \boldsymbol{T}_{\hat{N}} \end{bmatrix}^T = \boldsymbol{M}_{int}\boldsymbol{u}_{int} + \boldsymbol{M}_d\boldsymbol{u}_d + \boldsymbol{M}_n\boldsymbol{u}_n \qquad (2.26)$$

where the column vectors $\boldsymbol{u}_{int}$, $\boldsymbol{u}_d$, and $\boldsymbol{u}_n$ are the array of displacements for the interior, Dirichlet, and Neumann cells in the least squares stencil. The matrices M_{int}, M_d, and M_n store the coefficients for the interior, Dirichlet, and Neumann cell displacements, respectively, which are functions of the stiffness matrix and the weighted least squares parameters.

After rearranging such that all the unknowns are on the left hand side and the knowns on the right hand side, the following system of equations is obtained

$$\boldsymbol{u}_n = \underbrace{\boldsymbol{M}_n^{-1}\boldsymbol{T}' - \boldsymbol{M}_n^{-1}\boldsymbol{M}_d\boldsymbol{u}_d}_{\text{Contribution to } \boldsymbol{b}} - \underbrace{\boldsymbol{M}_n^{-1}\boldsymbol{M}_{int}\boldsymbol{u}_{int}}_{\text{Contribution to } \boldsymbol{A}} \qquad (2.27)$$

where the left hand side consists of the array of unknown displacement values in the ghost cells as a function of the right hand side. The first two terms on the right hand side contribute to the forcing vector, $\boldsymbol{b}$, and the last term contributes to the matrix, $\boldsymbol{A}$, in the linear system ($\boldsymbol{Ax} = \boldsymbol{b}$), respectively. Note that the contribution to $\boldsymbol{A}$ is independent of the magnitude of the prescribed traction BC.

The final BC implemented is the mixed BC, which prescribes a known traction and at least one displacement component at some part of the boundary. The implementation of the mixed BC combines the ideas enumerated in the former two BCs and will not be detailed here.

2.1.4 Sparse storage and iterative solver implementation

The discretization of the governing PDEs results in sparse matrices and vectors. The Portable, Extensible Toolkit for Scientific Computation (PETSc, [29]) library is

used for implementing sparse data storage and an iterative linear systems solver with preconditioning.

For the *elliptic* governing PDEs, Eq. (2.2), the geometric algebraic multigrid (GAMG) preconditioner is used due to its suitability for elliptic PDEs, as well as to significantly decrease convergence time by decreasing the condition number of the linear system. In order to optimize the efficiency of GAMG, the rigid body modes are created from the cell centroid coordinates. A global null space is created from the six rigid body modes (three translational and three rotational) for a pure Neumann problem so that the GAMG method can preserve the space on coarse grids, increasing its effectiveness and the overall efficiency of the preconditioner. The generalized minimal residual method (GMRES) is used to solve the preconditioned linear system.

Algorithm 1 shows an outline of the key steps in the linear elastic solver. The inputs of the solver are the mesh information (e.g., elemental size and location), $\boldsymbol{M}$, the dirichlet and Neumann boundary conditions, $\boldsymbol{u}_{BC}$ and $\boldsymbol{T}_{BC}$, and the material properties, $\boldsymbol{C}$.

Algorithm 1: linear_elastic_solve($\boldsymbol{M}, \boldsymbol{u}_{BC}, \boldsymbol{T}_{BC}, \boldsymbol{C}$)

1 initialize($\boldsymbol{u} \leftarrow 0, \boldsymbol{\epsilon} \leftarrow 0, \boldsymbol{\sigma} \leftarrow 0$)

2 for *each $c \in M.cells()$* **do**

3   c.compute_wlsq();

4 end

5 for *each $f \in M.facets()$* **do**

6   **for** *each $u \in f.\boldsymbol{u}$* **do**

7 $A \leftarrow$ u.contrib_diff_op(A, $\boldsymbol{C}$);

8 $b \leftarrow$ u.contrib_forcing(b, f.extract_bc($\boldsymbol{u}_{BC}, \boldsymbol{T}_{BC}$), $\boldsymbol{C}$);

9   **end**

10 end

11 create_rigid_body_modes($\boldsymbol{M}$)

12 // use geometric algebraic multigrid preconditioner

13 set_preconditioner(gamg)

14 $\boldsymbol{x} \leftarrow$ GMRES(A, b, tolerance = τ)

15 // extract displacement field solution for each cell c

16 for *each $c \in M.cells()$* **do**

17   c.$\boldsymbol{u}$.extract($\boldsymbol{x}$);

18 end

19 // use displacement field to construct stress and strain for each cell c

20 for *each $c \in M.cells()$* **do**

21   c.construct_strain();

22   c.construct_stress();

23 end

2.2   Thermal Response Model

In this section, the mathematical model is presented for the thermal response analysis of HEEET. The thermal response modeling is performed using Icarus. The subsequent subsections detail the governing equations, thermodynamic relationships between state variables, and the boundary conditions. Additional details of the governing equations and numerical discretization can be found in the manual for Icarus [25].

2.2.1   Governing Equations

2.2.1.1   Material Response Equations for a 3-D Woven TPS

For decomposing ablators such as HEEET, the decomposition of the TPS material is modeled using the Arrhenius rate equation [30]:

$$\frac{\partial \rho_{s,n}}{\partial t} = -k_n \rho_{v,n} \left(\frac{\rho_{s,n} - \rho_{c,n}}{\rho_{v,n}} \right)^{\psi_n} \exp\left(-\frac{T_{a,n}}{T} \right) \tag{2.28}$$

where $k_n, \psi_n, T_{a,n}$ are the Arrhenius reaction rate, pre-exponential, and activation temperature of the pyrolysis reaction for the n-th component of the material. $\rho_{s,n}$ is the density for the n-th component of the solid material. For HEEET, a three-component decomposition model is used. The solid decomposition model accounts for the endothermicity of the pyrolysis process.

The rate of decomposition of the solid material is proportional to the production of pyrolysis gases (i.e., a mass balance between the virgin material and decomposed solid and gas mixture). The rate of generation of the pyrolysis gases is defined as a linear combination of the rate of decomposition of the solid components

$$\dot{\omega} = \sum_{n=1}^{N} \Gamma_n \frac{\partial \rho_{s,n}}{\partial t} \tag{2.29}$$

where Γ_n is the initial pseudo-volume fraction of the n-th component of the virgin solid material. The products of the decomposition are assumed to be in local thermo-chemical equilibrium, reducing the number of products and thus governing equations.

The continuity equation for the pyrolysis gas is

$$\frac{\partial (\phi\rho_g)}{\partial t} + \frac{\partial}{\partial x_i}(\phi\rho_g u_{g,i}) = \dot{\omega} \tag{2.30}$$

where $\phi\rho_g$ is the product of the porosity and pyrolysis gas density or otherwise known as the bulk density of the pyrolysis gas. $u_{g,i}$ is the i-th component of the pyrolysis gas velocity and is modeled using Darcy's law [31; 32] for porous media

$$u_{g,i} = -\frac{1}{\mu}K_{ij}\frac{\partial p}{\partial x_j} \tag{2.31}$$

where μ and K_{ij} are the viscosity and permeability tensor, respectively. The 2-D permeability tensor is used because HEEET is an orthotropic material.

The energy conservation equation is the non-linear parabolic partial differential equation [30; 32]

$$\frac{\partial (\rho e)}{\partial t} + \frac{\partial}{\partial x_i}(\phi\rho_g h_g u_{g,i}) - \frac{\partial}{\partial x_i}\left(\kappa_{ij}\frac{\partial T}{\partial x_j}\right) = 0 \tag{2.32}$$

where e and ρ are the total energy and density, respectively. The second term describes the convective transport of the pyrolysis gas and is a function of the porosity of the solid material and pyrolysis gas variables. h_g is the pyrolysis gas enthalpy.

The total density is computed as

$$\rho = \phi\rho_g + \rho_s \tag{2.33}$$

where the solid density is computed using

$$\rho_s = \sum_{n=1,n_s} \Gamma_n \rho_{s,n} \tag{2.34}$$

2.2.2 Thermodynamic state variables

To close the set of governing equations, thermodynamic variable models are needed. The pressure of the pyrolysis gas is computed using the equation of state

$$p = \rho_g \frac{\mathcal{R}}{W_g} T \tag{2.35}$$

where T is the temperature of the solid and gas material under the assumption that the two are in thermal equilibrium. W_g and $\mathcal{R}$ denote the molecular weight of the gas mixture and the universal gas constant.

The extent of reaction of the decomposing material is determined as the ratio of the difference between virgin and solid densities and the difference between virgin and char densities

$$\beta(t) = \frac{\rho_v - \rho_s(t)}{\rho_v - \rho_c} \tag{2.36}$$

where (t) is used to clarify that solid density is a function of time, whereas the virgin and char densities are independent of time. The extent of reaction is used to compute the virgin and char mass fractions

$$Y_v(t) = \left(\frac{\rho_v}{\rho_s(t)} \right) (1 - \beta) \tag{2.37}$$

$$Y_c(t) = \left(\frac{\rho_c}{\rho_s(t)}\right)\beta(t) \tag{2.38}$$

The virgin and char mass fractions are used to compute the internal energy and enthalpy of the solid material as

$$e_s(p, T) = h_s(p, T) = Y_v e_v(p, T) + (1 - Y_v)e_c(p, T) \tag{2.39}$$

The total energy and enthalpy is

$$e(T) = Y_g e_g(T) + (1 - Y_g)e_s(T) \tag{2.40}$$

$$h(T) = Y_g h_g(T) + (1 - Y_g)h_s(T) \tag{2.41}$$

where $Y_g = \frac{\phi \rho_g}{\rho}$. e_g and h_g represent the energy and enthalpy of the pyrolysis gas.

2.2.3 Thermal Boundary Conditions

Icarus supports various BCs such as isothermal, adiabatic, radiative heat flux, and aeroheating. In this work, only the adiabatic and radiative heat flux BCs are used. For all BCs, two assumptions are made in the implementation: (1) the total heat flux incident on the surface and conducted into the material equals the Fourier conductive heat flux and (2) the effective thermal conductivity for orthotropic materials can be approximated.

For the Neumann BCs, further simplifications are made in Icarus. In particular, for computing ghost cell temperatures, the following approximation is used

$$\kappa_{\text{avg}}\left(\frac{T_{\text{interior}} - T_{\text{ghost}}}{\Delta d}\right) = q \tag{2.42}$$

$$\implies T_{\text{ghost}} = T_{\text{interior}} - \frac{q\Delta d}{\kappa_{\text{avg}}} \tag{2.43}$$

where q is the specified heat flux. Here, κ_{avg} is set to be the through the plane

31

component of thermal conductivity and Δd is the distance between the interior and ghost cell centroids.

For the adiabatic BC, where $q = 0$, the above implementation results in

$$T_{\text{ghost}} = T_{\text{interior}} \tag{2.44}$$

2.2.4 Numerics

Like the linear elasticity solver, the thermal response governing equations are also discretized using FVM. Spatial gradients are computed using the Gauss-Green theorem and temporal discretization is performed explicitly or implicitly using forward or backward Euler, respectively. A more detailed presentation of the numerics can be found in [25].

Both boundary conditions are prescribed directly on the boundary faces, and a layer of ghost cells are used to compute the ghost cell temperatures. Detailed information on the numerics for the BCs can be found in [25].

2.2.5 Thermoelastic Coupling

The thermoelastic coupling is performed in a quasi-steady manner, in which the cell-centered temperature computations are transferred to the structural solver after the thermal material response equations are solved. In [33], it was shown that when the non-dimensional parameter, Boley's number,

$$B = \frac{\tau_T}{\tau_M} = \frac{h^2}{L^2 \kappa} \sqrt{\frac{EI}{\rho_s A}} \tag{2.45}$$

is much greater than unity, then a quasi-steady coupled technique for thermally induced structural deformation is reasonable for the treatment of beams. Here h, L, and I are the geometrical quantities of the beam: thickness, length, area moment of inertia, respectively. The variables E, κ, ρ_s are the material properties of the beam:

modulus of elasticity, thermal conductivity, and solid density. It is therefore purely a function of the material properties and the cross-section dimensions and independent of the rate of heating and the structural boundary supports.

Boley's number represents the ratio of the characteristic thermal and mechanical times, τ_t and τ_M, respectively [33]. For the TPS experiments modeled, Boley's number evaluates to be $\sim \mathcal{O}\left(10^3\right)$, validating the use of a quasi-stready assumption.

The transfer of the temperature allows for the computation of thermal stresses and the resulting deformation due to thermal loading. Thermal stresses are caused by temperature changes in the material and geometric restraints that prevent stress-free thermal expansion. Hooke's law generalized for thermoelastic problems is known as the Duhamel-Neumann relations [34]. The relation for an anisotropic body, described as

$$\boldsymbol{\sigma} = \boldsymbol{C} : [\boldsymbol{\epsilon} - \boldsymbol{\alpha}_{CTE}(T - T_{ref})] \tag{2.46}$$

is implemented, where $\boldsymbol{\alpha}_{CTE}$ is a diagonal matrix consisting of coefficients of thermal expansion in the three orthotropic directions.

Numerically, the addition of thermal stresses only affects the source term, $\boldsymbol{F}$, in Eq. 2.2, and the vector $\boldsymbol{b}$ in the linear system. Therefore, accounting for thermal effects adds little complexity and does not affect the conditioning of the linear system.

CHAPTER III

Code Verification

In this chapter, verification studies for the linear elasticity and Icarus solvers are performed to ensure that the governing equations are solved correctly. Both solvers are relatively new in the TPS community and were in active development during the current research.

As most of the code development aspect of the current work focused on the structural response modeling aspect, most of this chapter focuses on verification and convergence studies of the linear elasticity solver. Specifically, a Method of Manufactured Solutions (MMS) approach is used to empirically observe the spatial order of accuracy of the linear elasticity solver, and the classical cantilever beam deflection problem is modeled to demonstrate the effects of shear locking, a phenomenon relevant for modeling TPS experiments in later chapters. The chapter concludes with a code-to-code comparison of Icarus and the more established 1-D material response solver, FIAT [20], on a 1-D HEEET model subject to conditions representative of the experiments modeled in the later chapters.

3.1 Linear Elasticity Solver Verification

3.1.1 Convergence analysis

Verification studies are performed for the linear elasticity solver. Due to the insufficient complexity of classical problems (e.g., compression and tensile tests) with analytical solutions, the MMS is used to generate more involved analytical solutions [35]. Initially, several solutions are manufactured that isolated portions of the code for individual component testing. Once the individual components (e.g., isolated Dirichlet BC testing) are verified, comprehensive verification is performed.

Only the comprehensive verification study performed using MMS is presented. The manufactured solution from the comprehensive study incorporates all major elements of the solver, allowing for a more thorough verification of the capabilities of the entire code for solving the governing PDEs.

The manufactured solution is chosen to adhere to the guidelines outlined in [35]:

- Smooth analytic solutions, e.g., polynomials, trigonometric functions

- General enough to exercise every term in the governing equations

- Sufficient number of non-trivial solution derivatives

- Derivatives are bounded by a small constant

- Should not prevent code from running successfully to completion during testing

- Defined on a connected subset of two- or three-dimensional space

The following smooth, infinitely differentiable (with non-trivial derivatives), trigonometric solution is used:

$$\boldsymbol{u} = \begin{bmatrix} \cos(x+y+z) \\ \sin(x+y+z) \\ \cos(x+y+z) + \sin(x+y+z) \end{bmatrix} \tag{3.1}$$

which is substituted into Eq. (2.2), resulting in the following source term

$$\boldsymbol{F} = - \begin{bmatrix} \boldsymbol{C}'(1,:)\frac{\partial\boldsymbol{\epsilon}'}{\partial x} + \boldsymbol{C}'(6,:)\frac{\partial\boldsymbol{\epsilon}'}{\partial y} + \boldsymbol{C}'(5,:)\frac{\partial\boldsymbol{\epsilon}'}{\partial z} \\ \boldsymbol{C}'(6,:)\frac{\partial\boldsymbol{\epsilon}'}{\partial x} + \boldsymbol{C}'(2,:)\frac{\partial\boldsymbol{\epsilon}'}{\partial y} + \boldsymbol{C}'(4,:)\frac{\partial\boldsymbol{\epsilon}'}{\partial z} \\ \boldsymbol{C}'(5,:)\frac{\partial\boldsymbol{\epsilon}'}{\partial x} + \boldsymbol{C}'(4,:)\frac{\partial\boldsymbol{\epsilon}'}{\partial y} + \boldsymbol{C}'(3,:)\frac{\partial\boldsymbol{\epsilon}'}{\partial z} \end{bmatrix} \tag{3.2}$$

where

$$\frac{\partial\boldsymbol{\epsilon}'}{\partial x} = \frac{\partial\boldsymbol{\epsilon}'}{\partial y} = \frac{\partial\boldsymbol{\epsilon}'}{\partial z} = \begin{bmatrix} -\cos(x+y+z) \\ -\sin(x+y+z) \\ -\sin(x+y+z) - \cos(x+y+z) \\ -2\sin(x+y+z) - \cos(x+y+z) \\ -2\cos(x+y+z) - \sin(x+y+z) \\ -\cos(x+y+z) - \sin(x+y+z) \end{bmatrix} \tag{3.3}$$

The convergence analysis is performed on Cartesian grids of hexahedral elements for a rectangular block. The spatial discretization for the convergence analysis consists of cells with varying step sizes in the three Cartesian directions. Both Neumann (traction) and Dirichlet BCs are prescribed.

The algebraic tolerances on the residuals for the Generalized Minimal Residual Method (GMRES) iterative method for solving the resulting linear system in Chapter 2 are tightly set during the convergence analysis. This is done to keep the algebraic error smaller than the discretization error as the mesh is refined in order to ensure an accurate convergence analysis. The error is computed using the ℓ_2 norm scaled by volume so that it better approximates the continuous L_2 norm:

$$\|\tilde{\boldsymbol{u}} - \hat{\boldsymbol{u}}\|_{L_2} \approx \sqrt{\sum_{i=1}^{N} V_i \left(\tilde{u}_i - \hat{u}_i\right)^2} \tag{3.4}$$

where $\tilde{\boldsymbol{u}}$ and $\hat{\boldsymbol{u}}$ are the manufactured and numerical solutions, respectively, and the summation is over the N elements within the overall mesh.

Systematic grid refinement by halving the step sizes in each direction is used to produce trends to determine the spatial order of accuracy of the solutions. Four refinements (five meshes) in the spatial discretization of all three cartesian directions are used. Figure 3.1 presents the plot of the approximate L_2 norm vs. the number of cells, where an approximate second order global spatial accuracy is observed for the convergence analysis on a cartesian grid.
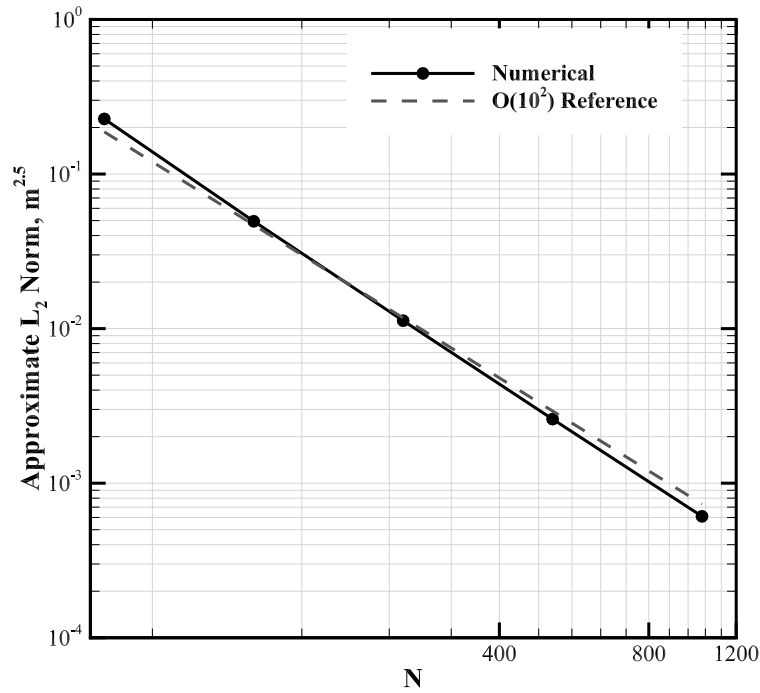
Figure 3.1: Convergence Analysis.

3.1.2 Sensitivity of Numerical Solution to Mesh Refinement for Applied Bending

The ability to accurately model bending phenomena is critical for modeling TPS experiments. For modeling bending, shear locking [36] may arise due to inappropriate spatial discretization and mesh choice, leading to a structure that stiffens or locks and, consequently, net displacements that are significantly under-approximated. This is a common problem encountered in the FVM and Q4 finite element methods for beams undergoing pure bending. The locking effect is magnified when the aspect ratio (AR), the ratio of cell length to its height, of the cells is decreased.

A remedy to shear locking is mesh refinement in the direction of bending, resulting in a larger elemental AR. The classical cantilever deflection problem, shown in Fig. 3.2, is modeled for a 10 m long rectangular steel rod to illustrate the sensitivity of the solution to mesh refinement in the lateral direction (direction of applied loading). The left end is a fixed Dirichlet BC. The four side surfaces are prescribed as a free surface (zero traction) Neumann BC, and the loaded surface experiences a non-zero traction Neumann BC. Table 3.1 shows the inputs and lateral deflections at the loaded end computed by the solver for the six cases of increasing mesh refinement in the lateral direction. The analytical solution for the deflection is derived in [37] as

$$v = -\frac{F}{6EI} \left(3\nu y^2 (L - x) + (3L - x)x^2 \right) \tag{3.5}$$

where I, E, F are the second moment of area, modulus of elasticity, and applied force. The remaining variables, ν, L, x represent the Poisson's ratio, length of the beam, and distance from the fixed end of the beam. At the loaded end, Eq. (3.5) gives $v = -0.02$ m.

Figure 3.3 presents the numerical solutions for the six test cases of varying elemental AR. The shear locking effect is clearly evident for small elemental aspect ratios.

As the spatial step size of the mesh is halved in the direction of bending (y-direction) and held constant in the x- ($\Delta x = 0.1\ m$) and z-directions ($\Delta z = 0.5\ m$), the error in the tip displacement decreases. As the AR is increased, the structure is less susceptible to stiffening and locking, leading to significantly improved numerical solutions. This is better illustrated in Fig. 3.4, where the error in the displacement at the tip asymptotically approaches zero as the AR increases.

A key implication of this study is that in coupled thermo-structural modeling under bending conditions, the mesh should be chosen to ensure convergence in the thermal solutions, as well as chosen to mitigate shear locking effects.

Figure 3.2: Cantilever Schematic.

Table 3.1: Inputs and Outputs for Cantilever Cases

Case No.	E, Pa	Δy, m	Elemental AR $\left(\frac{\Delta x}{\Delta y}\right)$	Free End Deflection, m
1	2×10^{11}	0.5	0.2	-0.0127834
2	2×10^{11}	0.25	0.4	-0.0175923
3	2×10^{11}	0.125	0.8	-0.0193077
4	2×10^{11}	0.0625	1.6	-0.0197732
5	2×10^{11}	0.03125	3.2	-0.0198902
6	2×10^{11}	0.015625	6.4	-0.0199193
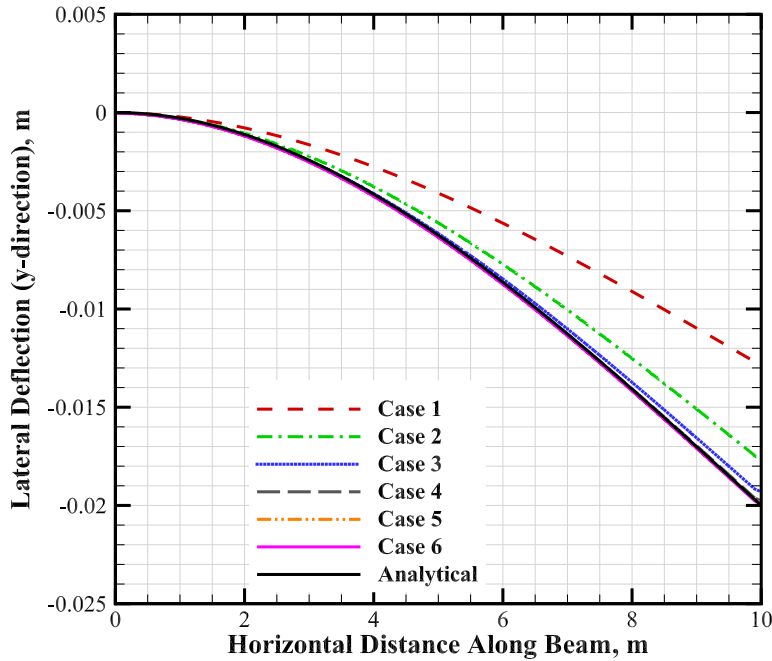
Figure 3.3: Convergence Study of Lateral Mesh Refinement for the Classical Cantilever Problem.

3.2 Icarus Verification

3.2.1 Code-to-code Comparisons

The well-established material response code, FIAT, is used for code-to-code comparisons with Icarus. As FIAT is a 1-D material response code, the verification study here is limited to 1-D. Furthermore, the pyrolysis gas transport model in FIAT does not allow for a permeability input and instead assumes a fully permeable material. To eliminate the differences in physical modeling between Icarus and FIAT, pyrolysis gas transport is ignored.

The geometry modeled is an approximately 0.05 m long rod with a square cross-sectional area of 0.00017 m^2, shown in Fig. 3.5. The four side walls are set to an adiabatic BC, while the top and bottom surfaces use a radiative BC. The radiative heat flux is applied at the top surface for approximately 255 s, and the bottom surface
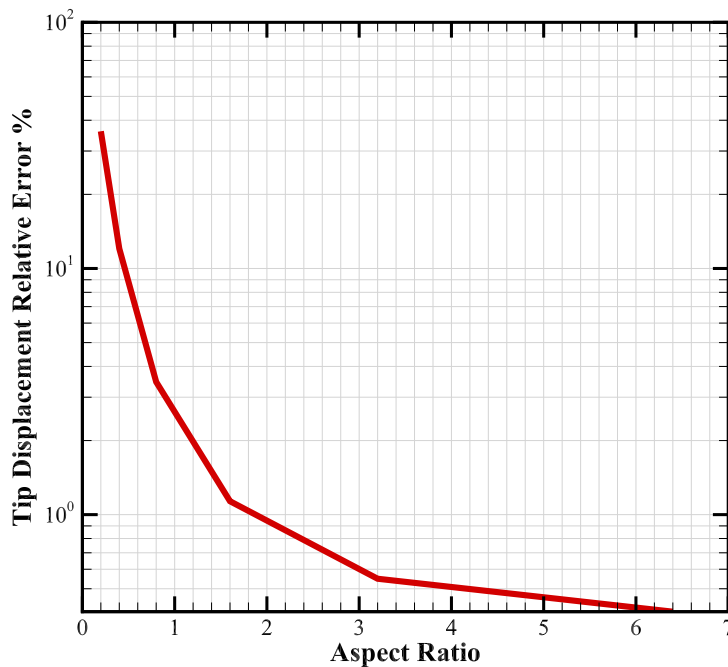
Figure 3.4: Aspect Ratio vs. Tip Displacement Error Convergence.

is allowed to reradiate freely. The material modeled here is a dual-layer HEEET with a composite substrate fixed to the insulation layer, which, along with the boundary conditions, are representative of the HEEET stack-up in the LHMEL experiments modeled in the later chapters.

Figure 3.6 presents the comparison between FIAT and Icarus. The temperatures are normalized by the maximum temperature observed by the predictions from the two solvers. The simulations are performed under representative HEEET LHMEL conditions, where the material is heated for the first 255 s. The temperature results are provided in the TTT direction at multiple depths for five minutes. As this is a 1-D model, In Plane (IP) conduction is neglected.

Excellent agreement is observed between Icarus and FIAT. To quantify the difference between the two predictions, the percentage is plotted in Fig. 3.6b. The difference is generally observed to be under 1%. The minor differences could be
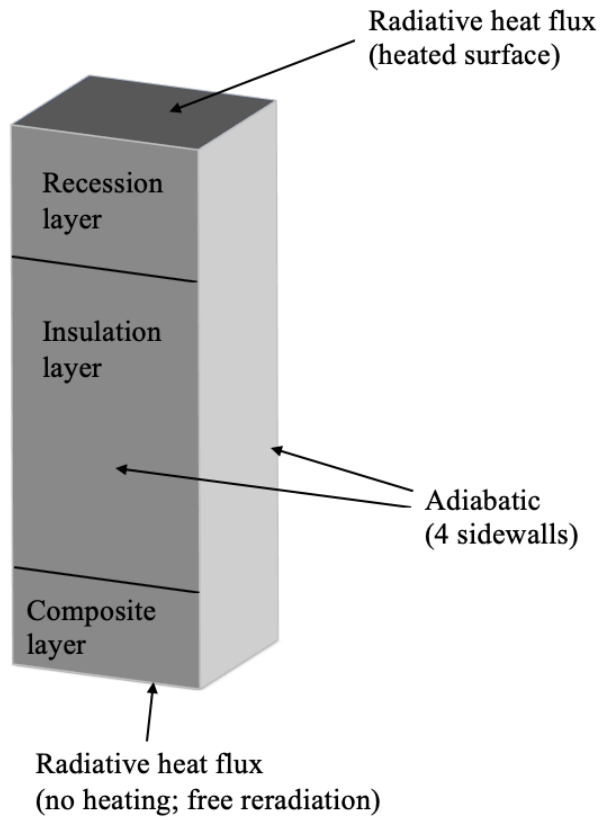
Figure 3.5: 1-D boundary conditions for verification test case.

explained by differences in the numerical discretization, as well as the interpolation/extrapolation method used to obtain the predictions at the thermocouple (TC) locations.

3.3 Chapter summary

Verification studies for the linear elasticity and Icarus solvers were presented in this chapter. The linear elasticity solver was shown to be approximately second order accurate spatially, a sufficient order of accuracy as the majority of modeling tools in the ablation and TPS communities are limited to second order accuracy. The 3-D material response code, Icarus, was shown to be in close agreement with FIAT, a well-established 1-D material response code, on a test case representative of the
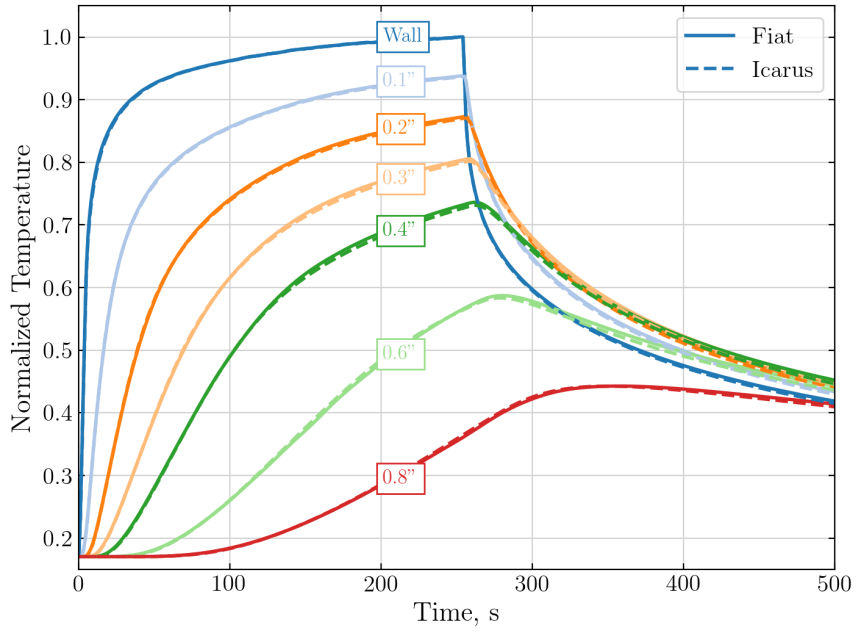
(a) Temperature
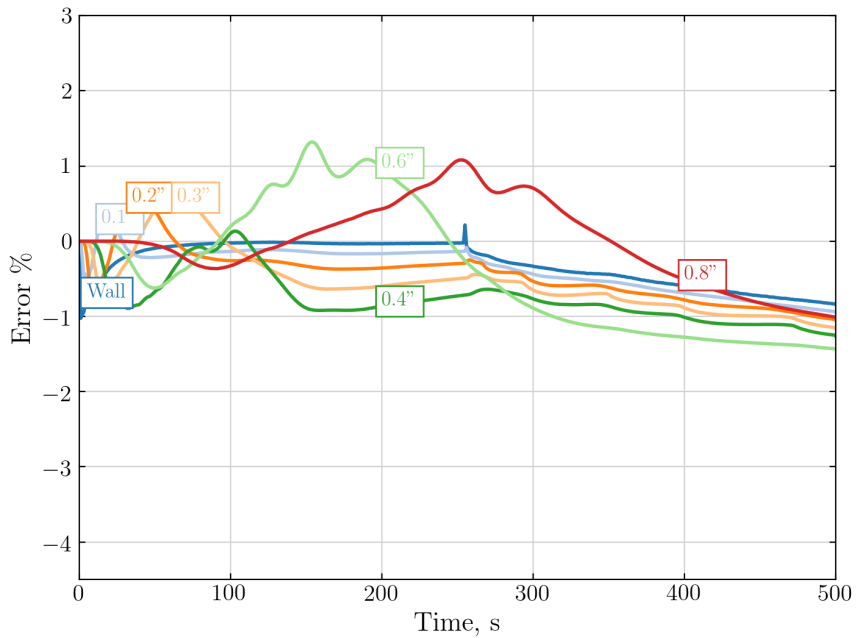
(b) Error

Figure 3.6: Comparison of FIAT vs. Icarus for 1-D verification test case.

conditions modeled in later chapters. These verification studies demonstrate that the thermal and structural response modeling tools that will be used in later chapters are correctly solving the governing equations. Therefore, any inaccuracies in modeling in

the later chapters are expected to be attributed to unmodeled physical phenomena and uncertainties in input parameters and not to the numerics presented here.

CHAPTER IV

Thermal Response Modeling

The analysis in this chapter focuses on using Icarus to model the thermal aspects of the experiments conducted by the HEEET team at the LHMEL at Wright Patterson Air Force Base. Multiple rounds of LHMEL testing were conducted in 2017 and 2018 that focused on thermal, structural, and combined thermo-structural loading of HEEET panels to assess their performance [38]. These experiments provide a rich suite of experimental data for evaluating the thermal, structural, and coupled thermo-structural modeling.

4.1 LHMEL experimental setup

The experimental setup, located inside a vacuum chamber (7 feet in diameter and 9 feet in length), is shown in Fig. 5.1. The chamber is capable of operating at pressures as low as 1 torr and can be actively purged with dry nitrogen gas. Either a 10 kW and 20 kW fiber laser or a 100 kW CO_2 laser with a Gaussian or flat top profile can be used to supply and simulate the desired thermal loading through the windows installed on the walls of the chamber.

The focus of the modeling is on the 2018 experiments, which provide a more comprehensive set of measurements for validation purposes. In the 2018 HEEET experiments, only the 20 kW fiber lasers were used. The fiber laser was operated at

full and half power for several tests at a 1.07 μm wavelength using a continuous pulsed flat top profile with an elliptical spot size. The major and minor axes' diameters of the elliptical spot size are 9.2 in. (0.234 m) and 4.6 in. (0.117 m), respectively. Prior to the laser-induced heat flux reaching the HEEET panel, the elliptical spot size is clipped off using a knife edge mask at the sides to ensure that power is only delivered to the 7 in. (0.178 m) by 4 in. (0.102 m) rectangular region centered on the recession layer surface shown in Fig. 5.1. However, the testing allowed for laser spillage over the two insulation blocks to provide more uniform heating at the top and bottom edges of the HEEET panel and to eliminate steep temperature gradients.

In this experiment, an active nitrogen cross flow is applied to the panel face to provide a chemically inert environment and to remove pyrolysis products that could block the irradiance. The experiment is designed to yield little to no surface ablation, simplifying the computational model significantly as surface chemistry can be effectively neglected. The sides of the dual-layer panel are insulated, and the remaining surfaces are free to reradiate. This setup is designed to yield primarily 1-D thermal phenomena within the vicinity of the centerline. Six thermocouples are situated at 0.1 in. (0.00254 m), 0.2 in. (0.00508 m), 0.3 in. (0.00762 m), 0.4 in. (0.01016 m), 0.6 in. (0.01524 m), and 0.8 in. (0.02032 m) in the TTT direction at the centerline of the HEEET sample to measure the in-depth temperature. A pyrometer and infrared camera are used to measure the surface temperature at the centerline.

The test panels are made of a 3-D WTPS composed of a high density recession-resistant layer and an inner lower density insulative layer of blended carbon and phenolic yarn. The layers are mechanically interlocked together through an industrial weaving process and infused with phenolic resin to form the dual layer HEEET material.

The resulting HEEET material is an orthotropic material where the three mutually orthogonal directions are conveniently aligned with the traditional cartesian axes in

the experimental setup. The warp and weft directions, which together span the IP direction, are oriented along the length and width of the panel, respectively. The TTT direction, as the name suggests, is orthogonal to the IP direction (i.e., in and out of the page).
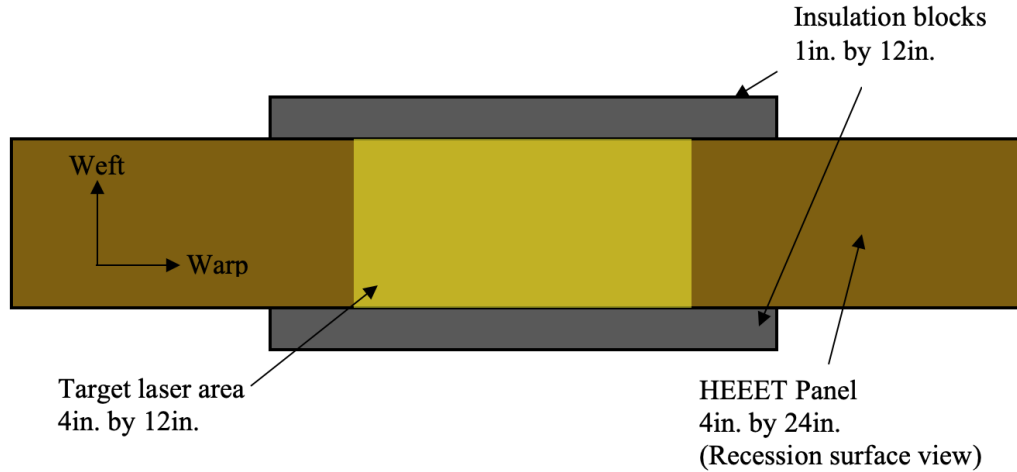
Figure 4.1: Experimental configuration for LHMEL test of HEEET.

Panels were tested at two target power levels using the 20 kW fiber laser: 10 kW and 20 kW. The experimental data provides power measurements at 0.1 s intervals. These readings are used to generate an *a priori* radiative heat flux boundary condition, which will be referred to as "nominal" in the remainder of this chapter. The nominal heat flux schedule computed from the measurements is shown in Fig. 4.2 for the 10 kW and 20 kW target powers. Experimental data indicates that only approximately 75% of the 20 kW target power was realized, therefore a factor of two difference is not observed in Fig. 4.2. The durations of the tests are designed to fully char the recession layer such that the infused resin within the material is fully decomposed into pyrolysis gas products. During irradiation and after the laser is turned off at approximately 255 s, the only mechanism of cooling is expected to be through the un-insulated surfaces, which, as shown in Fig. 5.1, corresponds to all surfaces excluding a centralized portion of the side surfaces.
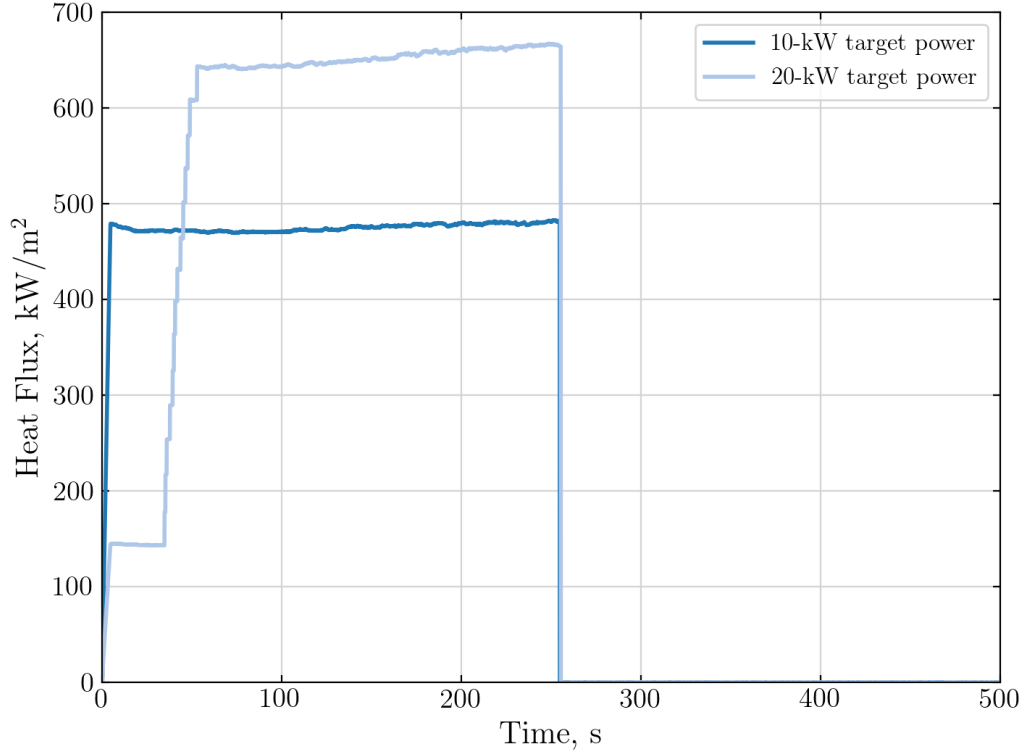
Figure 4.2: Nominal heat flux schedule in the LHMEL tests of HEEET.

For the 10 kW case, the laser is turned on at 0 s and reaches a radiative heat flux of approximately 470 $\frac{kW}{m^2}$ in 5 s. A linear ramping is applied during the first five seconds, and a constant power is maintained for approximately 250 s prior to shutting off the laser. The 20 kW test consists of two separate ramps between zero and five seconds, as well as between 35 and 55 s. As the radiative heat flux boundary condition for the 20 kW case is relatively more complex, the 10 kW case is modeled first.

The boundary conditions are shown in Fig. 4.3. The adiabatic walls correspond to insulation blocks shown in Fig. 5.1. The remaining side walls and the entire bottom surface are free to reradiate.

The mesh for the HEEET panel is shown in Fig. 4.4, where the x, y, z cartesian axes are aligned with the TTT, warp, and weft directions, respectively. Due to the symmetry in the experimental setup, only a quarter geometry is needed. The mesh

is chosen to ensure that the solutions at all TC locations have converged to minimize the errors due to the spatial discretization. As shown, the majority of the elements are concentrated in the recession layer, which is where most of the physicochemical phenomena occurs. Additional refinement is applied in the TTT direction in the vicinity of the recession surface, the recession-insulation layer interface, and at the laser boundary. Further refinement is applied in the warp direction at the laser boundary. These refinements are necessitated by the disparate material properties and boundary conditions at these locations, which generally require a finer mesh to ensure numerical convergence. The mesh in the weft direction is only one layer deep as minimal gradients are expected in that direction due to the nature of the experimental setup and observations in the experimental measurements of temperature in the weft direction. A subsequent section will demonstrate this.
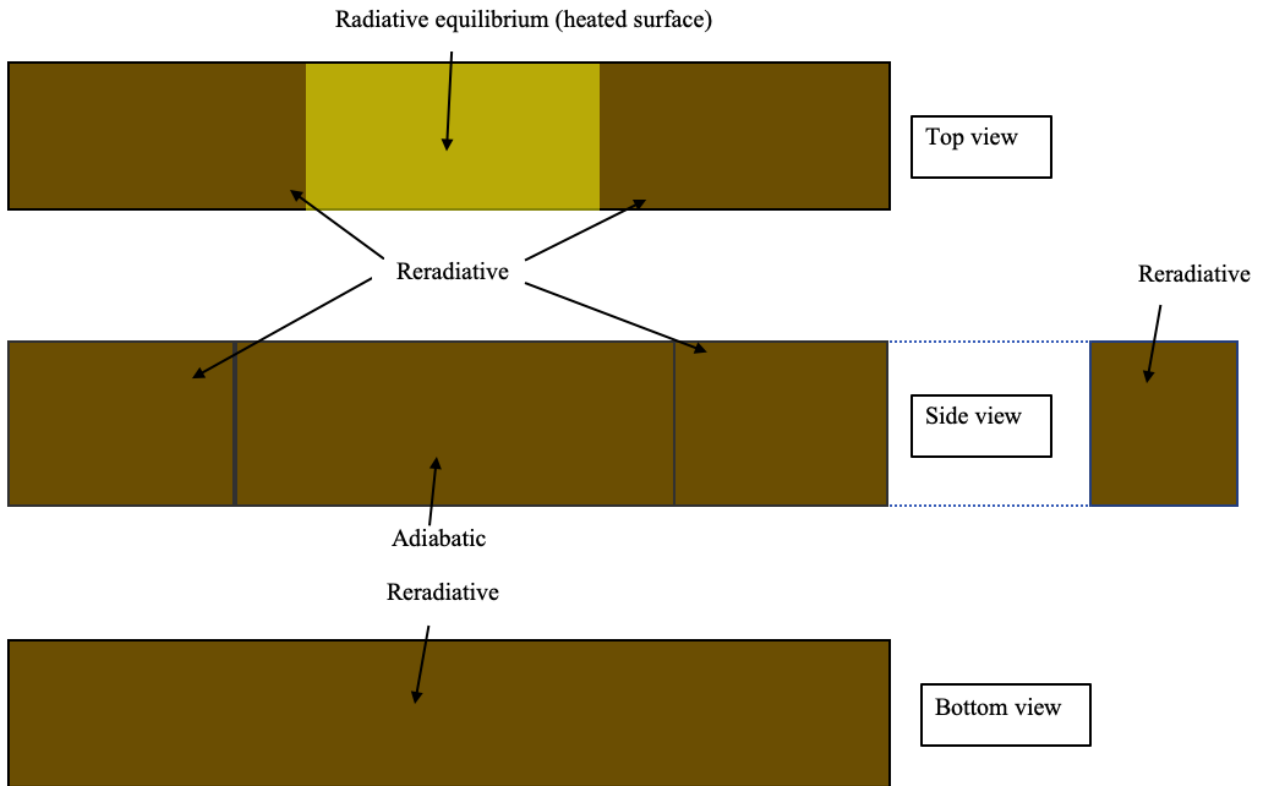
Figure 4.3: Boundary conditions for LHMEL test of HEEET.

The HEEET is a very low porosity and permeability material (e.g., several orders
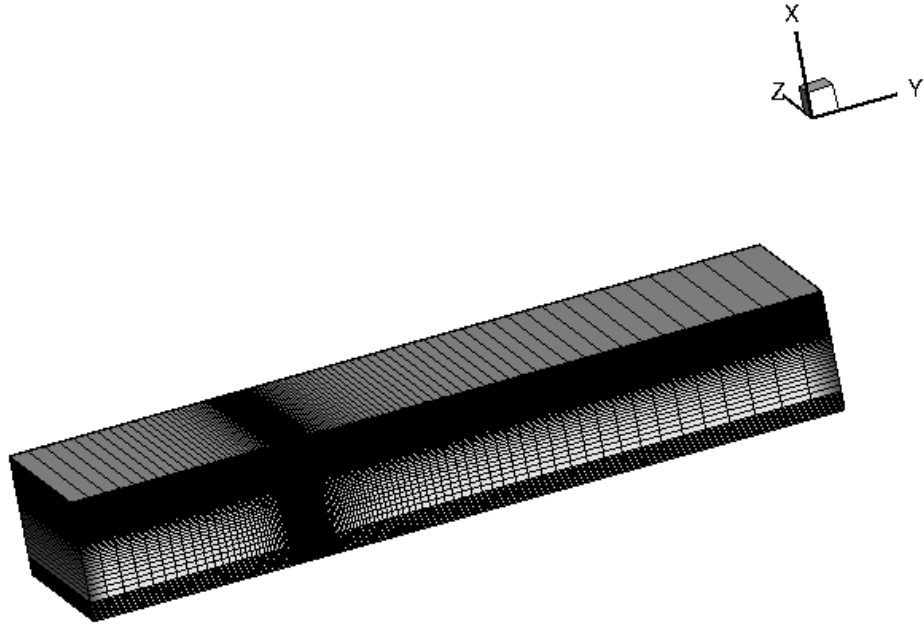
Figure 4.4: Quarter mesh for HEEET model.

of magnitude lower than that of PICA), so the pyrolysis gas cannot as easily flow through the pores of the material, largely diminishing any reduction in temperature due to pyrolysis gas transport that might otherwise be observed in a high permeability material. Due to the low porosity and the uncertainties in the permeability of the recession and insulation layers in the orthotropic directions, the study here neglects the pyrolysis gas transport phenomena. Instead, the focus is directed towards the multi-dimensional in-depth heat transport, as well as the spatial radiative heat flux profile, which are postulated to be the principal factors governing the simulation predictions.

4.2   10 kW Case

4.2.1   Reconstruction of magnitude of radiative heat flux profile

The nominal heat flux schedule is used as the radiative heat flux input into Icarus for an initial assessment of the comparisons between experimental measurements and simulation predictions at the centerline that are presented in Fig. 4.5a. Unless otherwise stated, all temperature plots in this section are normalized by the radiative equilibrium temperature, which is computed using the gray body Stefan-Boltzmann Law shown in Eq. (4.1):

$$q = \epsilon \sigma T_{\text{radeq}}^4 \tag{4.1}$$

where q is the radiative heat flux and ϵ and σ are the emissivity and the Stefan-Boltzmann constant, respectively. As the emissivity of a charring ablator varies with temperature, the computation of the radiative equilibrium temperature, T_{radeq}, is iterative.

From this comparison, it is clear that by using the nominal heat flux schedule, Icarus underpredicts the temperature at the recession surface (labeled as "wall") and the shallow in-depth locations. For the deeper locations, a shift from underprediction to overprediction is observed. As previously mentioned, the nominal heat flux schedule is generated from experimental measurements; however, this does not necessarily indicate that the sample is actually experiencing this measured power at the centerline. In fact, the comparisons for the top-level TCs, where the physics is predominantly governed by the radiative boundary condition, suggest that a higher heat flux is experienced at the centerline. As such, a correction factor is applied to the nominal heat flux schedule to improve the agreement between the simulation predictions generated from the corrected heat flux and the experimental measurements at the centerline. This is similar to the "TC driver" methodology that is routinely used

in the community [39].

According to the experimentalists[1], the TCs provide the most reliable measurements, and observations of experimental data indicate that the surface temperature measured by the pyrometer is above reasonable thresholds (e.g., the pyrometer measurements exceed the radiative equillibrium temperature). The infrared camera was not used for the 10 kW experiment, which was another device installed to measure surface temperature. However, based on comparisons and observations between the pyrometer and infrared measurements for the other panels tested in the LHMEL experiments, it appears that the pyrometer measurements are consistently higher than that of the infrared data, which suggests that the former is overmeasuring, the latter is undermeasuring, or a combination of the two. In Fig. 4.5a, the pyrometer measurements are shown to be greater than unity (i.e., the measured temperature is greater than the computed radiative equilibrium temperature), which further suggests that either the pyrometer is overmeasuring or the computed radiative equilibrium temperature is smaller than reality.

Due to the uncertainties in the surface temperature measurements, the reconstruction process focuses on matching the more confident measurements from the TCs. In particular, only the top-level TCs are used for the heat flux reconstruction, as shallower locations are more susceptible to the boundary condition and not as sensitive to the material model.

After studying several correction factors, it is determined that a 20% increase from the nominal radiative heat flux schedule achieves the best agreement with the TC measurements at the shallow in-depth locations. The bottom-level TC measurements are much more sensitive to the material model, and less so to the boundary condition, and are therefore not used as part of the boundary condition inference process.

The comparison using the inferred radiative heat flux schedule is shown in Fig.

---

[1]E. Stern, private communication, December 2019

4.5b, where excellent agreement is observed between simulation predictions and the top-level TCs' measurements during the heating and cooling phases. The corresponding MSE (note that all tabulated MSE in this chapter are based on the normalized temperatures) for the predictions generated from the nominal and corrected (denoted as 1.20) radiative heat flux schedules is shown in Table 4.1. The headings "Heating" and "Total" correspond to the MSE computed for the heating phase and for the entire duration, respectively. It is clear that the MSE for the predictions at the two top-level TCs decrease by a factor of 3-10, but the MSE for the bottom-level TCs increases. The discrepancy between the simulation predictions and experimental measurements for the bottom-level locations will be studied in a later section.

Table 4.1: MSE for 10 kW centerline comparisons.

	Nominal		1.20	
	Heating	Total	Heating	Total
0.1 in.	1.095e-03	1.262e-03	3.115e-05	1.661e-04
0.2 in.	6.415e-04	1.293e-03	2.314e-04	3.942e-04
0.3 in.	2.929e-04	1.381e-03	5.646e-04	8.519e-04
0.4 in.	3.264e-04	1.693e-03	1.085e-03	1.484e-03
0.6 in.	2.164e-04	7.941e-04	1.151e-03	1.449e-03
0.8 in.	7.416e-05	2.365e-04	2.559e-04	1.475e-03

4.2.1.1 Comparisons of 1-D, 2-D, and 3-D transport at the centerline

After reconstructing the radiative heat flux magnitude at the centerline, the corrected heat flux is used to model multi-dimensional heat transfer in the material. Prior to assessing the modeling at off-center locations, centerline temperature comparisons are performed for 1-D, 2-D, and 3-D models.

The mesh parameters of the n-dimensional models are shown in Table 4.2. For all three cases, the grid refinement is identical in the TTT direction. The 2-D and 3-D cases refine the grid in the IP directions, where the former refines only along the warp direction and the latter along both the warp and weft directions. It is
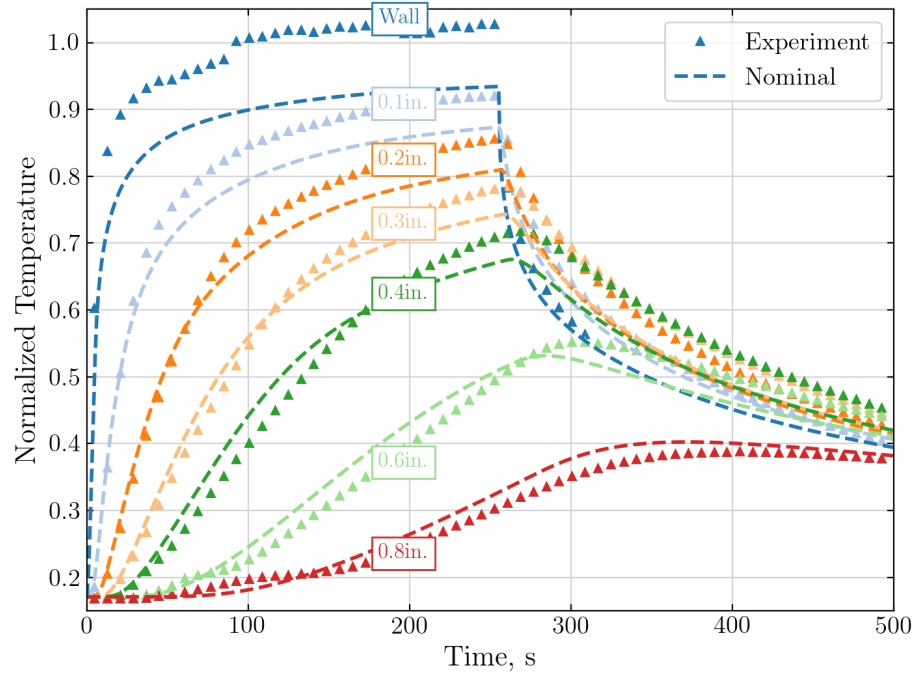
(a) Nominal
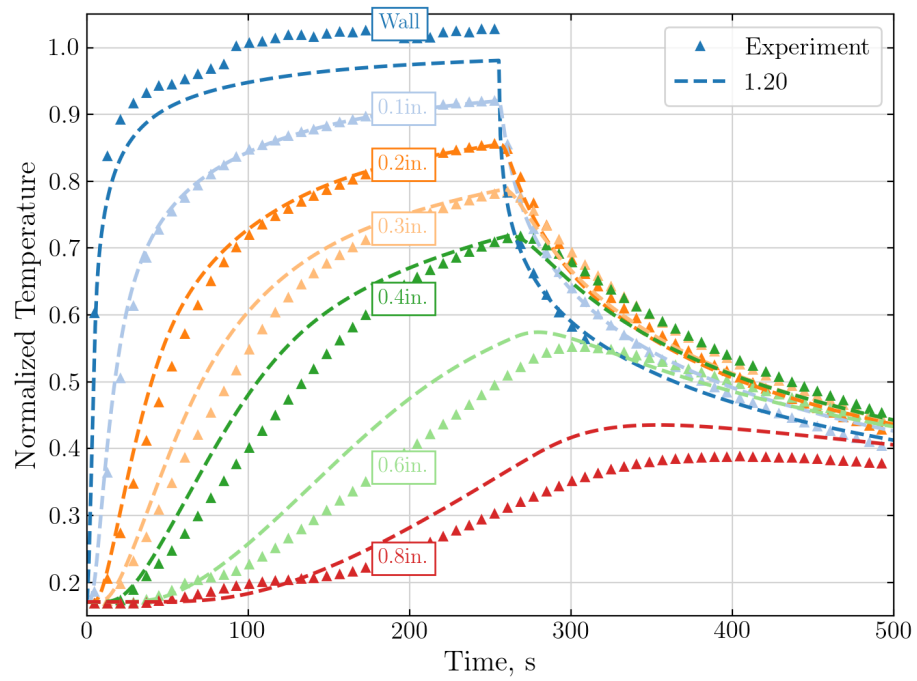
(b) 1.20 scaling

Figure 4.5: Comparison of simulation predictions vs. experimental measurements at the centerline.

hypothesized that the physics at the centerline will be predominantly 1-D due to the nature of the experimental setup, where insulative material is applied to both sides of the HEEET specimen as shown in Fig. 5.1, effectively limiting conduction in the weft direction, and where the laser spans several inches off-center, further reducing the dimensionality of the problem.

Table 4.2: Number of layers in TTT (N_{TTT}), warp (N_{warp}), and weft (N_{weft}) directions.

n	N_{TTT}	N_{warp}	N_{weft}
1-D	98	1	1
2-D	98	126	1
3-D	98	126	16

The results of this study are presented in Fig. 4.6. Figure 4.6a shows the temperature comparisons. Qualitatively, the results for the three cases are very similar, with the 2-D and 3-D cases predicting slightly lower temperatures. The lower temperatures in the multi-dimensional cases are expected due to the added mechanism of cooling through the IP directions; however, it is evident from the plots that this effect is minimal across all depths at the centerline. This observation is more evident for the deeper locations and during the cooling phase (after 255 s), where the cooling effects due to IP conduction are relatively more prominent, whereas temperature predictions closer to the surface are dominated by the radiative BC rather than the in-depth material model.

These observations are supported and illuminated by the absolute error plots shown in Fig. 4.6b. The absolute error percentage uses the 3-D predictions as the expected value in its computation as the 3-D model is the most accurate from a theoretical perspective. In the error curves, it is clear that during the heating phase, surface temperature predictions are governed by 1-D effects as evidenced by the approximately 0% error in the 1-D curve. For the 1-D curves, the error increases further in-depth, as well as during the cooling phase, as previously qualitatively observed,

due to the gradual increase in the importance of the multi-dimensional conductive heat transport. The 2-D curves exhibit approximately 0% error, with the maximum error of 1% observed at the 0.1 in. location at approximately 30 s, indicating that 3-D effects are negligible at the centerline. This is intuitive due to the presence of the insulative blocks, which effectively constrain the centerline to 2-D heat transfer for all depths as alluded to earlier.

4.2.1.2   Off-center comparisons

Figure 4.7 shows a side view of the HEEET panel being modeled. During the LHMEL experiments, TC arrays were situated at four off-center locations along the length of the sample: 1.25 in., 2.5 in., 3.25 in., and 3.75 in. at various depths. Note that the laser profile spans 3.5 in. off-center, so the last location is just outside of the direct laser impact region.

It is hypothesized that the 3.75 in. location may be most susceptible to 3-D effects due to reradiative effects at the sidewalls after the insulation boundary shown in Fig. 4.7. To test this hypothesis, 2-D and 3-D simulations are performed.

Figure 4.8 shows the comparison between 2-D and 3-D predictions for all off-center locations. It is evident that there is virtually no difference between the two cases at all off-center locations and across all-depths. This is not surprising as the insulation block spans 2.25 in. past the last off-center location, largely constraining the off-center locations to 2-D effects. It is surprising that the error for predictions at the 3.75 in. location is smaller than that of the predictions at the 1.25 in. location, as the 3-D effects should increase further away from the centerline and closer to the reradiative sidewall. However, because the errors are so small, the observation is deemed insignificant, but a conclusion can be confidently drawn that predictions conducted on a 2D mesh are adequate, and will therefore be used for the remainder of this chapter.
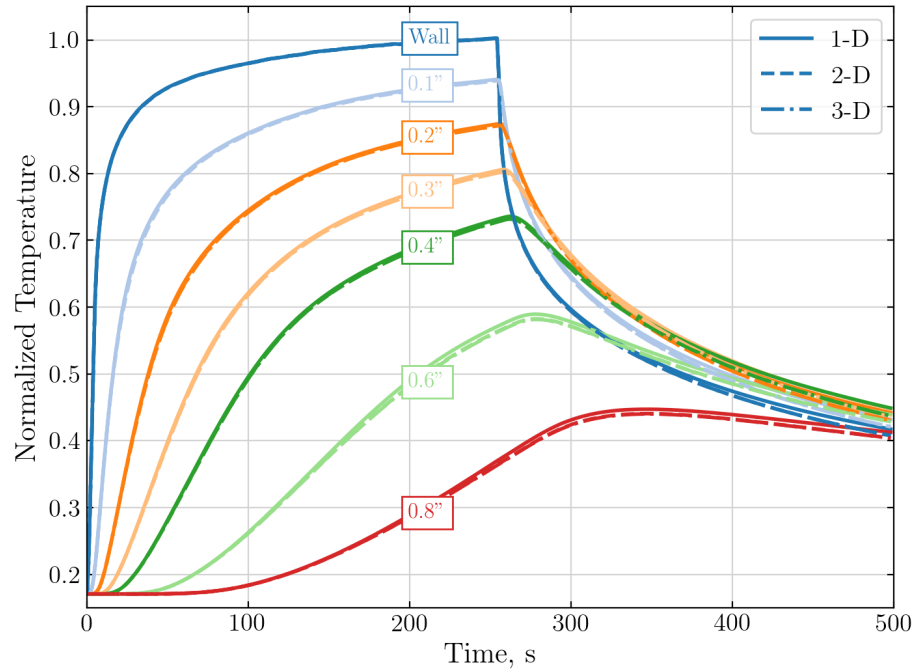
(a) Temperature
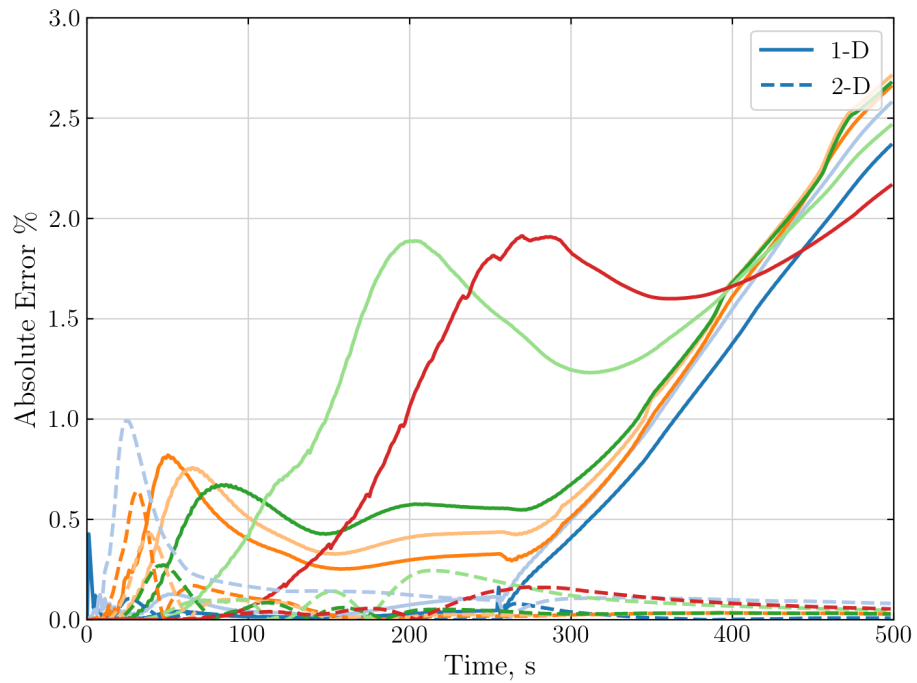
(b) Error

Figure 4.6: Comparison of Icarus predictions at the centerline between 1-D, 2-D, and 3-D cases.
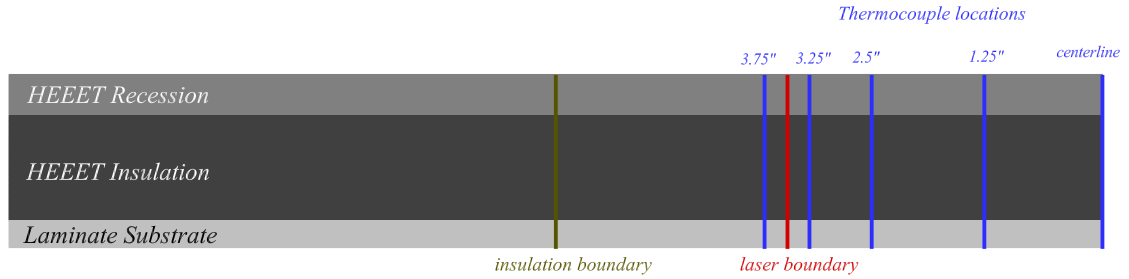
Figure 4.7: Material stackup and off-center thermocouple array locations.

Figure 4.9 presents the comparisons between Icarus predictions and TC measurements at the off-center locations. At all locations, and for both experimental measurements and simulation results, the temperature at the more shallow depths reaches its peak temperature faster than that of the deeper locations in both the experimental measurements and simulation predictions. During the cooldown phase, the temperature further in-depth decreases at a slower rate than that of the shallower depths. These observations are due to a combination of reradiation at the surface, the transient conduction process, and the timescales at which they operate. This lag in which the TCs reach their peak temperature is due to the timescale associated with the conductive propagation of the radiative heat flux effects through the material. Similarly, when the laser is shut off, the deeper TCs take longer to be affected by the reradiative cooling at the surface, resulting in a slower rate of decrease in temperature.

Several other interesting attributes are observed in the comparisons between the measurements and predictions. First, in Figs. 4.9a - 4.9b, both the experimental and simulation results with a 1.20 scaled heat flux profile reach approximately the same peak temperature at several off-center locations and depths. However, Icarus, in general, predicts a larger initial rate of increase, especially for the deeper TCs. This is less pronounced at the shallow TC locations as the effects of the radiative BC
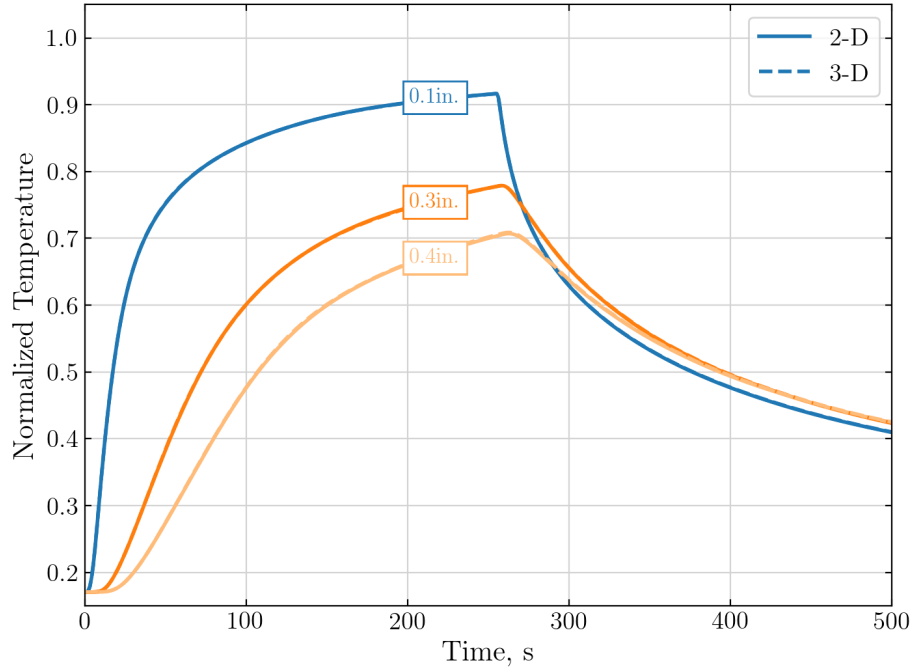
(a) 1.25 in. normalized temperature comparison.
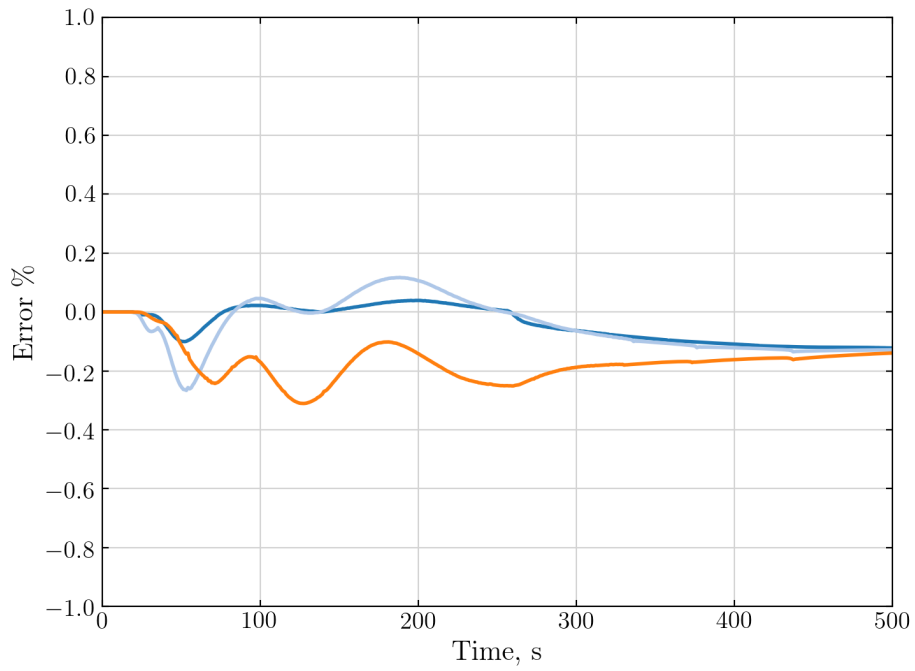
(b) 1.25 in. error %.

is more dominant than that of the material model, so any inaccuracies that may exist in the material model are not as significant. For the deeper TCs, this observation is likely attributed to the material model, where the conductivity inputs for the

59
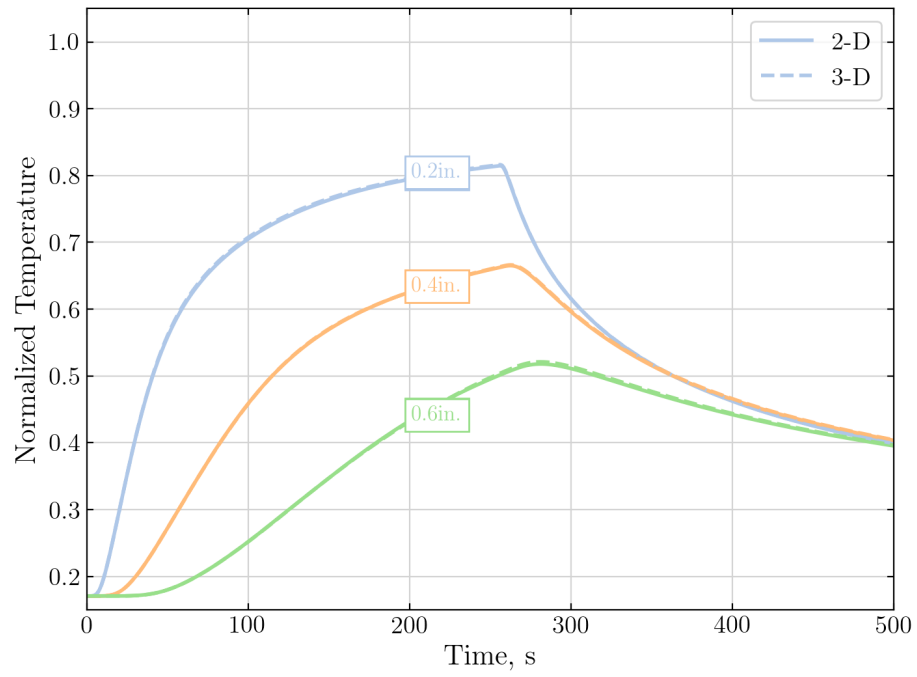
(c) 2.5 in. normalized temperature comparison.

(d) 2.5 in. error %.

60
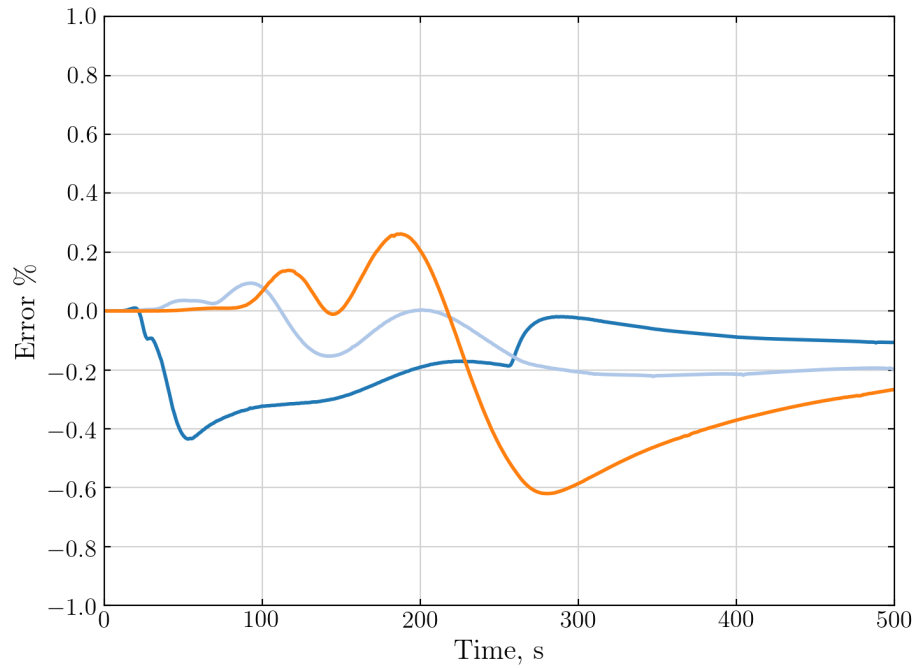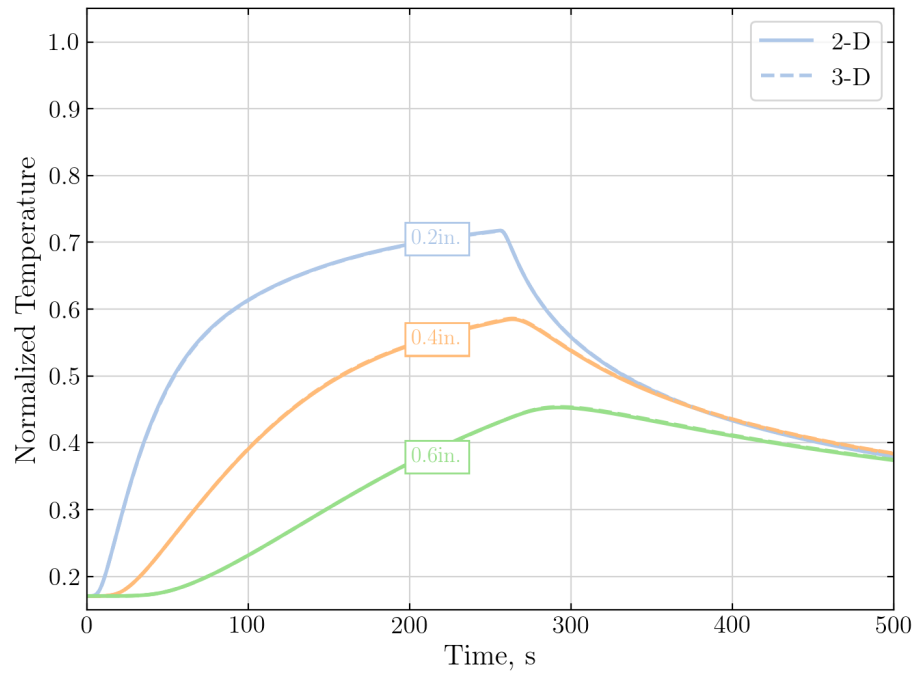
(e) 3.25 in. normalized temperature comparison.

(f) 3.25 in. error %.

61
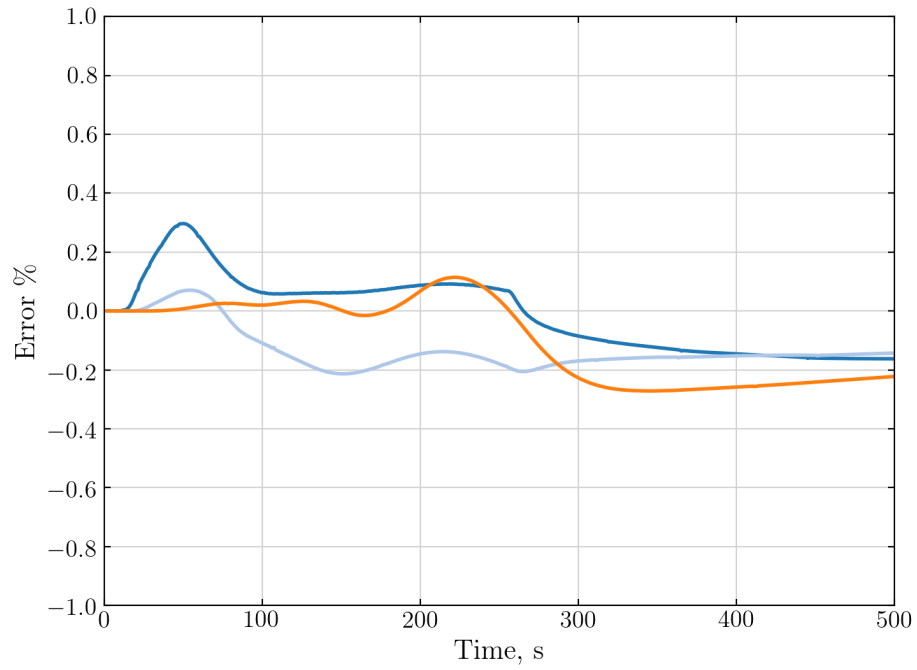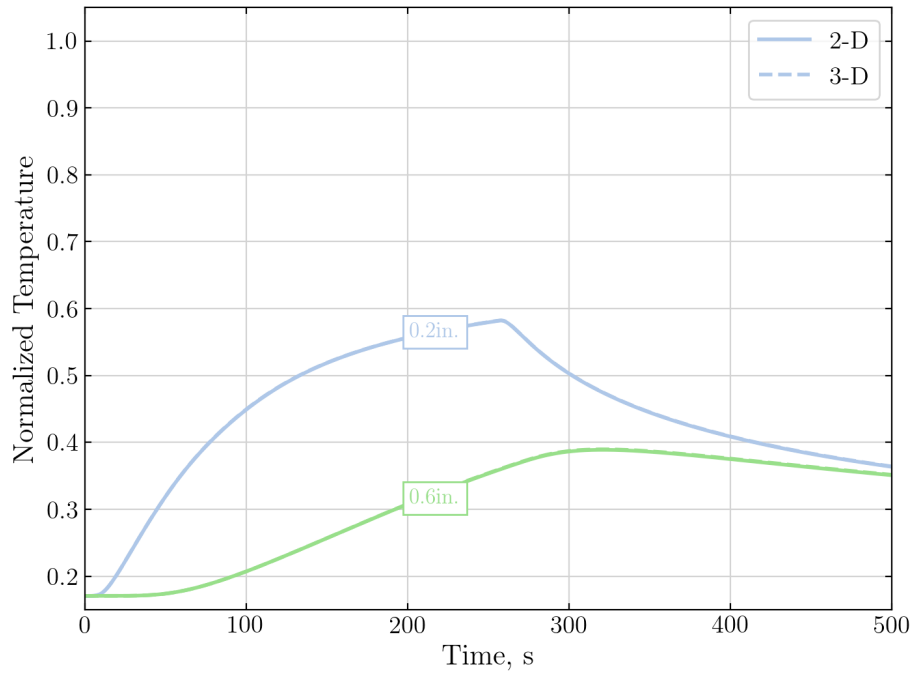
(g) 3.75 in. normalized temperature comparison.
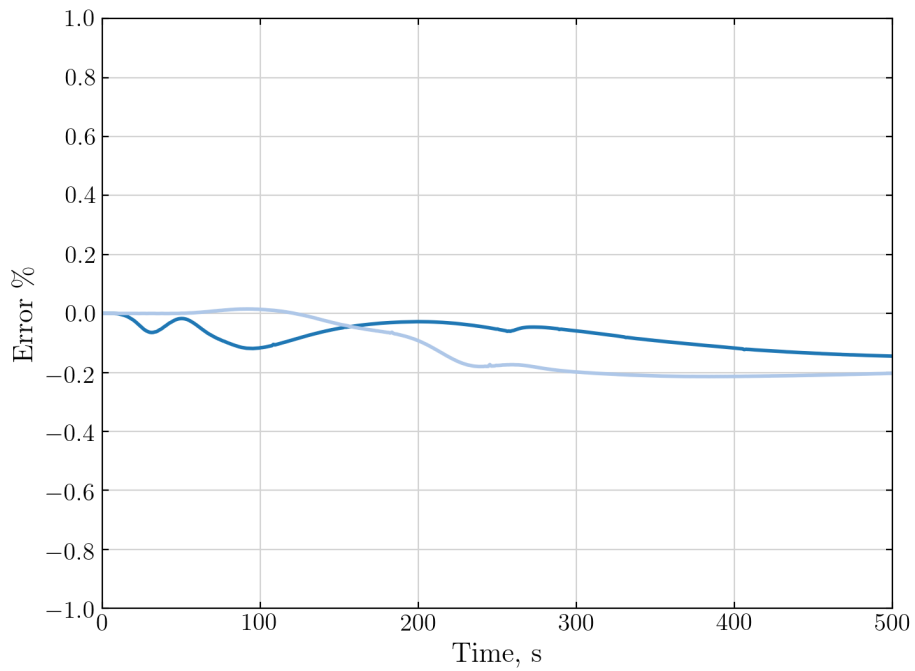
(h) 3.75 in. error %.

Figure 4.8: Comparison of 2-D and 3-D Icarus predictions at off-center locations.
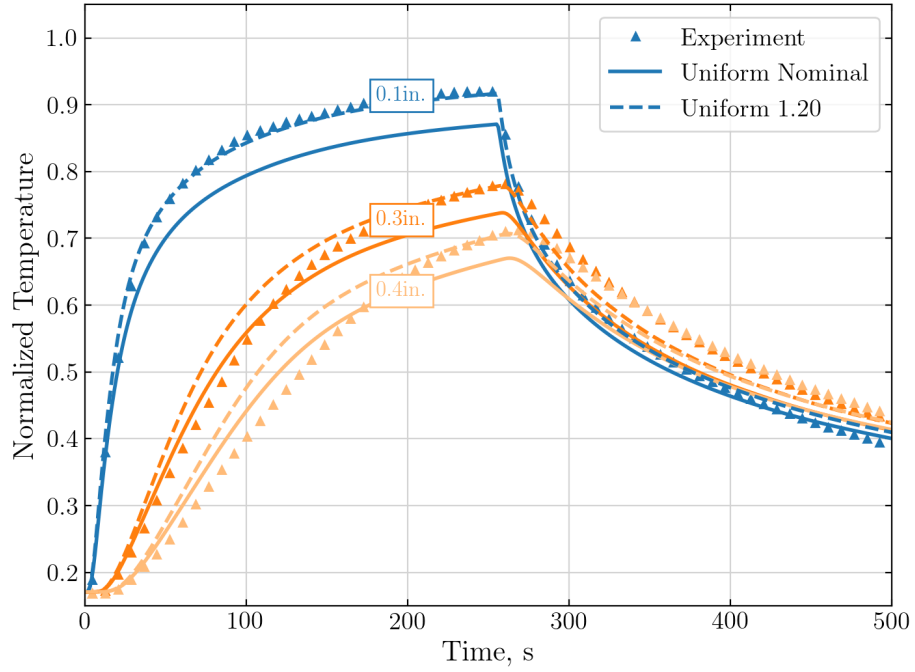
(a) 1.25 in. from centerline.
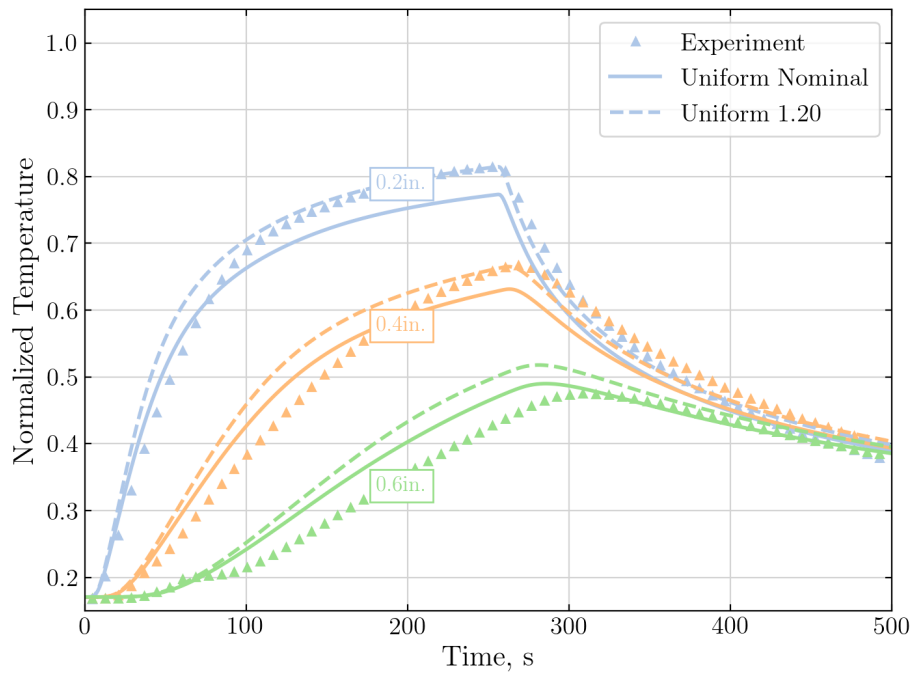
(b) 2.50 in. from centerline.

simulation may be larger than that of the actual material, resulting in a faster increase in temperature. This is supported by the observation that the simulation results from both the corrected and nominal heat flux profiles overestimate the temperature at
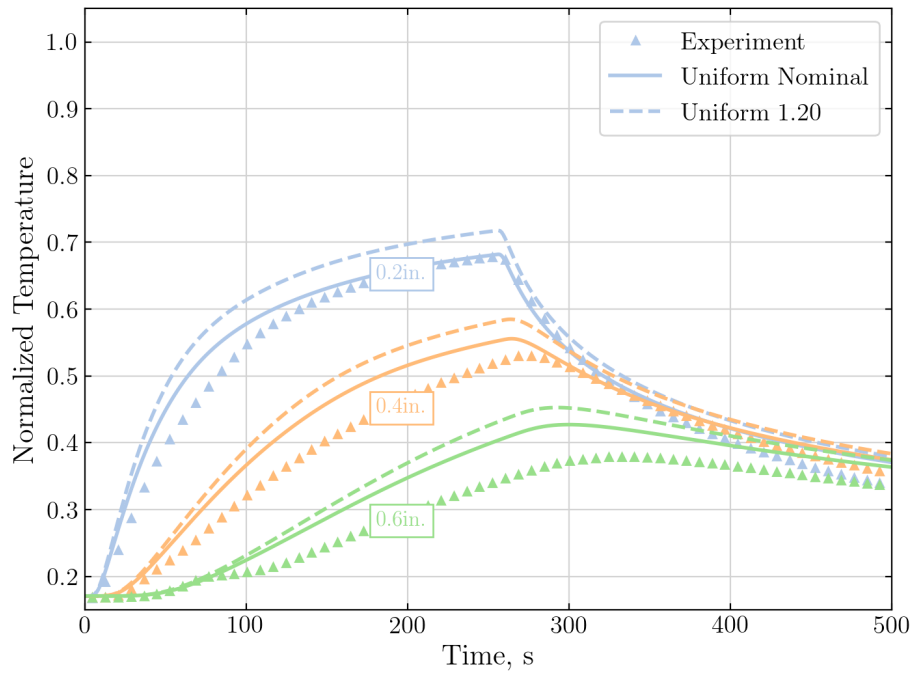
(c) 3.25 in. from centerline.
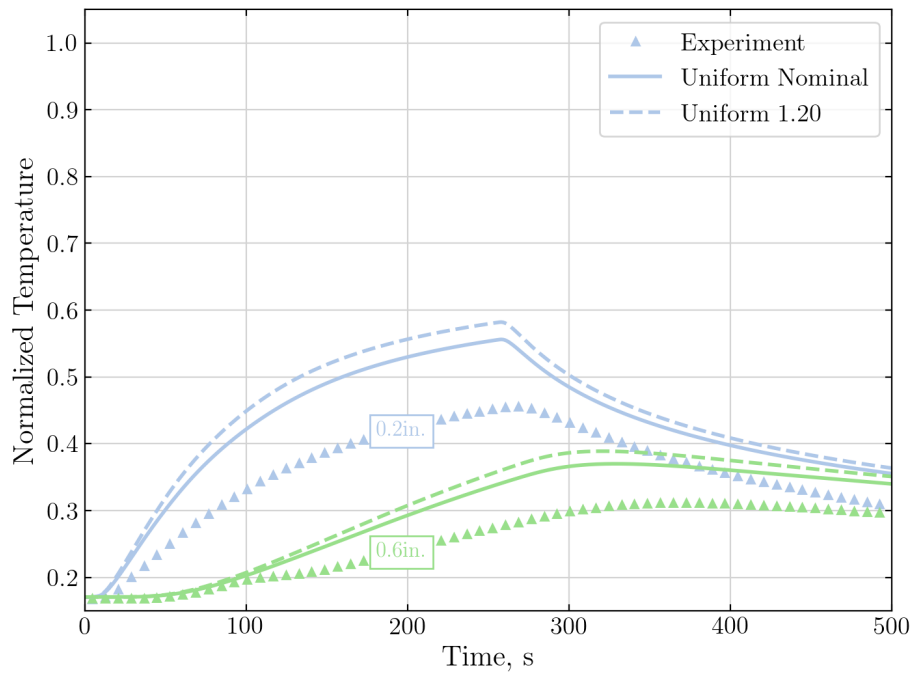
(d) 3.75 in. from centerline.

Figure 4.9: Comparisons of off-center TC predictions (under a flat-top heat flux profile assumption) with experiment.

the bottom TCs and that, in general, the experimental measurements indicate that the peak temperature is reached several seconds later than that of the simulation predictions.

Next, it is evident that the 2-D heat transfer effects are manifested in the decrease in temperature away from the centerline, as heat is conducted out of the direct laser impact region in the IP directions. The 1.25 in. off-center results are near identical to the centerline results; however, at 2.5 in. off-center, which is still well within the direct laser impact region, the 0.4 in. depth curve yields a lower temperature than the measurement at the 1.25 in. location. This is observed in both the experimental measurements and simulation results. This downward trend continues to the edge of the direct laser impact region as shown in Fig. 4.9c and just outside of the region as shown in Fig. 4.9d. It is clear from both the experimental and simulation results that 2-D effects due to IP conduction in the warp direction of the sample are cooling the material.

Finally, it is evident that the agreement between the predictions using the corrected radiative heat flux BC and measurements worsens further away from the centerline. This is likely due to a combination of the spatial heat flux profile and, again, the material model. The former suggests that the actual heat flux profile is not uniform, which is intuitive, as ideal flat top profiles are not realistic. Rather than an infinite slope at the laser boundary, it is hypothesized that the decay in heat flux at the laser boundary is gradual. This hypothesis is supported by the observation that the predictions using the nominal heat flux schedule are in better agreement with the experimental results at the last two off-center locations. Therefore, the hypothesis motivates the study of non-uniform heat flux profiles in the next section. Furthermore, the observations here have indicated that the material model may not accurately reflect the HEEET panel being tested. In a subsequent section, studies will assess different material models.

4.2.1.3 Non-uniform studies

A flat top profile heat flux profile can be approximated with a Supergaussian (SG), which takes the form

$$q(x) = q_{\max} \exp\left[\left(-\frac{x}{\sigma}\right)^n\right] \tag{4.2}$$

where σ is the standard deviation and n indicates the order of the SG, where $n = 1$ reduces to a zero-mean gaussian. The standard deviation governs the spread, where the larger the standard deviation, the more the profile disperses away from the mean. The n parameter governs the rate of decrease, where in the limit as $n \to \infty$, an idealized flat-top profile is realized. The variable x is the distance along the length of the sample from the centerline. The maximum radiative heat flux, $q_{\max}$, realized at the centerline is chosen to be the corrected uniform heat flux as the centerline predictions using the corrected uniform heat flux at the shallow TCs are in close agreement with the experimental results.

The SG parameters that are employed in this work are shown in Table 4.3 and the resulting profiles illustrated in Fig. 4.10. Three SG profiles are tested where the parameters n and σ are determined to ensure that the total power is consistent with the experimental measurements. The predictions using these profiles are shown in Figs. 4.11a - 4.11d along with the results from the corrected and nominal uniform profiles for reference.

The predictions using a SG heat flux profile are generally observed to yield smaller temperatures at all temporal and spatial locations than the predictions from the corrected uniform profile. This is intuitive because the total power experienced by the panel is smaller for the SG profiles than for the corrected uniform profile. The predictions for cases 1-3 achieve much better agreement with experimental results for the TCs at the 3.75 in. location at both depths, as well as for the bottom level TCs at the 2.50 in. and 3.25 in. locations; however, the agreement at the top level TCs at

the 2.50 in. and 3.25 in. locations worsened. This is not surprising after inspecting Fig. 4.10, where the supergaussian profiles are shown to drop to approximately zero flux between the 2.5 in. and 3.25 in. locations, as opposed to the 3.5 in. location in the nominal and corrected flat-top profiles. Clearly, when constrained by a constant power, the choice of a flat-top or SG profile is a balancing act, where better agreement at farther off-center locations is achieved at the expense of worsening agreement at closer locations.

Table 4.3: SG parameters.

Case No.	n	σ
1	4	0.0063
2	8	0.006
3	14	0.0058
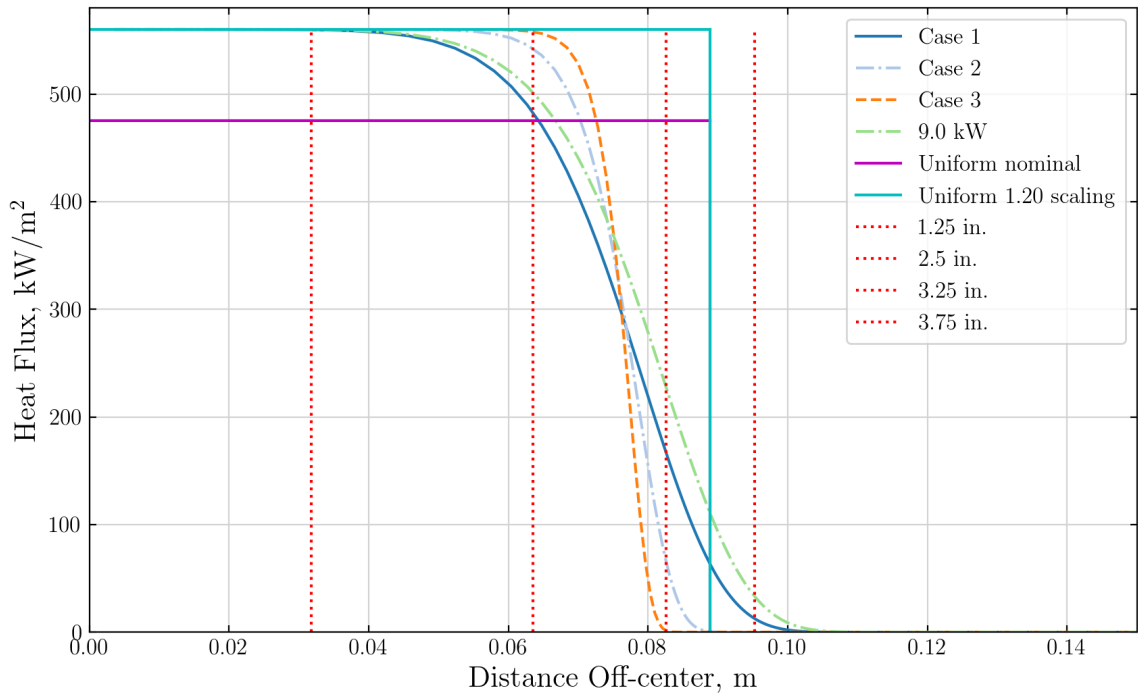
Figure 4.10: SG profiles.

This analysis raises an important question and uncertainty in the modeling: what is the actual power experienced by the rectangular region on the HEEET panel?
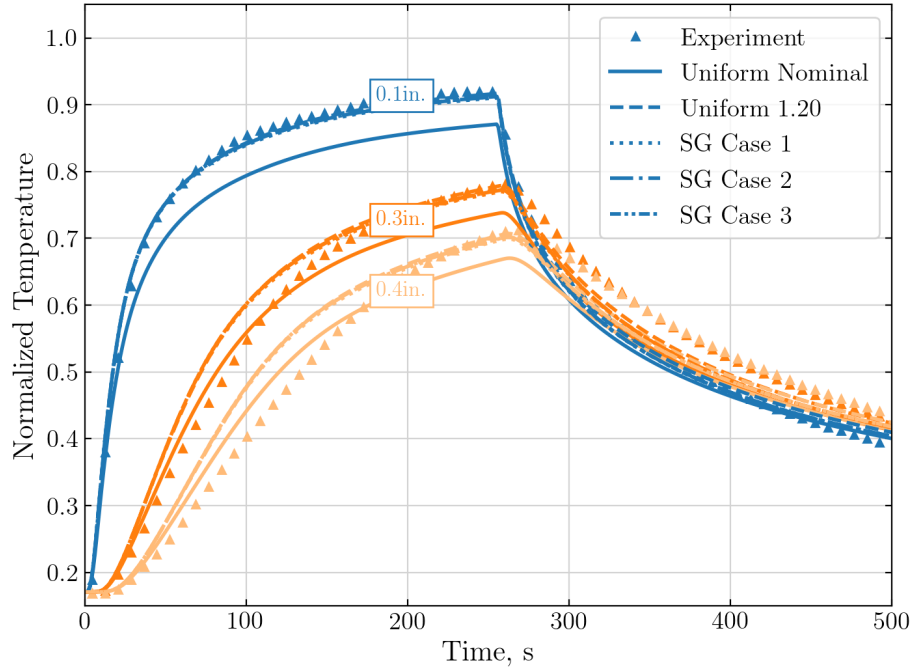
(a) 1.25 in. from centerline.
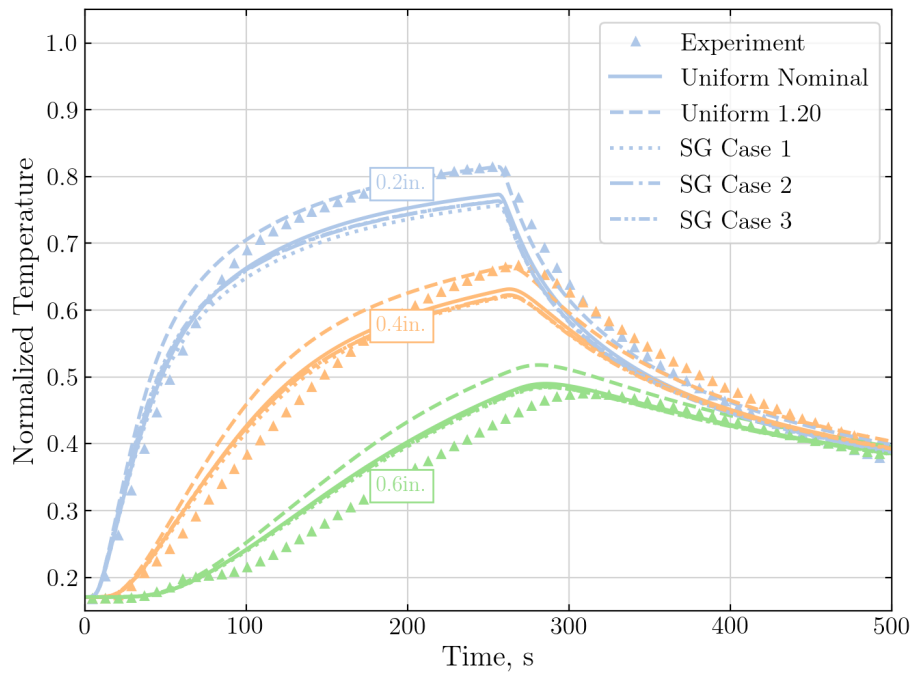
(b) 2.50 in. from centerline.

Surely, this power must be equal to or less than that of the measured power. Prior to reaching the panel, the fiber laser, which exhibits an elliptical spot, is clipped off at the sides in the warp direction, but not in the weft direction; hence, a percentage of
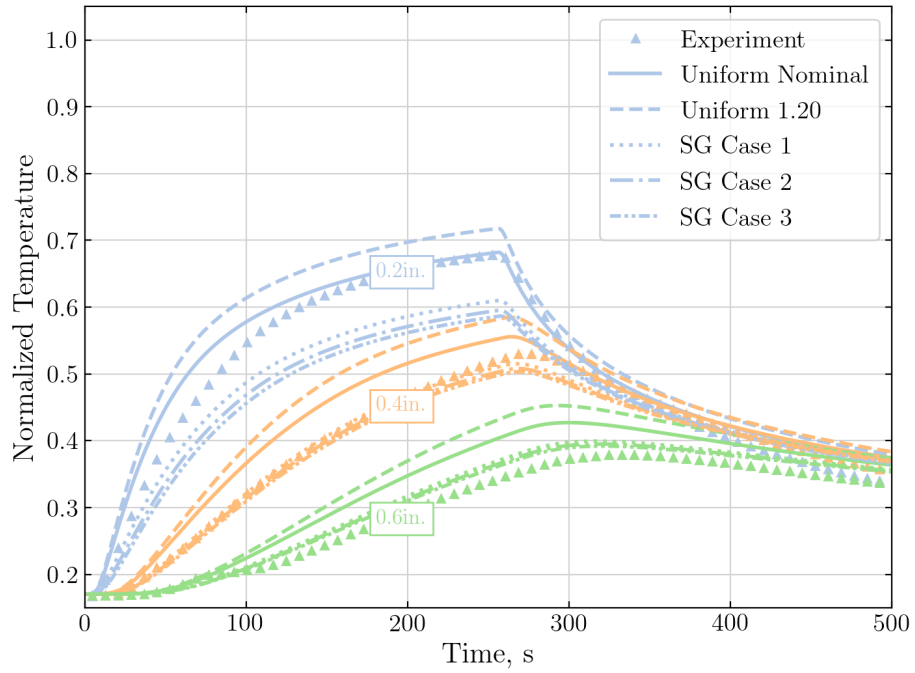
(c) 3.25 in. from centerline.
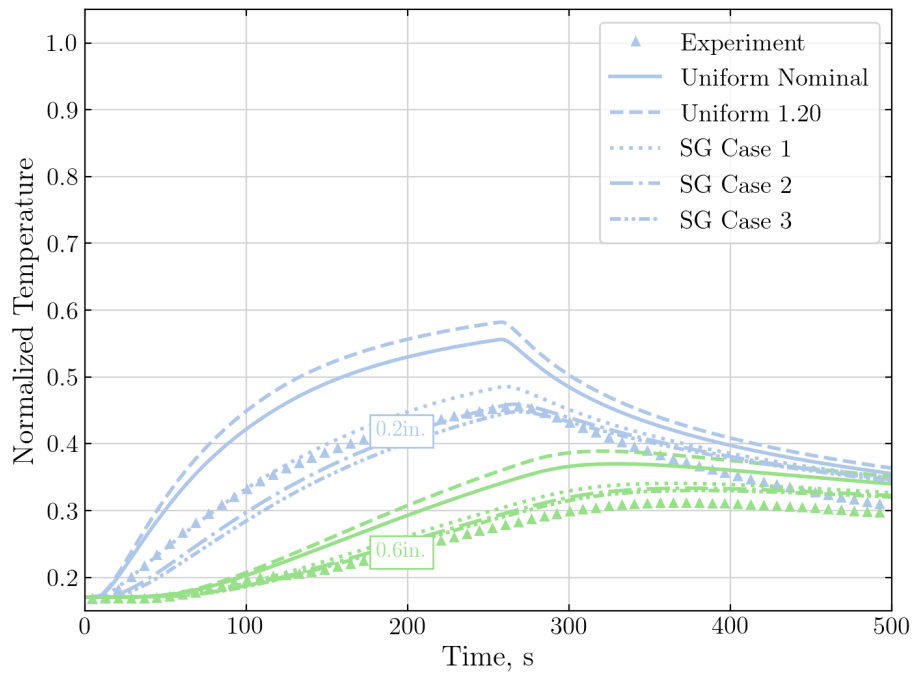
(d) 3.75 in. from centerline.

Figure 4.11: Comparisons of off-center TC predictions using SG heat flux profiles with experiment.

the total power is distributed to the insulation blocks. The current calculations using the elliptical spot beam size indicate that approximately 15% of the power is lost to the insulation blocks. In other words, under current calculations and assumptions, the HEEET panel experiences about 8.5 kW of power. This power divided by the width of the sample gives the area under the curve in the nominal and SG profiles shown in Fig. 4.10.

Instead of constraining the SG profile to 8.5 kW, the power constraint will be relaxed in the next study. Based on prior evidence, supplying additional power is expected to yield better agreement between predictions and measurements.

Figure 4.12 presents the results for simulations performed with a relaxed power constraint. The relaxed power SG profile corresponds to $n = 8$, $\sigma = 0.007$, which integrates to approximately 9 kW of power. This SG profile will be referred to as "SG Case 4." In contrast with SG cases 1-3, the current case is in much better agreement with the measurements from the shallow TCs at the first three off center locations. However, the accuracy at the 3.75 in. location has worsened.

These studies suggest that it is difficult to further improve agreement between simulation predictions and experimental measurements by only reconstructing the spatial heat flux distribution. In the next section, the material model is examined. The off-center analysis in the next section will use SG Case 4 as, comparatively, the predictions using SG Case 4 exhibits better agreement at the shallower locations.

4.2.1.4   Material model analysis

The preceding sections demonstrate that assessing only the surface model (i.e., BCs) limits the capability of the solver in achieving good agreement with experiments. This limitation is most significant for the deeper TCs as at these locations, the simulation prediction is much more sensitive to the material model than at the surface. The primary property of interest for the material model is the thermal conductivity,
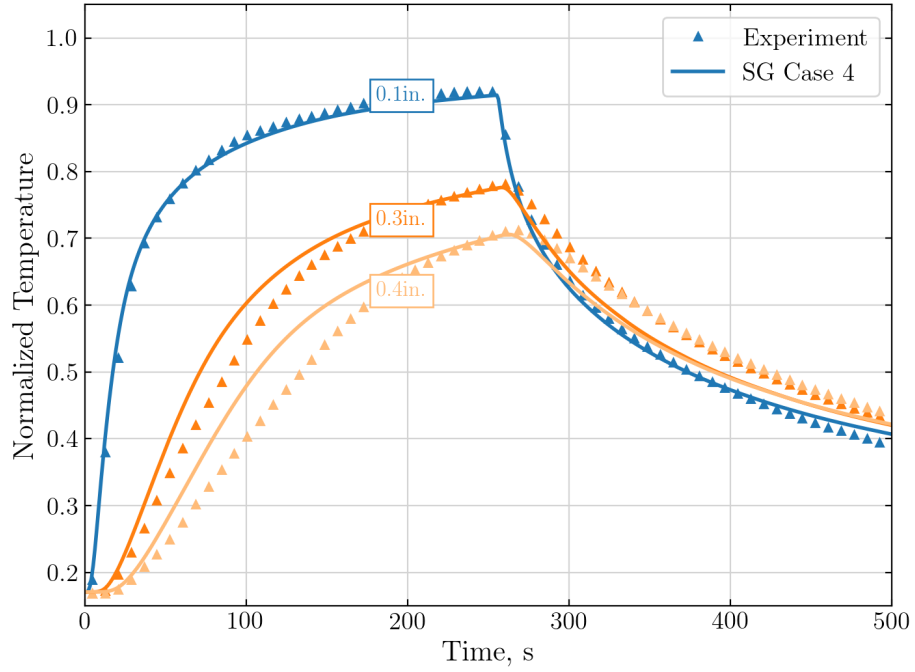
(a) 1.25 in. from centerline.
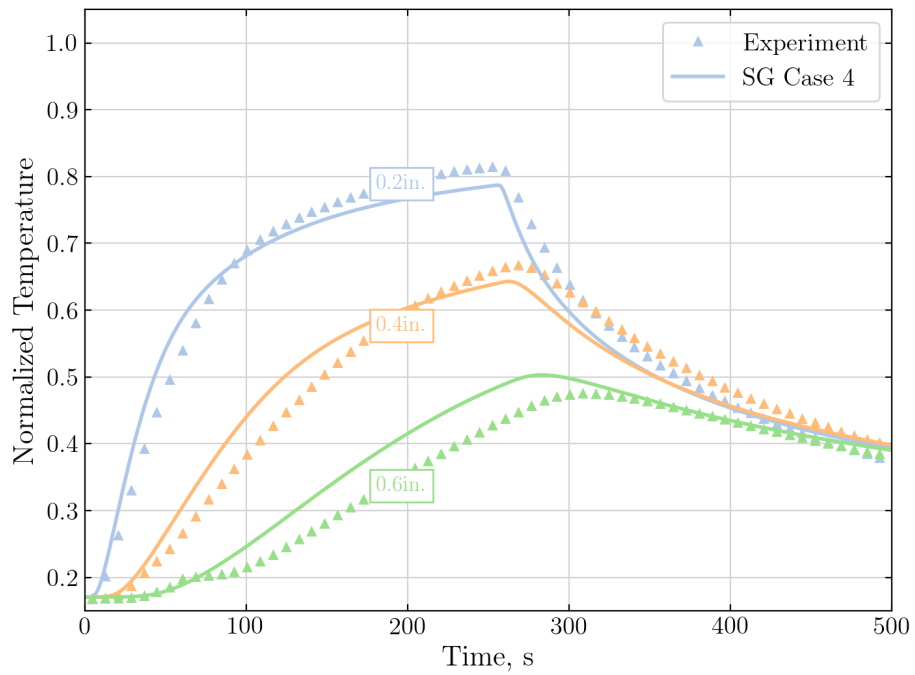
(b) 2.50 in. from centerline.

as it governs the in-depth heat transfer in both the TTT and IP directions.

As with all complex materials, there are a number of uncertainties in its material properties. This is especially true for HEEET as there are uncertainties associated
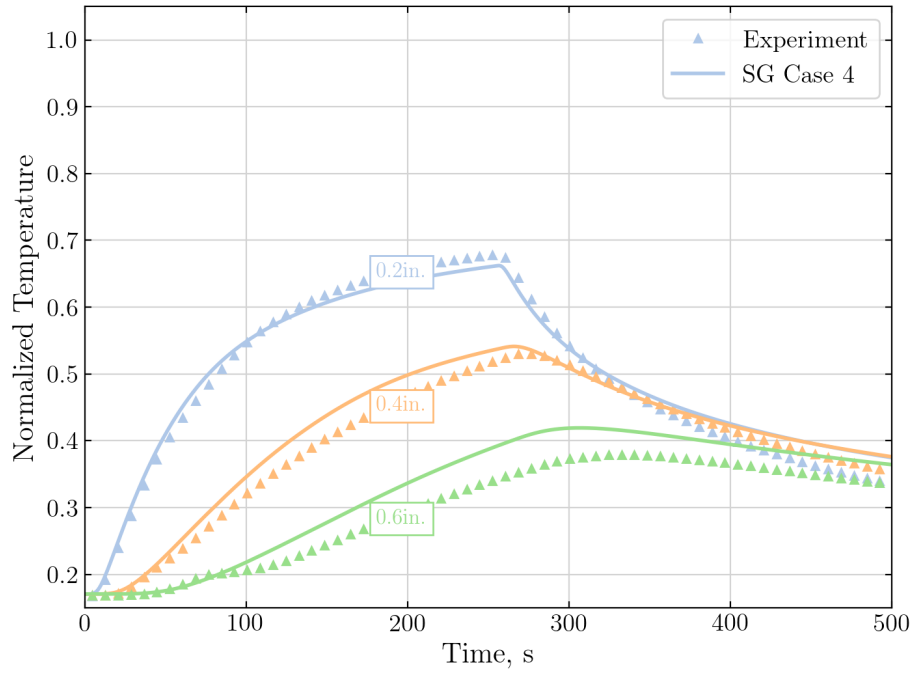
(c) 3.25 in. from centerline.
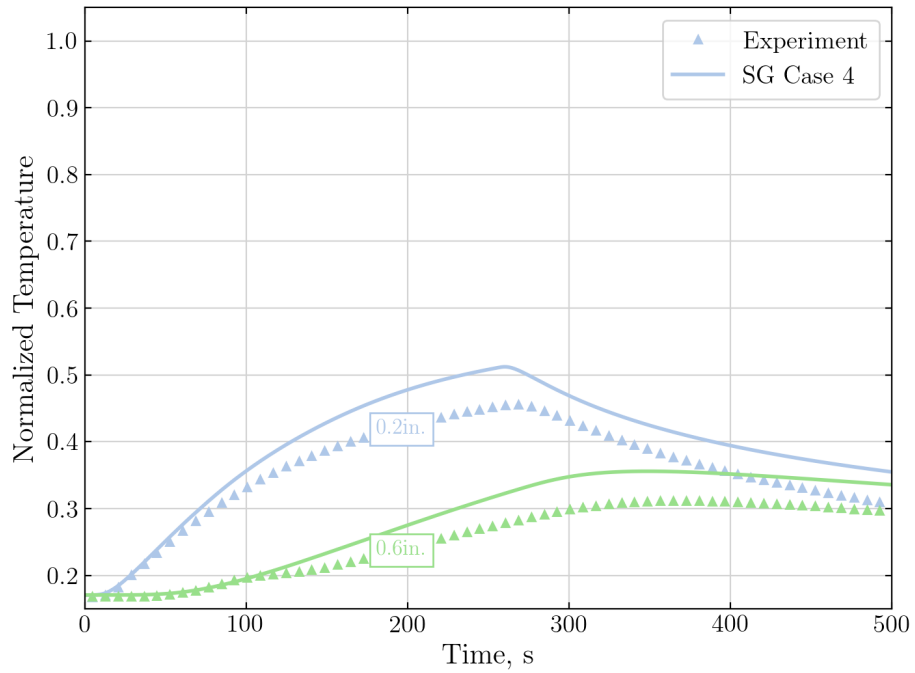
(d) 3.75 in. from centerline.

Figure 4.12: Comparisons of off-center TC predictions using SG heat flux profiles with relaxed power constraint.

with non-linearity in the conductivity as a function of temperature, extrapolation of current properties to high temperatures (i.e., current properties are experimentally characterized for temperatures under 1000K), the anisotropic nature, as well as significant differences between the virgin and charred material properties and coupon-to-coupon variability.

All of these features makes it very difficult to accurately measure the conductivity using direct measurements.

The conductivity values used in the inputs thus far are obtained from direct measurements from previous experiments (i.e., comparative rod apparatus and guard hot plate testing [2]). Direct measurement of the char conductivity introduces another uncertainty as the charred material being measured is often different than that of the actual char depending on the nature of the charring process. For example, baking the material in an oven until it is fully charred can lead to different measured values of charred conductivity than, say, measuring a fully charred material in an arc jet or in the LHMEL due to differences in the environments and heating rates.

In this section, numerical optimization is used to infer a set of conductivity properties to achieve better comparisons between simulation and measurements. The analysis can be formulated as a constrained optimization problem:

$$\arg\min_{\mathcal{M}} f(\mathcal{M}) \tag{4.3}$$

$$\mathcal{M} = \{\kappa_r\}_{j,k,\ell} \cup \{\kappa_i\}_{j,k,\ell}$$

$$\text{subject to } \kappa_i < \kappa_r \quad \forall i, j, k$$

where $f(\mathcal{M})$ is an objective function. In this case, the MSE cost function is used

$$f(\mathcal{M}) = \|T_e - Tp(\mathcal{M})\|^2 \tag{4.4}$$

---

[2]E. Stern, private communication, June 2020

where T_e and T_p are the experimental and simulated temperatures at depths shown in Fig. 4.5 and at times as determined by the TC readings. $\mathcal{M}$ is defined as a set of conductivities, where κ_r and κ_i represent the conductivity of the recession and insulation layers, and the subscripts j, k, ℓ index the temperature (discretized on the interval defined by the maximum and minimum temperatures), direction (warp, weft, TTT), and material state (virgin or char). That is, $\mathcal{M}$ is the set of recession and insulation conductivities over the orthotropic directions, discrete temperature values, and virgin or char material state. Tikhonov's regularization is not used for the final inference presented here as minimal overfitting is observed, and regularization studies do not result in appreciable changes in the results. The size of the dataset used for inference is $\sim \mathcal{O}\left(10^3\right)$, and the number of dimensions is $\sim \mathcal{O}\left(10^1\right)$.

Clearly, this is a high-dimensionality optimization problem, and the problem is very complex, with possibly many local optima. To simplify the problem and make the optimization problem more tractable, only the TTT conductivity is varied. In addition, the T_e and T_p are constrained to just the centerline measurements and predictions, which supports the simplification of fixing the IP conductivity from a physics-perspective, as the centerline is primarily 1-D, and IP effects are negligible as previously shown in Fig. 4.6. Finally, due to uncertainties in the TC measurements during the cooling phase, and the presence of an active nitrogen purge that may lead to unmodeled cooling effects, the dimensionality of the temperature dataset is reduced to measurements and predictions during the heating phase.

As an analytical solution to $T_p(\mathcal{M})$ is not known, and the gradient cannot be determined analytically, gradient-free optimization algorithms are used [40]. The Particle Swarm Optimization (PSO) method [41] is used here as it is embarrassingly parallel, which is extremely favorable for the current problem compared to a more sequential optimization strategy such as Bayesian optimization [42]. The embarrassingly parallel nature of PSO is particular advantageous here as the $T_p(\mathcal{M})$ in the objective function

is expensive to evaluate.

Each particle's location in the swarm, $\mathcal{M}_p$, is randomly initialized using a uniform distribution $\mathcal{M}_p \sim U(0.1\mathcal{K}', \mathcal{K}')$, where $\mathcal{K}'$ is the set of original TTT conductivity. Each particle moves around in the search space and each analyzes a candidate solution, and the swarm synchronizes periodically to communicate information between the particles. The process is iterative where each particle's movement is influenced by the local and global best known solutions.

As the objective function here is inherently a black box, it is not feasible to theoretically assess whether it is a convex function or not, and thus the PSO solution may be locally optimal, but not globally optimal. To mitigate this concern, numerous different random initializations are tested to observe whether the solution from the different initial conditions result in the same final solution. The study confirmed that all the trials resulted in the same solution, leading to more confidence in the determined solution.

The solution to the optimization problem results in approximately a 20-40% reduction in char and virgin TTT thermal conductivity of the recession and insulation layers over a temperature interval bounded by the initial and the radiative equilibrium temperature. A reduction in TTT thermal conductivity supports the previous observation where the simulation results exhibit a larger rate of increase in temperature for the majority of the heating phase.

The centerline comparisons using the inferred TTT conductivity are shown in Fig. 4.13 along with the former predictions, and the corresponding MSE are shown in Table 4.4. The predictions at the wall and at the 0.1 in. location are virtually the same as these locations are not particularly sensitive to changes in the material model. A significant improvement in accuracy is observed for comparisons at 0.2 in. and deeper locations. These locations are particularly sensitive to the material model as previously hypothesized. By reducing the TTT conductivity, the experimental

measurements and the simulation predictions now exhibit a similar rate of increase in temperature.
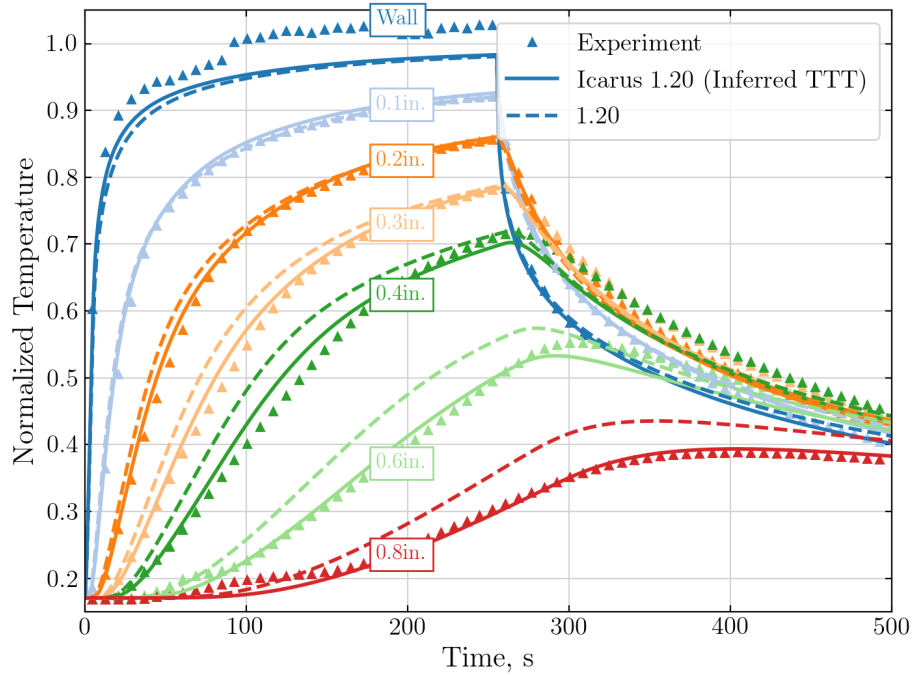
Figure 4.13: Comparison of simulation vs. experiment at the centerline using inferred TTT conductivity.

Table 4.4: MSE of centerline comparisons using inferred TTT conductivity for 10 kW case.

	Original		Inferred	
	Heating	Total	Heating	Total
0.1 in.	3.115e-05	1.661e-04	2.311e-05	8.133e-05
0.2 in.	2.314e-04	3.942e-04	3.522e-05	1.019e-04
0.3 in.	5.646e-04	8.519e-04	5.581e-05	2.680e-04
0.4 in.	1.085e-03	1.484e-03	1.361e-04	5.640e-04
0.6 in.	1.151e-03	1.449e-03	3.374e-05	3.109e-04
0.8 in.	2.559e-04	1.475e-03	7.075e-05	7.861e-05

The inferred TTT conductivity, as well as the SG case 4 profile determined in the previous section, are then used to analyze the off-center comparisons. The results are presented in Fig. 4.14. The predictions using a uniform profile and a SG profile with the inferred TTT conductivity are in better agreement with experimental

measurements at deep TC locations; however, the agreement at the 0.2 in. depth TCs has worsened when compared to Fig. 4.12. This is not surprising as the 0.2 in. depth is sensitive to the material model, and by reducing the TTT conductivity, the temperature predictions at the 0.2 in. location have decreased. From these figures, the net increase in accuracy in the comparisons at the off-center locations appears to be minimal when only using the reconstructed spatial heat flux profile and inferred TTT conductivity.

In addition to the spatial heat flux profile and TTT conductivity, the IP conductivity is expected to play a role in the off-center predictions. It is not clear whether increasing or decreasing the IP conductivity would increase or decrease the off-center temperature predictions. For example, without loss of generality, at the 1.25 in. location, there are two competing conductive heat transfer processes. First, an increase in temperature is expected due to the conductive heat transfer from a hotter centerline region to the cooler 1.25 in. region. Second, a decrease in temperature is expected due to the conductive heat transfer from the hotter 1.25 in. region to further off-center. Increasing the IP conductivity would strengthen both of the competing processes, and the net outcome is uncertain.

The optimization problem converges to a solution where the inferred recession layer's virgin and char IP conductivity is approximately half that of the original IP conductivity across the entire temperature domain. The results appear to not be very sensitive to small changes in the IP conductivity, and a comparatively (to that of the TTT scaling) large correction is needed to observe a discernible change. In addition, the optimization algorithm indicates that the results are not sensitive to changes in the IP conductivity of the insulation layer. This is reasonable as all of the TCs are located in the recession layer, except for the 0.6 in. TCs which are located near the recession-insulation layer interface. In Fig. 4.15, the comparisons are shown for the SG Case 4 predictions using the inferred TTT conductivity for two IP conductivity
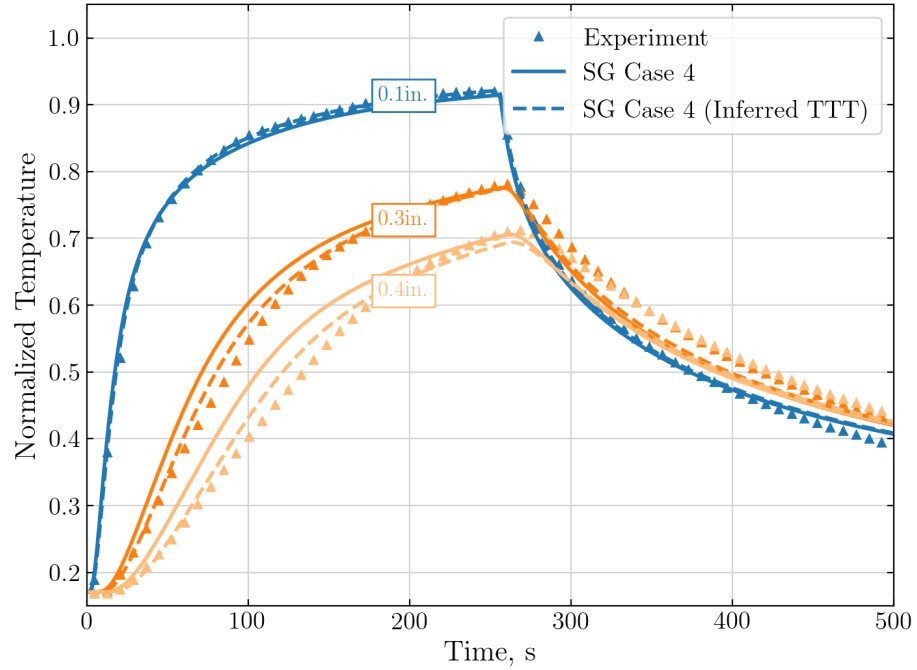
(a) 1.25 in. from centerline.
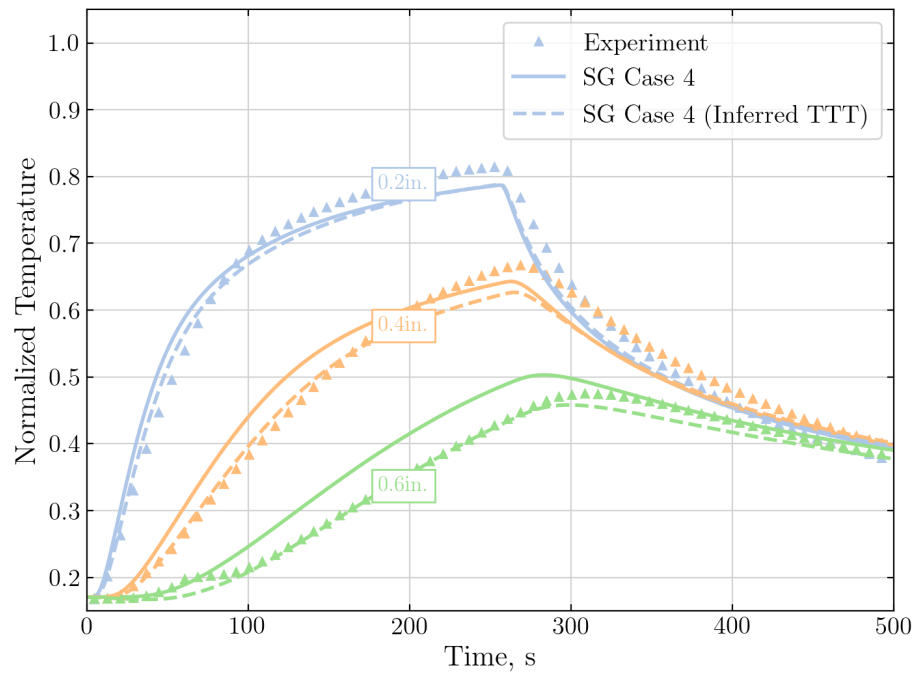
(b) 2.50 in. from centerline.

scaling factors: 0.5 and 1.5. The predictions using the 0.5 IP scaling generally yields the best agreement with experimental results.

Several interesting attributes are evident in Fig. 4.15. First, at the first two
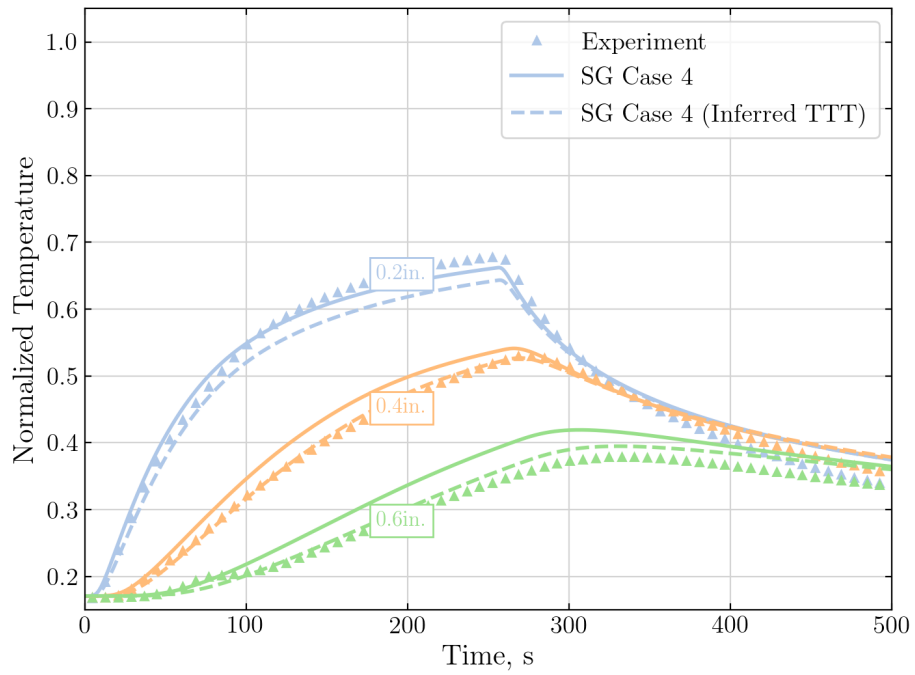
(c) 3.25 in. from centerline.
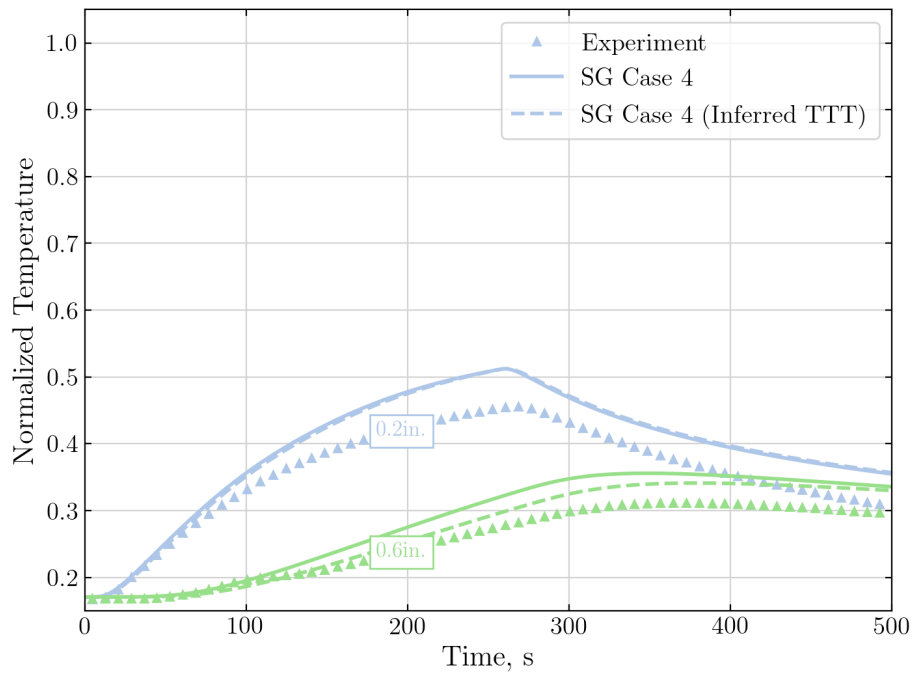
(d) 3.75 in. from centerline.

Figure 4.14: Comparisons of off-center TC predictions using inferred TTT conductivity.

off-center locations, decreasing the IP conductivity results in an increase in temperature across all depths and times. This suggests that the reduction in conductive heat transfer to the first two off-center locations outweighs the reduction in conductive heat transfer away from these locations. On the other hand, increasing the IP conductivity results in a decrease in temperature, suggesting that the increase in conductive heat transfer to these locations outweighs the conductive heat transfer out of these locations. For the last two off-center locations, the opposite trend is observed. Interestingly, the comparisons at the 3.25 in. location suggest that the simulation predictions are not sensitive to changes in the IP conductivity. This is likely due to the two competing IP conduction mechanisms cancelling each other out at this location.

A reduction in the char and virgin TTT conductivity of both the recession and insulation layers results in improved agreement along the centerline, and off-center comparisons are further improved by a reduction in the char and virgin IP conductivity of the recession layer. In total, the material model analysis suggests that a reduction to the original values of the TTT and IP conductivity is appropriate when modeling HEEET. Due to the expected sensitivity of the char properties to the heating rate, the inference performed in this section is susceptible to overfitting [43], and validation of the inferred properties is needed to assess its generalizability to other heating rates.

4.2.2   20 kW Case

In this section, the 20 kW case is used to assess the inferred properties from the 10 kW case. This type of validation is commonly known as hold-out cross-validation, and in this work, it is the first part of the k-fold cross-validation process [44]. The 20 kW case, shown in Fig. 4.2, exhibits a relatively more complex heating profile than that of the 10 kW case due to an additional power ramp later in the experiment.
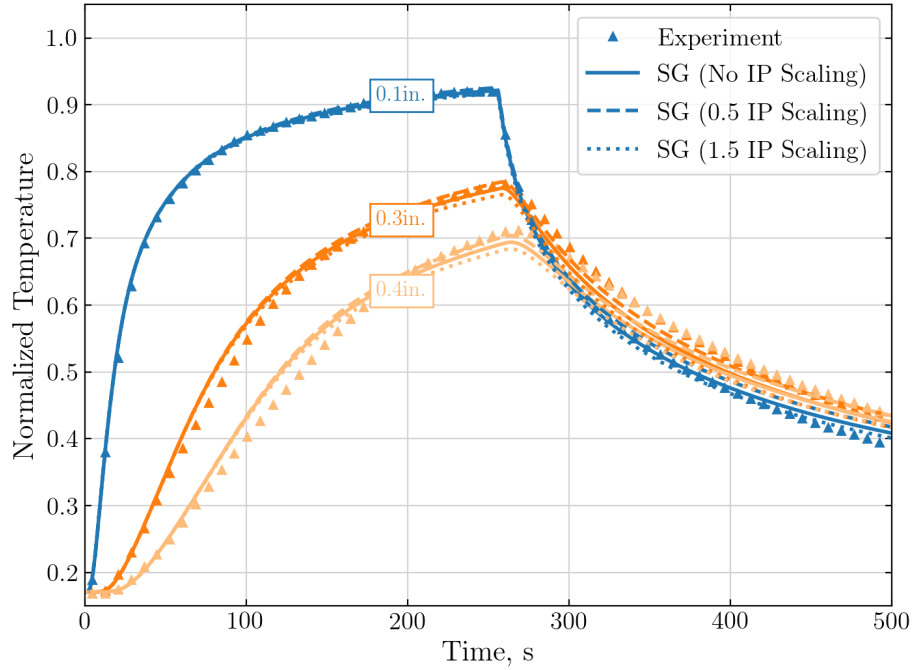
(a) 1.25 in. from centerline.
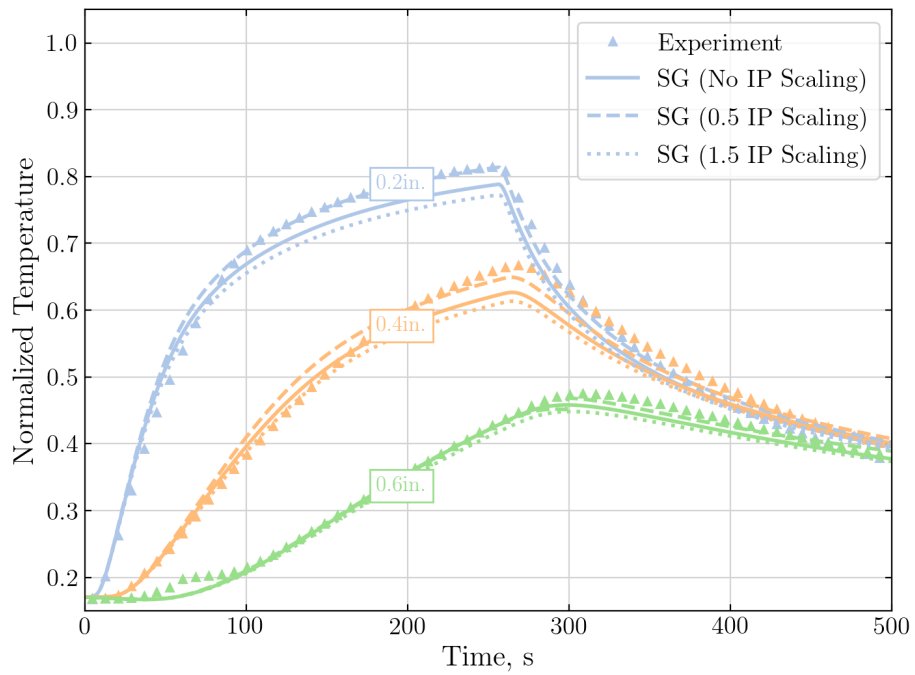
(b) 2.50 in. from centerline.

Figure 4.16 presents the centerline comparisons between Icarus and experimental measurements. Again, the nominal heat flux input results in underpredicting the temperature at the top level TC locations. An Infrared (IR) camera was used to record
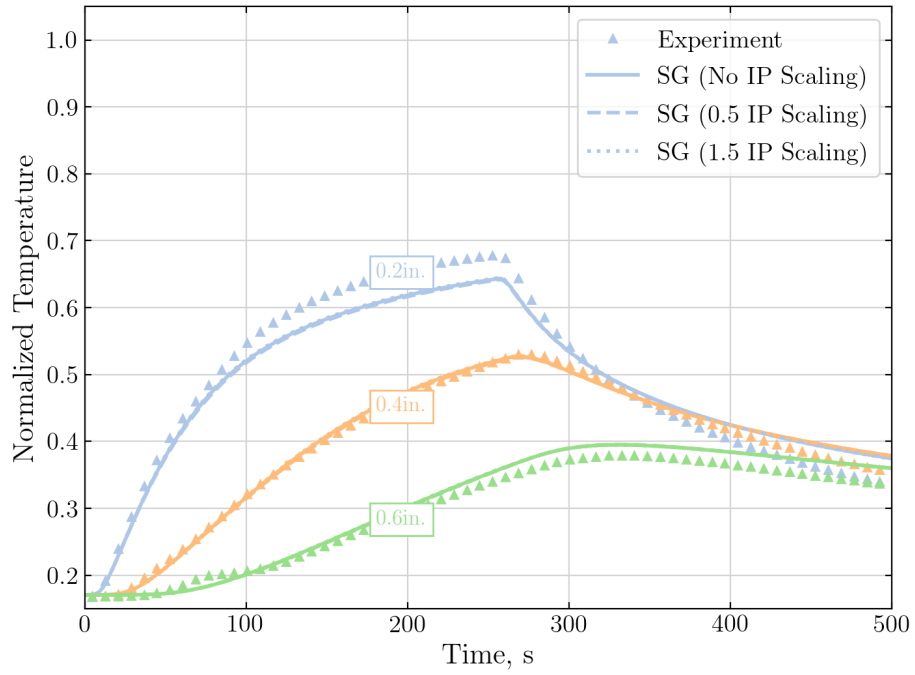
(c) 3.25 in. from centerline.
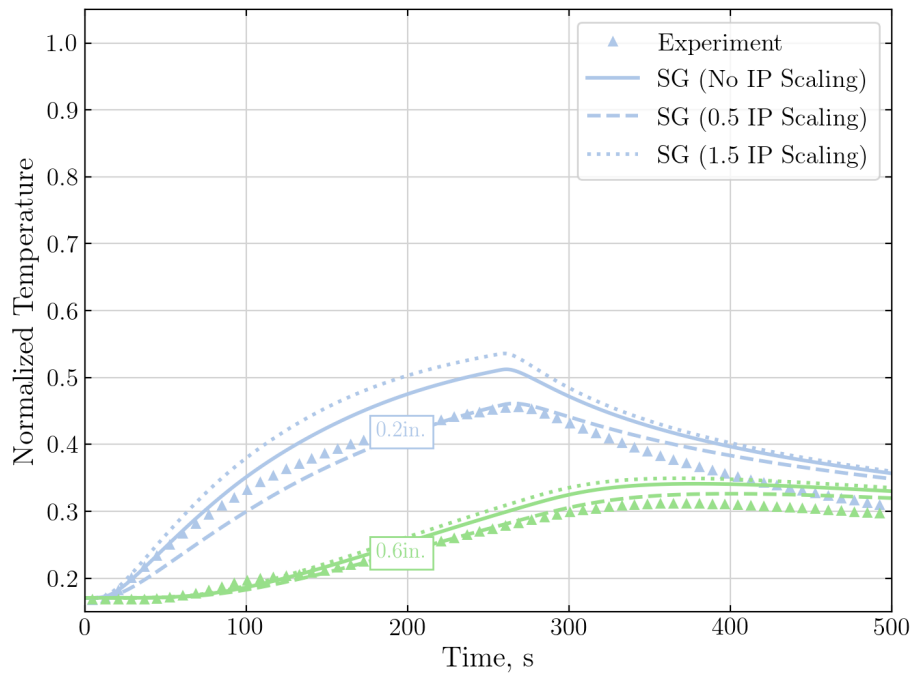
(d) 3.75 in. from centerline.

Figure 4.15: Comparisons of off-center TC predictions using inferred IP conductivity.

the centerline surface temperature for the 20 kW panel in the LHMEL experiment; however, the sharp and flattened top suggests that saturation occurred. A 20% correction in the centerline radiative heat flux again results in the most optimal agreement at the top level TC locations. The repeatability instills some confidence in the correction factor determined previously.

Figure 4.17 presents the centerline comparisons using the inferred TTT and IP conductivity determined from the 20 kW studies. By using the previously inferred properties for the 20 kW case, the agreement between the simulation predictions and experimental measurements have improved significantly. For all TC locations, the MSE between the measurements and predictions decreased by an order of magnitude.

The off-center comparisons are also analyzed for the 20 kW case. The SG parameters used here is $n = 8, \sigma = 0.008$. Figure 4.18 presents the comparisons between the experimental measurements and simulation results at the off-center locations. Here, "SG" indicates the simulation results using the SG heat flux profile with the original conductivity. Similar to the results in the 10 kW case, gradual improvements in the comparisons between the simulation predictions and experimental measurements is observed using the inferred radiative heat flux profile, inferred TTT conductivity, and inferred IP conductivity.

The above validation completes half of the validation process. It demonstrates that the inferred TTT and IP conductivity from the 10 kW case can be confidently generalized to this higher power case. To complete the cross-validation process, the 20 kW case is used for inference of the TTT and IP conductivity, and the resulting inferred properties are validated using the 10 kW case.

The solution to this case is found to converge to approximately the same TTT and IP conductivity as the 10 kW case. The maximum difference between the TTT and the IP conductivity for the 10- and 20 kW cases are only 1% and $4 - 8\%$, respectively. The change in MSE for the 10- and 20 kW cases using the newly inferred conductivity
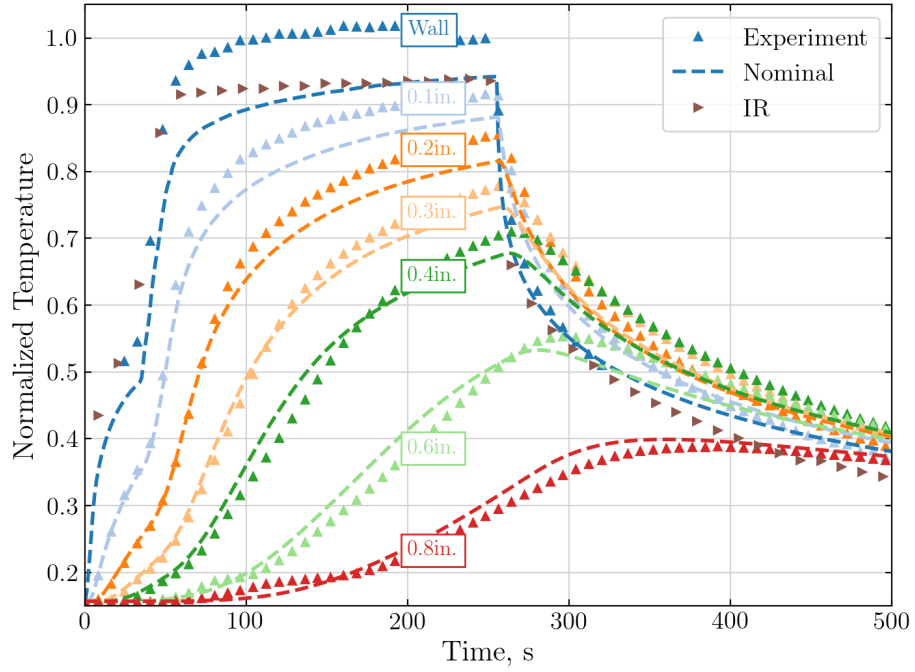
(a) Icarus Nominal vs Experiment.
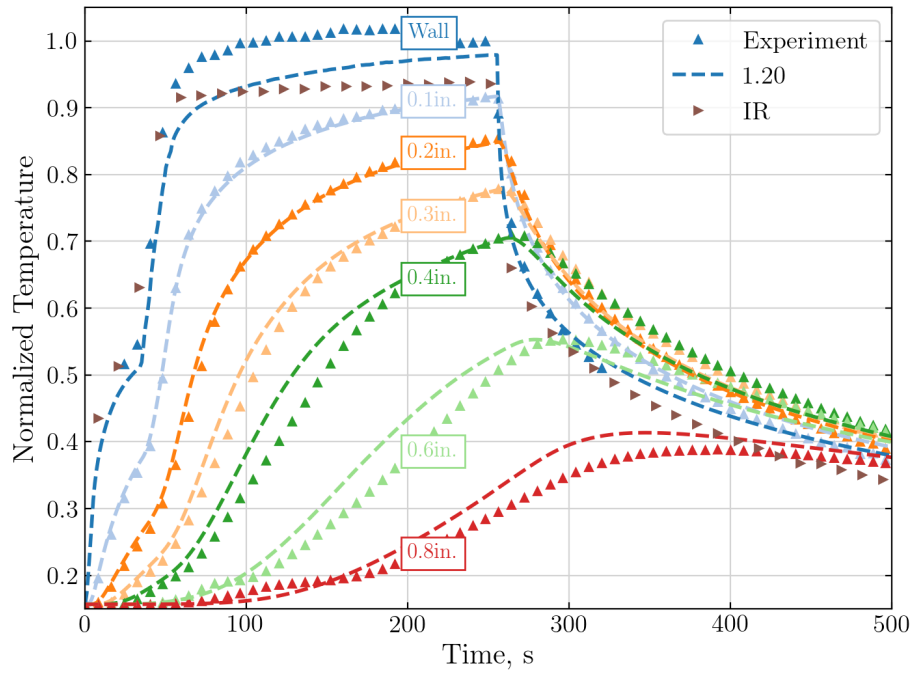
(b) Icarus 1.20 vs Experiment.

Figure 4.16: Comparison of FIAT vs. Experiment for 20 kW case.

is under 5% at all locations.

This is not a surprising result given that the initial 20 kW results show that the
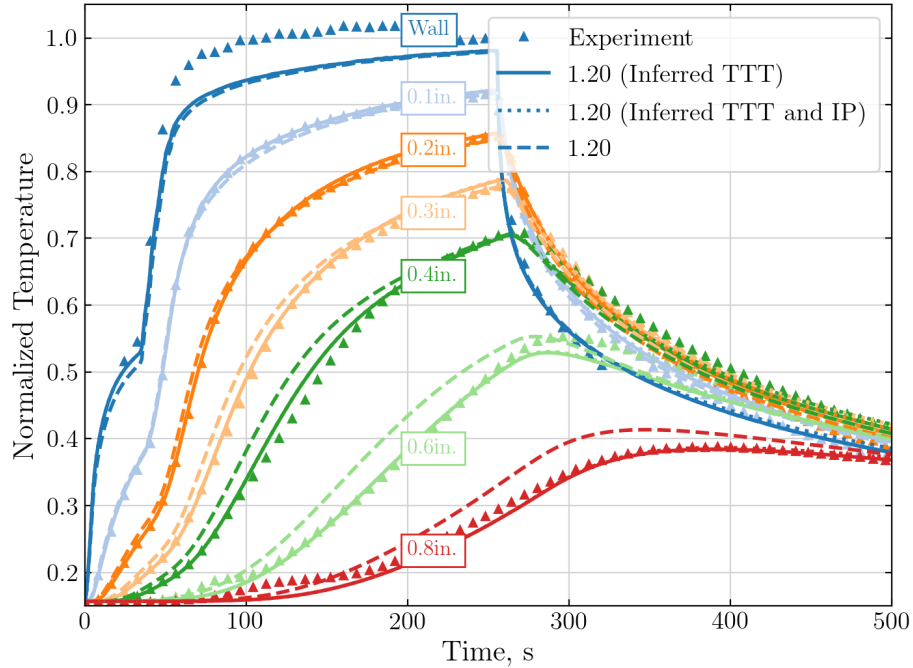
Figure 4.17: Comparison of simulation vs. experiment at the centerline for 20 kW case using inferred TTT conductivity.

properties inferred from the 10 kW case generalizes to the higher power case. The optimization problem for both cases independently converging to approximately the same conductivity suggests that the conductivity found is indeed a global optima, and not a local optima. In addition, these results suggest that the char conductivity may be independent of the heating rate under the simulated conditions, but care needs to be taken when extrapolating the usage of the inferred properties to significantly larger heating rates.

4.3 Chapter summary

A computational analysis for the thermal response modeling of the Heatshield for Extreme Entry Environment Technology (HEEET) was presented. The 3-D finite volume material response code, Icarus, was used to model the Laser Hardened Materials Environmental Laboratory (LHMEL) testing of the HEEET, a dual-layer woven
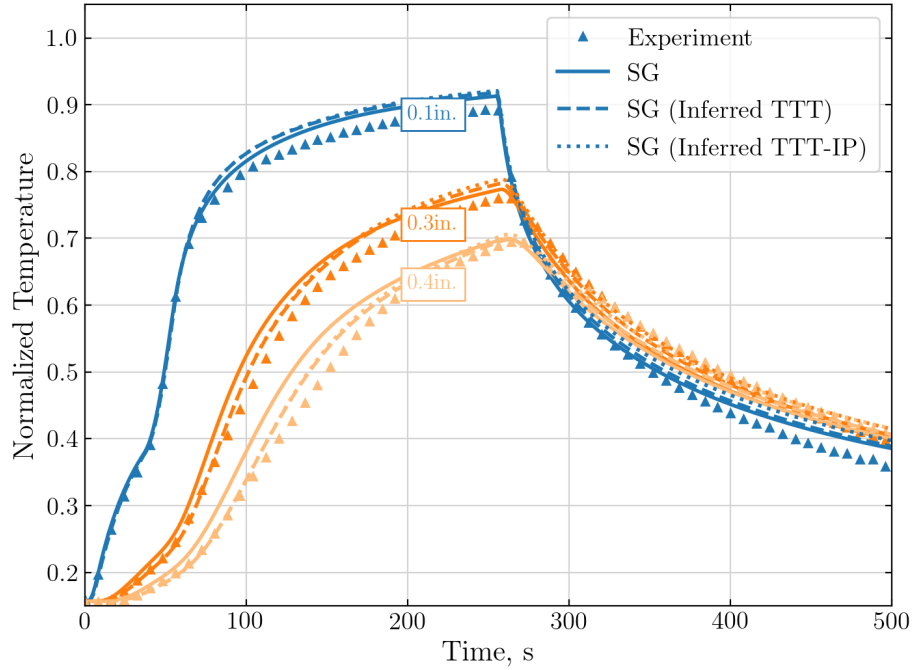
(a) 1.25 in. from centerline.
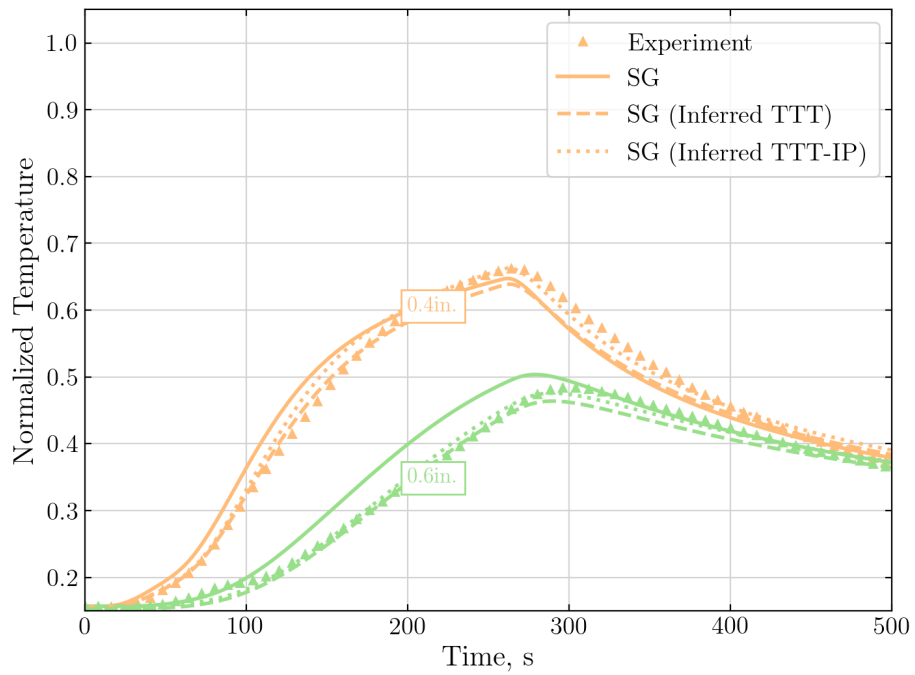
(b) 2.50 in. from centerline.

thermal protection system (WTPS), for a 10 kW and 20 kW laser power experiments. 1-D verification studies comparing Icarus, a 3-D material response code, and FIAT, a 1-D material response code, demonstrated that the two solvers are in close agreement
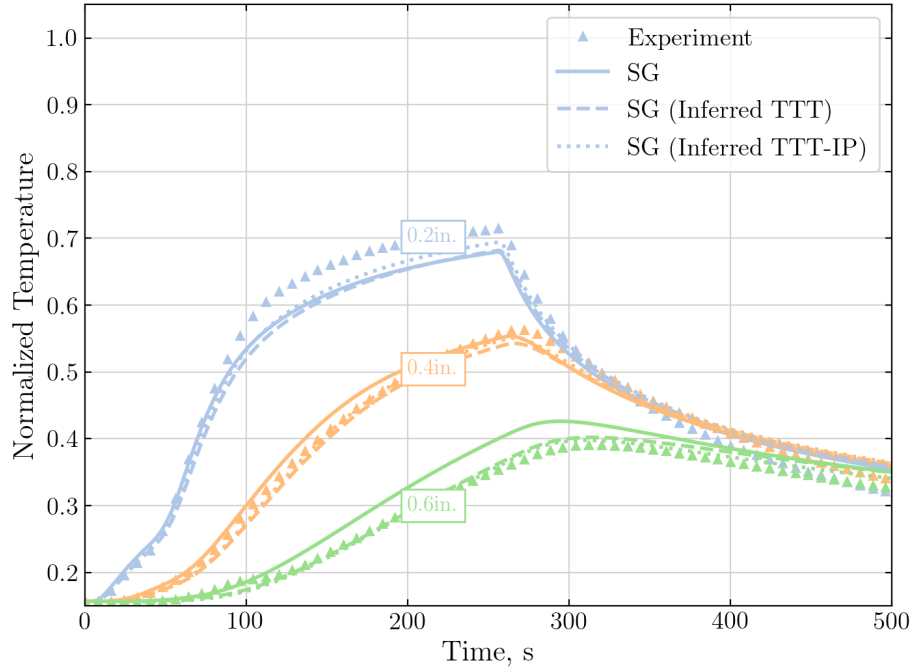
(c) 3.25 in. from centerline.
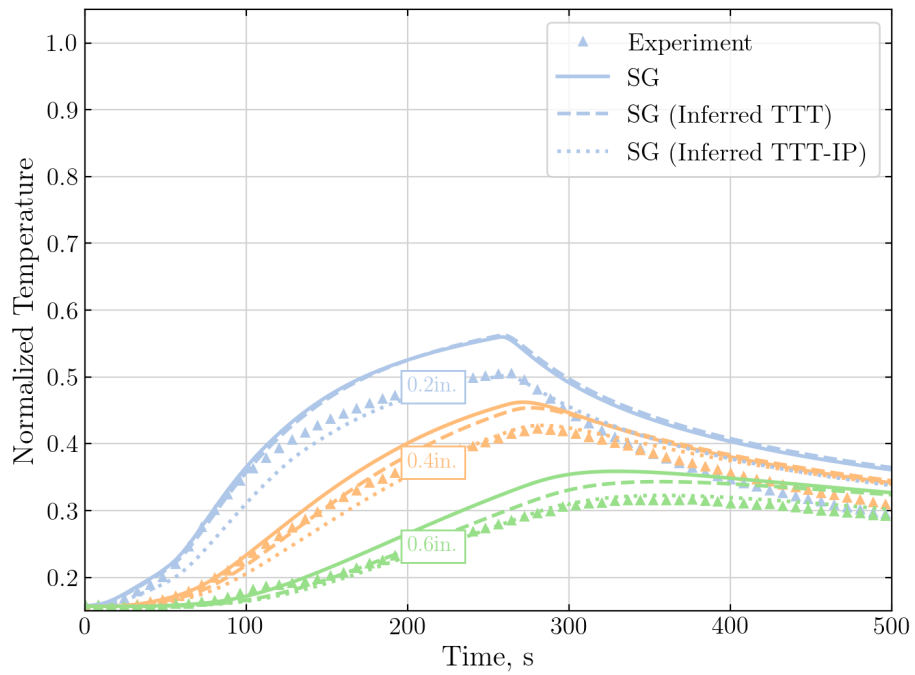
(d) 3.75 in. from centerline.

Figure 4.18: Comparisons of off-center TC predictions for 20 kW case with experiment.

when pyrolysis gas transport is neglected.

Icarus predictions for the 10-kW LHMEL testing of HEEET showed that the nominal radiative heat flux Boundary Condition (BC) computed from the experimental power measurements resulted in underpredictions of the centerline temperatures. Increasing the nominal heat flux by 20% resulted in much approved agreement with experimental measurements for top level thermocouple (TC) measurements. However, Icarus predictions overestimated the temperature at deeper TC locations, as well as at off-center locations.

Optimization and cross-validation were applied to the surface and material models to improve the agreement between simulation predictions and experimental measurements. The first of these techniques explored the use of a strain gauge (SG) spatial heat flux profile, which resulted in improved agreement with experimental measurements at off-center locations. The second technique explored the inference of the Through the Thickness (TTT) conductivity using cross-validation. A 20-40% reduction in char and virgin TTT conductivity of the dual-layer material resulted in greatly improved agreement for in-depth temperature predictions and measurements at the centerline. However, both of these revised models and their combined effects exhibited limited impact on the accuracy of off-center in-depth predictions. As a result, In Plane (IP) conductivity was also reevaluated. A 50% reduction in char and virgin IP conductivity of the recession layer resulted in appreciable improvement for off-center in-depth predictions.

The inferred properties derived from the 10 kW case were then applied to the 20 kW experiment. The same 20% correction factor to the nominal heat flux was determined to be valid for the 20 kW case. In addition, using the inferred TTT conductivity from the lower power case resulted in improved agreement with experimental measurements at the centerline, as well as at off-center locations. Cross-validation showed that the conductivity independently inferred from both cases are approxi-

mately identical, instilling confidence that the results are general and not overfit to the dataset used for inference.

There are several key takeaways from the analyses in this chapter. First, the analyses demonstrated that the previously experimentally determined thermal conductivity may not accurately describe the current HEEET material under the LHMEL heating conditions, which is an observation consistent with one of the greatest uncertainties and challenges in TPS modeling, in that temperature-dependent properties are dependent on the rate of heating and environmental conditions. Second, the analyses provided a set of temperature-dependent thermal conductivity results that, when used in simulation models, lead to much improved agreement with experimental measurements at two disparate power levels. The HEEET is a complex material, and it is imperative to assess the material under different heating conditions. The newly inferred properties are critical for improved modeling capabilities for future HEEET research and design, particularly in a radiative heating environment.

CHAPTER V

Structural Response Modeling

The analysis in this chapter focuses on modeling the experiments conducted by the HEEET team at the LHMEL facility at the Wright Patterson Air Force Base. Multiple rounds of LHMEL testing were conducted in 2017 and 2018 that focused on thermal, structural, and combined thermo-structural loading of HEEET panels. These experiments provide a rich suite of experimental data for evaluating the structural, thermal, and coupled thermo-structural modeling. The panels tested in 2017 were manufactured from a 13 inch weave while the panels in 2018 were manufactured from a 24-inch weave with tighter threading. The differences in the manufacturing processes and the ability to manufacture longer weaves likely imply that the stiffness properties could have changed, which will be a key area of interest for these studies.

In this chapter, the focus is on comparisons of the simulation results with the 2018 four-point-bending experiments of the 24-inch weave, which provide a more comprehensive and reliable set of measurements for assessing the structural solver. The HEEET project developed a four-point-bending apparatus for use within a seven by nine foot vacuum chamber in LHMEL to subject a HEEET panel to mechanical loading.

Four structural HEEET warp panels were tested and are shown in Table 5.1. The term "structural" here is used to differentiate the panels subjected to mechanical

loading from panels subjected to combined or only thermal loading. The term "warp panel" refers to a HEEET panel where the long direction of the panel is aligned with the warp direction (i.e., lengthwise direction of the threaded weave). Structural panels 01 and 04 are the only panels subjected to mechanical loading, and are therefore the only panels of focus for the pure structural response modeling. Both of these panels were subjected to identical mechanical loading conditions with the exception that Structural Panel 04 was subjected to two ramped mechanical loads whereas Structural Panel 01 was only subjected to one.

Table 5.1: Experimental test matrix of structural warp panels

Panel	Mechanical preload
Structural Panel 01	Yes
Structural Panel 02	No
Structural Panel 03	No
Structural Panel 04	Yes

The experimental setup is shown in Figs. 5.1-5.2. Here, the four-point-bending test fixture contains a load platform at the bottom with an instrument lift. The load actuator, with a peak load capability of 2698 lb, is controlled through a displacement channel. Both a fixed and moving frame are used for outer and inner load points, respectively. The inner load points displace into the sample on the insulation surface, while the outer load points remain stationary normal to the surface of the recession layer of the HEEET panel. This setup is very similar to that of a classical simply supported beam with two point loads.

For Structural Panels 01 and 04, an initial preload is applied. The preload is maintained until it is later ramped up by a factor of five. Two strain gauges (SGs), SG6 and SG7, are situated on the recession surface, outside of the laser impact region. Five SGs, SG1-SG5, are situated on the insulation surface. Lastly, five Linear variable differential transformers (LVDTs) are situated on the back surface.
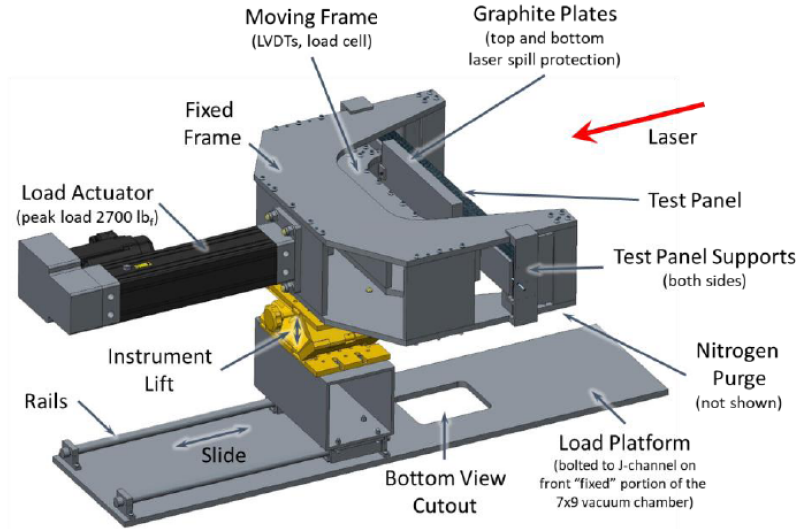
Figure 5.1: Experimental configuration for LHMEL test of HEEET [7].
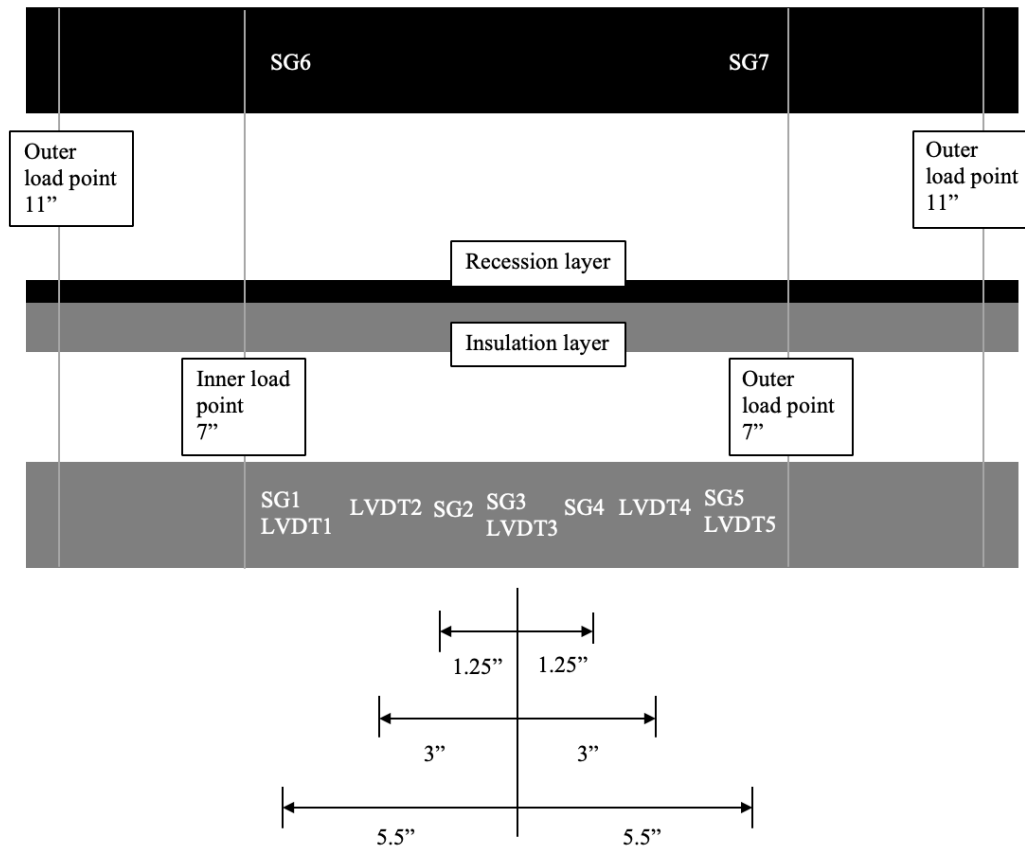
Figure 5.2: Experimental apparatus locations for LHMEL test of HEEET.

5.1 Structural response model setup

In the analysis, the structural response of the structural HEEET panel under mechanical loading is modeled independently of the thermal response. The small

deformation assumption of the governing equations is valid for modeling the experiment because the load applied is small and the material is relatively stiff, so very small deformations are expected.

The modeling is performed using the linear elasticity solver described in Chapter II. The model and boundary conditions are similar to that of a simply supported beam, where the two outer load points are modeled as fixed and roller supports. The roller support is prescribed a zero displacement component along the normal direction and unspecified in the planar directions. The traction components are prescribed in the planar directions and unspecified in the normal direction. The two inner load points are modeled using a traction BC, where the compressive force is given by the experimental measurements. The stiffness properties used for the initial simulations are from the 13 inch weave database as the stiffness properties for the 24-inch did not exist during the initial stages of modeling.

5.2 Strain results

The structural response results for the mechanical strain are shown in Fig. 5.3. These results are generated from the preload conditions. The strain is normalized by the magnitude of the maximum strain observed. Two of the strain gauges on the insulation surface in Fig. 5.2 (SG2 and SG4) did not register readings throughout the experiment.

A region of approximately constant strain between the inner load points on both the recession and insulation surfaces is observed in the simulation results. The disparate material properties of the insulation and recession layers is numerically manifested in the magnitude of the mechanical strains, where the insulation surface is deforming more than the recession surface in the region of constant strain. The magnitude of these results is expected because the recession layer is significantly stiffer. The constant strain is observed until the inner load points, where increased defor-

mation is observed on both the recession and insulation surfaces before decreasing to zero in the proximity of the outer load points.

The predicted strain on the insulation surface is in close agreement with the experimental measurements. Note that there is some asymmetry in the experimental results, which is likely attributed to apparatus tolerance and some degree of asymmetry in the experimental setup. On the recession surface, the model considerably over-predicts the strain by 70-80%.

The disparity is likely attributed to the use of the 13 inch weave properties, where it is evident that the 13 inch properties cannot be confidently extrapolated to a 24-inch material. When the 24-inch panels were woven, the manufacturing process allowed for a tighter weave than that of the 13 inch weave. Naturally, the stiffness of the 24-inch weave should be greater, which would result in smaller strain predictions.

5.3 Inverse analysis of stiffness properties

To infer a set of stiffness properties for the 24-inch weave, an inverse analysis using mathematical optimization is performed. The optimization seeks to find scaling factors, α_r and α_i, for the stiffness properties of the insulation and recession layers, respectively, that minimizes the MSE between the experimental measurements and the simulation predictions

$$\underset{\alpha_r, \alpha_i}{\arg\min} \, ||S_e - S_p(\alpha_r, \alpha_i)||^2 \tag{5.1}$$

where α_r and α_i are the hyperparameters and S_e and S_p are the experimental and predicted strain.

For the analysis, the same scaling factor is applied to the elastic modulus in all three orthotropic directions for both the recession and insulation layers. This implicitly assumes that the Poisson's ratio is constant, which, according to HEEET

94

experimentalists, are expected to remain constant.

Rather than biasing the inference towards only measurements taken at the preload, a more generalized approach is taken. The sample space for the optimization is increased to include the five SG measurements acquired from ramping of the load from zero to the preload. For example, the MSE defined for a given SG is

$$MSE = \frac{1}{n} \sum_{f \in \mathcal{F}} (S_e(f) - S_p(f))^2 \tag{5.2}$$

where $S_e(f)$ and $S_p(f)$ are the experimental and simulation response of a SG to some applied force in the set $\mathcal{F} = \{0, f_1, \cdots, f_p\}$, where f_p is the preload. The largest discrepancy between the experimental measurements and simulation results is on the recession surface, so the optimization strategy is primarily focused on inferring its properties. To avoid overfitting the experimental measurements, only Structural Panel 01 measurements are used in the inference.

Some examples of the optimization trajectory are shown in Tables 5.2 and 5.3. Note that Table 5.3 serves as validation of the inferred scaling factors as Structural Panel 04 measurements are not used in the inference procedure. The first column shows the scaling factor applied to the stiffness properties of the recession and insulation layers, and the remaining columns show the MSE associated with each SG. The first row shows the MSE of the results presented in Fig. 5.3. As the scaling is increased for the recession surface, the MSE decreases. The effects of the scaling are most prominent in the last two columns, which correspond to the SGs situated on the recession surface. This is intuitive as the SGs on the insulation surface are not as sensitive to changes in the recession layer properties. The scaling factors in the last row meet the criterion for termination of the optimization algorithm (i.e., all MSEs must be less than 6.). Further optimization would lead to diminishing returns and overfitting and therefore is not worth pursuing especially given the uncertainties in the experimental apparatus, which are evident in the differences of the Structural 01

95

and 04 measurements even though the two panels are subject to the same loading during the experiment. The terms "nominal properties" and "updated properties" will be used in the remainder of the chapter to refer to the properties derived from the 13 inch weave and properties generated from the scaling in the first and last rows of Tables 5.2 and 5.3, respectively.
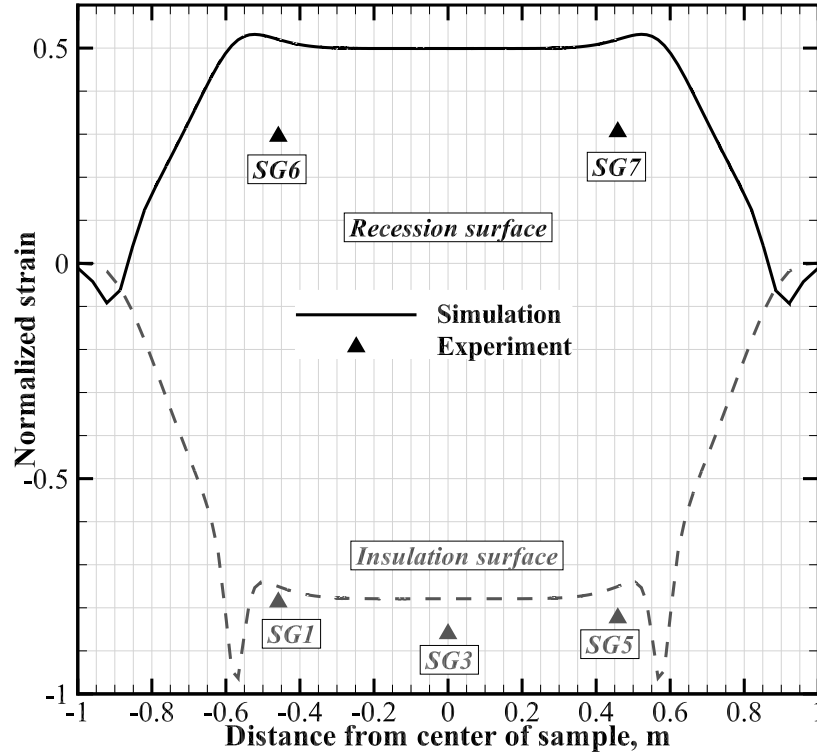
Figure 5.3: Predicted and measured strain along the length of the sample.

The evolution of the strain gauge measurements as the mechanical load is increased is shown in Fig. 5.5. The figure presents the comparison of the SG measurements with predictions on the insulation surface. The results for both structural panels under mechanical loading are presented here. As expected, the simulation results generated using nominal properties exhibit a steeper decrease in strain than those of the updated properties. The increased stiffness of the recession layer's weave yields a shallower slope as the material is less susceptible to deformation.

Even though SG1 and SG5 are symmetrically situated, as shown in Fig. 5.2,

Table 5.2: MSE $[10^{-4}]$ between Structural panel 01 measurements and simulation predictions

Scaling (recession|insulation)	SG1	SG3	SG5	SG6	SG7
1.0|1.0	95.8	27.6	30.5	285	235
1.3|1.0	57.8	10.6	11.1	120	87.9
1.5|1.0	42.8	5.86	5.37	66.8	43.6
1.9|1.0	24.8	3.15	1.24	18.2	7.21
1.9|0.9	81.2	24.3	22.5	25.3	11.9
2.3|0.9	59.6	14.1	12.0	5.79	0.89
2.3|1.0	15.0	4.57	1.79	3.11	0.39
2.3|1.1	4.02	2.74	1.94	1.69	0.86

Table 5.3: MSE $[10^{-4}]$ between Structural Panel 04 panel measurements and simulation predictions

Scaling (recession|insulation)	SG1 %	SG3 %	SG5 %	SG6 %	SG7 %
1.0|1.0	50.0	50.3	59.3	130	126
1.3|1.0	27.1	27.3	33.9	40.6	38.4
1.5|1.0	18.5	18.6	24.1	16.3	14.8
1.9|1.0	8.87	8.7	12.5	0.91	0.54
1.9|0.9	41.1	46.3	49.6	2.16	1.57
2.3|0.9	28.2	3.26	3.51	1.63	1.80
2.3|1.0	4.29	3.83	6.53	3.32	3.69
2.3|1.1	3.21	2.04	1.54	5.34	5.87

the experimental measurements for Structural Panel 01 show that the difference between the two measurements increases almost monotonically as mechanical loading increases. This is not observed in Structural Panel 04. If the difference between the SG1 and SG5 measurements remained relatively constant across all loading, then the difference is likely explained by apparatus tolerance and rig compliance. However, the presence of a non-constant and increasing difference may be indicative of non-uniformity in the warp direction's structural properties in the Structural Panel 01 panel, asymmetry in the panel geometrically, or asymmetry in the experimental setup for Structural Panel 01.

Figure 5.6 presents the analogous results for the recession surface. Once again,

the symmetrically situated SG6 and SG7 exhibit a growing difference in their measurements as load is increased for Structural Panel 01. Again, this is not observed in the measurements for Structural Panel 04.
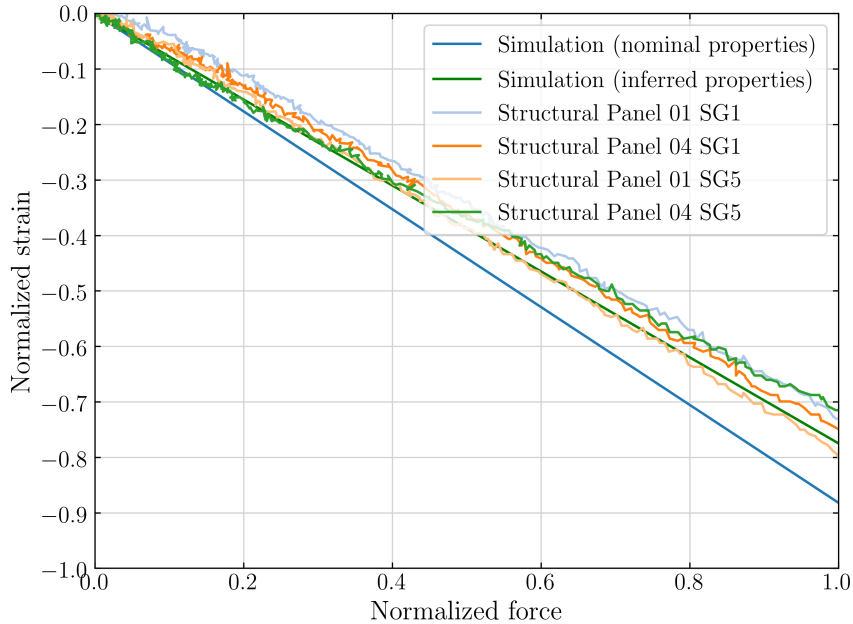
Figure 5.4: Comparisons of strain gauge measurements with predictions at SG1 and SG5 locations.

5.4 Deflection results

Figure 5.7 shows the deflection results on the recession and insulation surfaces. These results are normalized by the magnitude of the maximum deflection. In contrast to the strain profiles on the two surfaces, the vertical deflection on the surface of, and within, both layers are not sensitive to the disparate properties. The two curves closely overlap one another, yielding the expected homogeneity in the vertical deflection profiles. These results are not *directly* compared with experimental measurements due to a lack of confidence in the LVDT readings.

The LVDTs are mounted onto the four-point bend apparatus, which exhibits rig compliance. As the apparatus is loaded, it flexes, affecting the readings of the LVDTs.
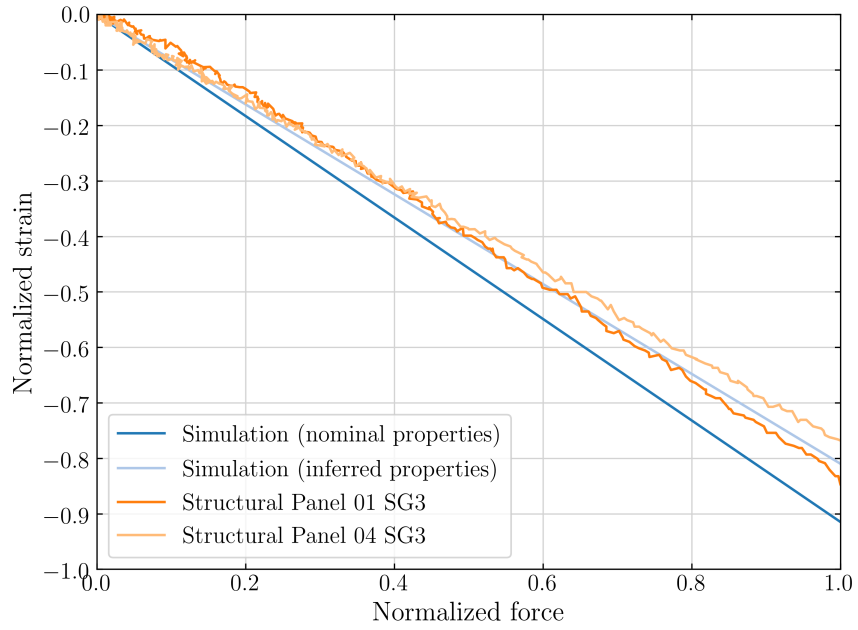
Figure 5.5: Comparisons of strain gauge measurements with predictions at SG3 location.
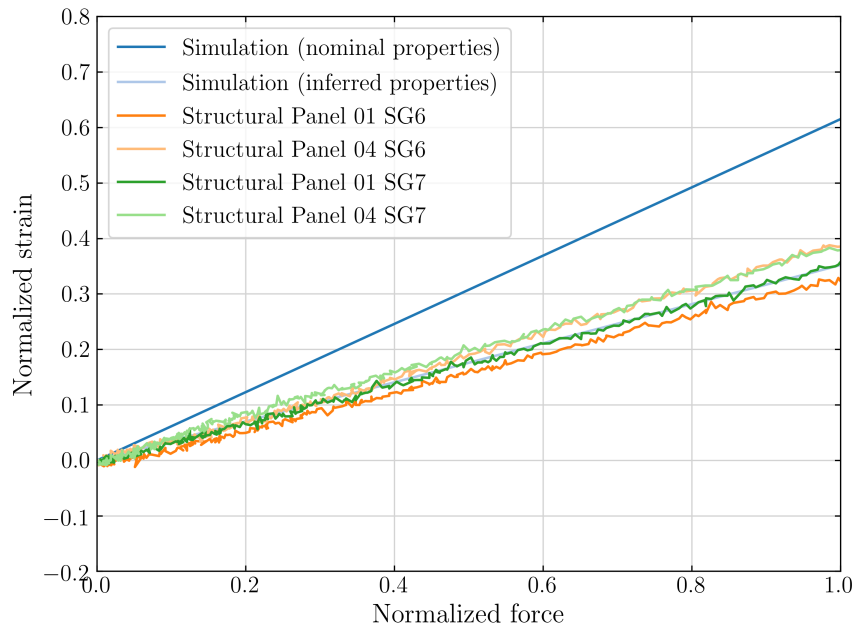
Figure 5.6: Comparisons of strain gauge measurements with predictions at SG6 and SG7 locations.
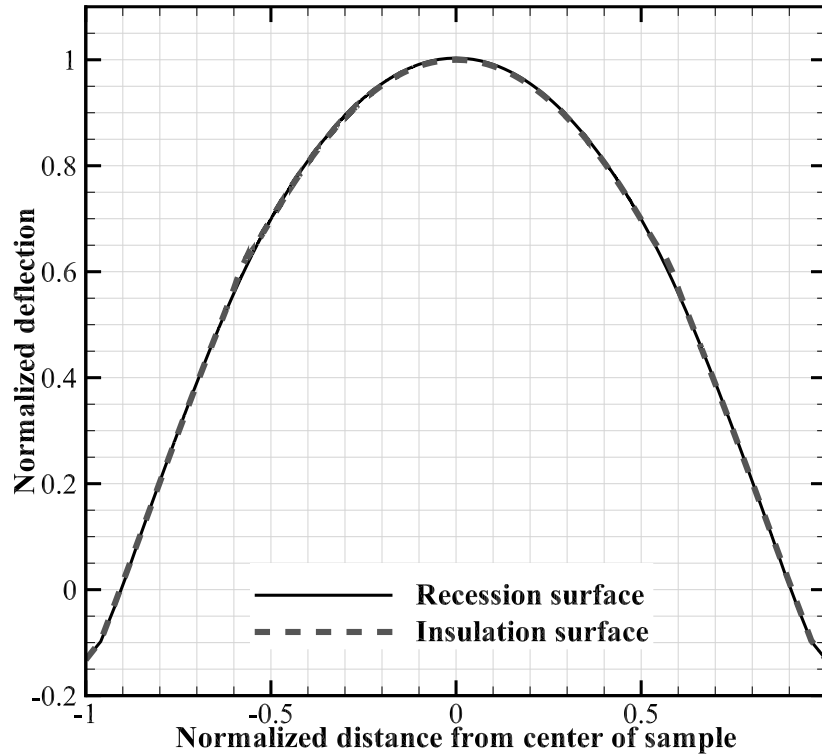
Figure 5.7: Normalized vertical deflection along the length of the sample.

However, the error induced by the rig is the same across all LVDTs. Taking the difference between two LVDT measurements removes the error component and enables a quantitative comparison between simulation results and experimental measurements.

Figure 5.8 presents the comparisons of normalized simulation results with experiments for $|LVDT3 - LVDT2|$ and $|LVDT3 - LVDT1|$. The displacements are normalized by the magnitude of the maximum deflection, and the force is normalized by the maximum force applied, which is five times the preload. From these comparisons, excellent agreement between the simulation and experimental results for Structural Panel 04 is observed. Interestingly, the Structural Panel 01 curve deviates from the Structural Panel 04 curve as the force is increased, further supporting the earlier hypothesis that non-uniformity in the warp direction's structural properties in the Structural Panel 01 panel, asymmetry in the panel geometrically, or asymmetry in the experimental setup may be present.

100

Table 5.5 presents the MSE of the simulation results and both experimental test cases (Structural Panels 04 and 01 are denoted as SP04 and SP01). Two separate MSEs are computed corresponding to the set of normalized forces less or equal to half (denoted as "≤0.5"), the set of normalized forces more than half (denoted as ">0.5"), and the entire sample space (denoted as "aggregate"). From the aggregate errors, it is evident that the simulation results are in closer agreement with the Structural Panel 04 panel by an order of magnitude. A partitioned analysis illustrates that for smaller mechanical loading, the agreement between Structural Panel 01 and Structural Panel 04 and simulation results is much closer than for larger mechanical loading (> 0.5). Nonlinear geometrical effects are not present because the material is relatively stiff, and the applied loading is very small. It is possible that uncertainties induced by experimental apparatus tolerance are more pronounced at larger mechanical loading, creating the increased disparity in the experimental results. However, this is not conclusive from a sample size of two panels, and further investigation with additional experimental runs is needed to validate the hypothesis.

Table 5.6 shows the results from a univariate linear regression analysis performed using least squares. The analysis seeks to find a linear model of the form:

$$|\Delta u| = m f_n + |\Delta u|_0 \tag{5.3}$$

where f_n is the normalized mechanical load and $|\Delta u|_0$ is the magnitude of the differential of the displacement absent of loading. Absent of thermal loading, the linear behavior between force and displacement is expected and observed for small deformations even for a multi-material stackup of orthotropic materials.

Table 5.4: MSE of LVDT measurements from Structural Panel 01 and 04 versus simulation results $[10^{-6}]$

Case	SP01 ($\leq$0.5)	SP04 ($\leq$0.5)	SP01 ($>$0.5)	SP04 ($>$0.5)
$|LVDT3 - LVDT1|$	7.41	5.28	207	6.52
$|LVDT3 - LVDT2|$	6.51	2.21	80.5	3.13

Table 5.5: MSE of LVDT measurements from Structural Panels 01 and 04 versus simulation results $[10^{-6}]$

Case	SP01 ($\leq$0.5)	SP04 ($\leq$0.5)	SP01 ($>$0.5)	SP04 ($>$0.5)
$|LVDT3 - LVDT1|$	7.41	5.28	207	6.52
$|LVDT3 - LVDT2|$	6.51	2.21	80.5	3.13

Table 5.6: Univariate regression estimators of displacement versus force

Case	m			$|\Delta u|_0$		
	SP01	SP04	Simulation	SP01	SP04	Simulation
—LVDT3 - LVDT1—	0.280	0.262	0.253	-0.008	-0.006	1.12E-10
—LVDT3 - LVDT2—	0.091	0.076	0.075	-0.004	-0.002	5.61E-9
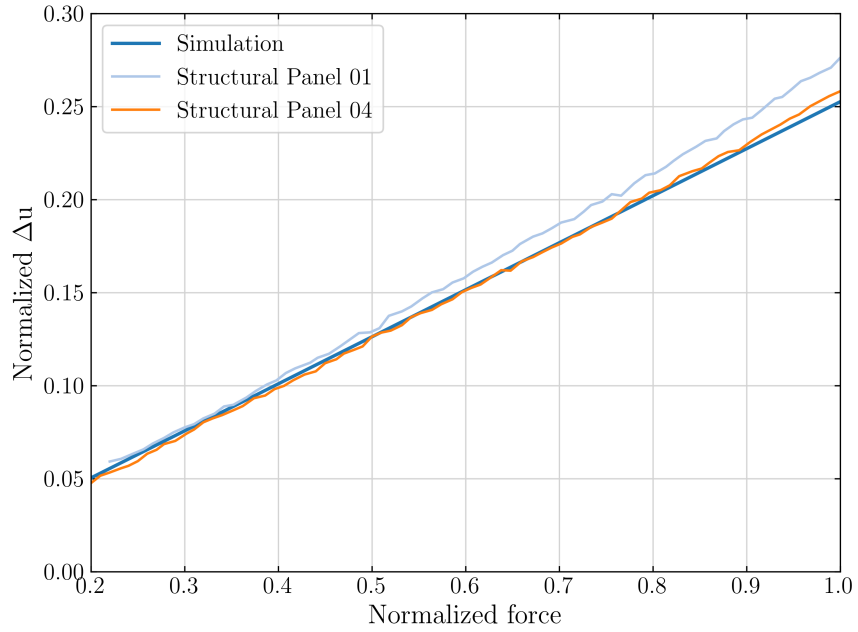
(a) |LVDT3 - LVDT1|
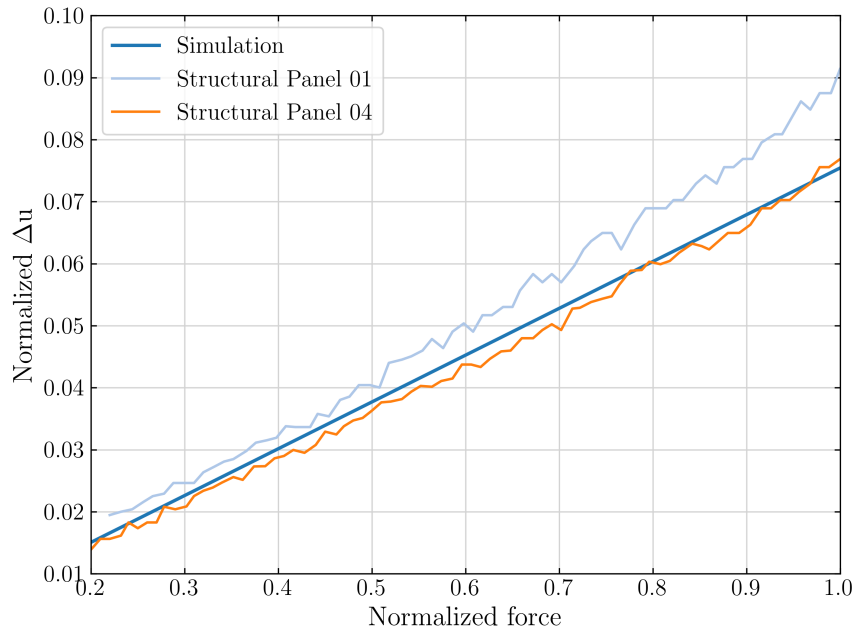
(b) |LVDT3 - LVDT2|

Figure 5.8: Comparisons of LVDT measurements with predictions

5.5   Chapter Summary

The structural response results presented here are the second of three chapters

focused on the analysis of HEEET in the LHMEL experiments. The initial studies

indicated that the previously determined properties from the 13 in. HEEET weave are not representative of the 24 in. HEEET weave used in Round 02 of the LHMEL experiments, which were expected to be stiffer as they were manufactured from a tighter weave. As such, a new set of room temperature stiffness properties was inferred, which will be later used for coupled thermo-structural modeling in the next chapter. The new set of room temperature stiffness properties were inferred using the SG measurements from the LHMEL testing. When using the inferred properties, excellent agreement between simulation results and measurements for strain and displacement measurements was observed.

The primary contribution of the analyses presented here is the inferred set of the stiffness properties for the 24 in. HEEET recession and insulation layer weaves at room temperature. These properties are essential for advancing modeling capability, as well as for future experimental testing and design efforts.

Progress towards structural response modeling of the 24 in. HEEET weave has been made; however, there remain important modeling considerations for future weaves, should the manufacturing process change. These considerations motivate further analysis, which can be performed at the microscopic level, to study different styles of weaves and to derive a macroscopic model.

CHAPTER VI

Coupled Thermo-Structural Response Modeling

The previous two chapters studied the structural and thermal response of the HEEET material in isolation. In this chapter, the inferred material properties from the preceding chapters are collectively used for coupled thermo-structural modeling.

In the LHMEL experimental tests of the HEEET, a key focus was on studying the combined thermo-structural behavior of the material. The same SG locations shown in Fig. 6.1 are used to measure the strain response as the material is heated. Surface level TCs were situated next to each SG to measure the temperature, which were later used to correct the raw readings of each SG if the SG does not remain at room temperature.

For the combined thermo-structural testing, in-depth TCs were not used, so the in-depth thermal response for these particular panels were not measured. However, the results from Chapter IV have shown that more confident predictions can be made when using the inferred thermal conductivity to model the internal thermal response.

6.1   Testing and Modeling description

Two different panels, referred to as Acreage 01 and Acreage 04, without a composite substrate were tested under combined mechanical and thermal loading. The testing conditions are shown in Table 6.1. Both panels were preloaded using the four-
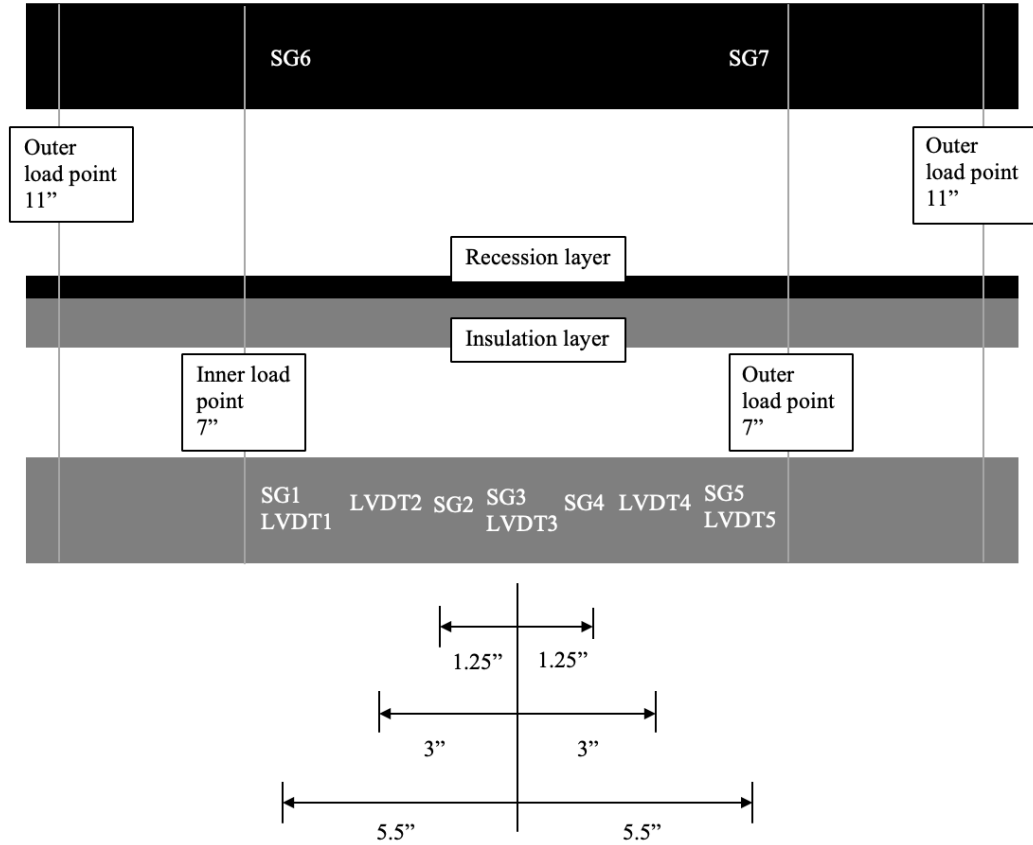
Figure 6.1: Experimental apparatus locations for LHMEL test of HEEET.

point-bending apparatus to approximately 445 N prior to turning on the laser at full power. After the laser is turned on, the Acreage 01 panel experienced a single load ramp from the four-point-bending apparatus, while the Acreage 04 panel experienced two load ramps.

Table 6.1: Testing conditions for thermo-structural panels

Panel name	Mechanical preload, N	No. of Load ramps	Power level
Acreage 01	445	1	Full
Acreage 04	445	2	Full

As the HEEET TPS is made from a pyrolyzing material, the decomposition of the phenolic resin and softening of the carbon substructure is expected to lead to a reduction in stiffness at elevated temperatures. The stiffness degradation is a key area of interest in the modeling of HEEET.

The coupled thermo-structural modeling is performed under a quasi-steady assumption. The suitability of the assumption is substantiated by the Biot number evaluating to $\mathcal{O}\left(10^3\right)$, which is much greater than unity. Physically, a large Biot number indicates that the characteristic time scale of the thermal response is much greater than that of the mechanical time scale of the structural response, providing the necessary condition for a quasi-steady coupling approach to be sufficient.

The inferred thermal conductivity as a function of temperature, inferred room temperature structural properties, and spatial radiative heat flux boundary condition profile determined from the analyses in the previous two chapters are used for the coupled modeling.

6.2 Thermal response results

The thermal response results for panels under the combined mechanical and thermal loading are presented here. The coupling is only in the thermal to structural direction and not in the reverse, as the thermal results here are unaffected by the presence of mechanical loading. However, the results here are different from the full power results in Chapter IV as the radiative heat flux boundary condition uses a single linear ramp to full power, similar to the half power profile in Chapter IV, as opposed to the multi-ramp technique used for the pure thermal HEEET testing.

The normalized density contours at the end of the heating phase is shown in Fig. 6.2. Here, the density is normalized by the recession layer material's density in its virgin state, the maximum density observed in the entire HEEET material. The majority of the changes in density occurs within the vicinity of the centerline.

The normalized temporal density profiles are shown in Figs. 6.3 and 6.4 for several depths in the recession and insulation layers, respectively, along the centerline. The virgin and char densities are also included as a reference.

The monotonicity in the temporal profiles is intuitive from a mathematical per-

spective as the decomposition of each phenolic resin component is modeled using an Arrhenius relationship. It is also physically intuitive because the rate of phenolic resin decomposition is directly proportional to temperature until the phenolic resin is completely decomposed. The "completely decomposed" state is commonly known as the "fully charred" state in the ablation community.

As shown, the majority of the recession layer material reaches within a few percent of the char density during the 255 s duration of the applied heating. Therefore, the recession layer is predicted to be effectively fully charred by the time the laser is turned off. The pyrolysis gases produced from the decomposition flow through the pores of the material and exit out of the recession surface. This is inherently a long process, but especially so for HEEET due to its low permeability, so it is expected that much of the pyrolysis gas products from the decomposition are still in the recession layer when the laser is shut off.

In an actual flight setting, these pyrolysis gases would transfer some of the internal energy of the material into the boundary layer, as well as deflect some of the incoming hot boundary layer gases away from the material, resulting in multiple mechanisms of desired cooling. However, because the LHMEL experiment is conducted in a chemically inert environment using a nitrogen gas purge, the cooling effect is not an area of interest in the coupled thermo-structural modeling.

For the insulation layer, which is of lower density, it takes significantly longer to reach the char density across all depths. Significant decomposition, such as in the normalized density response at the 0.6 in. and 0.8 in. depth locations, is still observed after the laser is shut off at 255 s as heat is conducted from the hotter recession layer to the cooler insulation layer. The majority of the insulation layer at the centerline does not experience a temperature change nor decomposition before the laser is turned off. From a stiffness degradation modeling perspective, the emphasis is therefore on the recession layer.

For both figures, a humplike feature is observed in each density profile. This is due to additional decomposition reactions activating at higher temperatures, that explains why the hump occurs at later times deeper into the material.
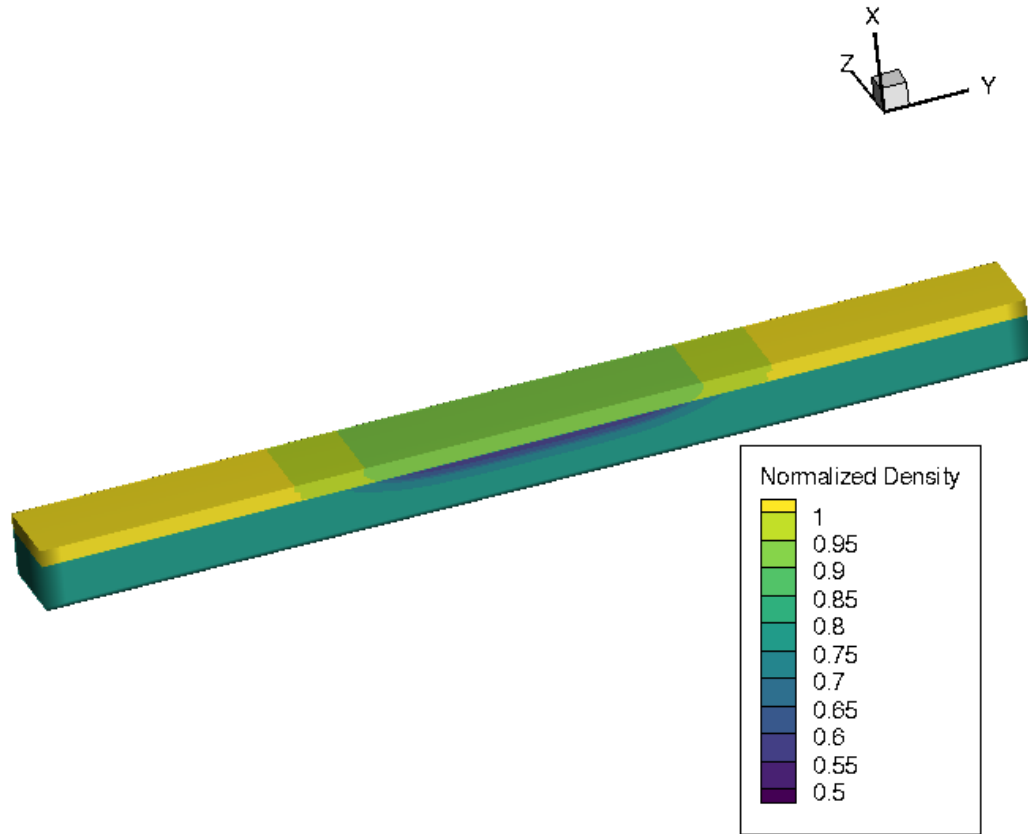
Figure 6.2: Normalized density contours at the end of the heating phase.

The corresponding virgin mass fraction profiles are shown in Figs. 6.5 and 6.6. The trends here mimic those of the density profiles as the temporal solid density is a linear combination of the virgin and char densities. However, these figures are more illustrative of the actual amount of virgin material remaining.

From Fig. 6.5, it is clear that the entire recession layer is approximately fully charred at the end of the heating phase, with the 0.4 in. location (the interface between the insulation and recession layer) falling to about a virgin mass fraction of 0.04. Significant stiffness degradation is expected for the recession layer within the
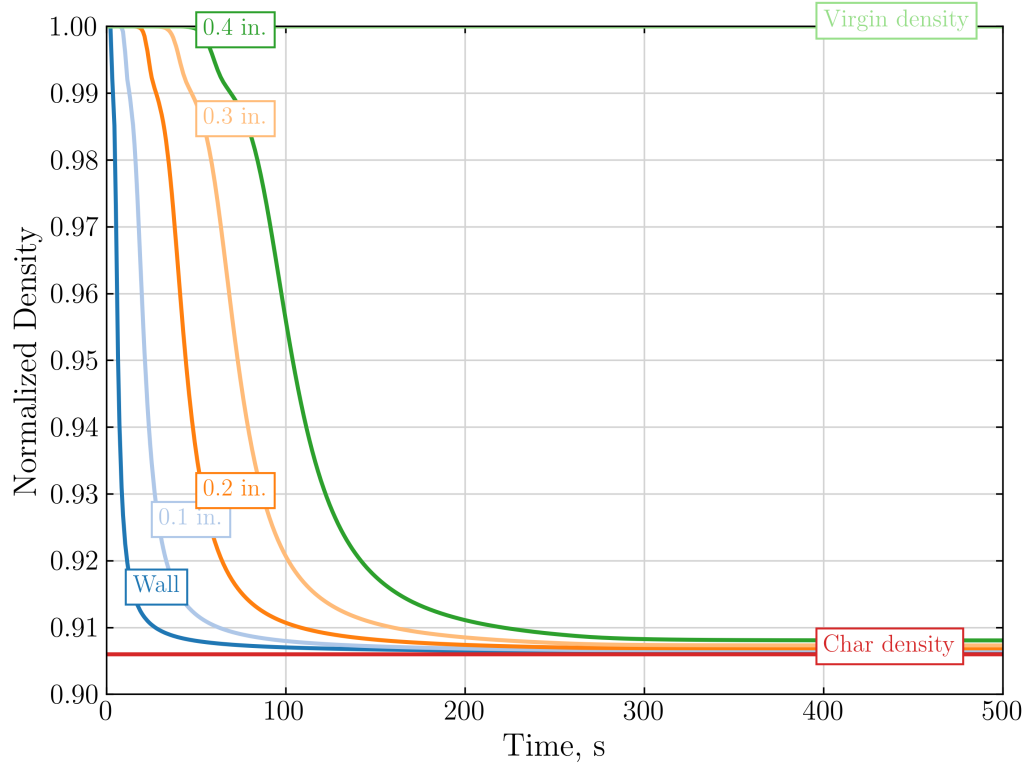
Figure 6.3: Recession layer density profiles along centerline of HEEET panel.

vicinity of the centerline.

In Fig. 6.6, it is clear that limited charring is observed. The 0.6 in. location asymptotically approaches a virgin mass fraction of 0.1, while locations 1 in. and deeper exhibit an under 10% change in virgin mass fraction for the first 500 s of testing. As alluded to previously from studying the density plots, the decomposition continues to occur after the laser is turned off due to the heat transfer from the hotter recession layer to the cooler insulation layer, but the effects are clearly limited for the majority of the insulation layer.

The extent of reaction plots are shown in Figs. 6.7 and 6.8. The trends here are inversely related to the trends in the virgin mass fraction curves. Mathematically, the result is intuitive as the virgin mass fraction can be written as the extent of reaction
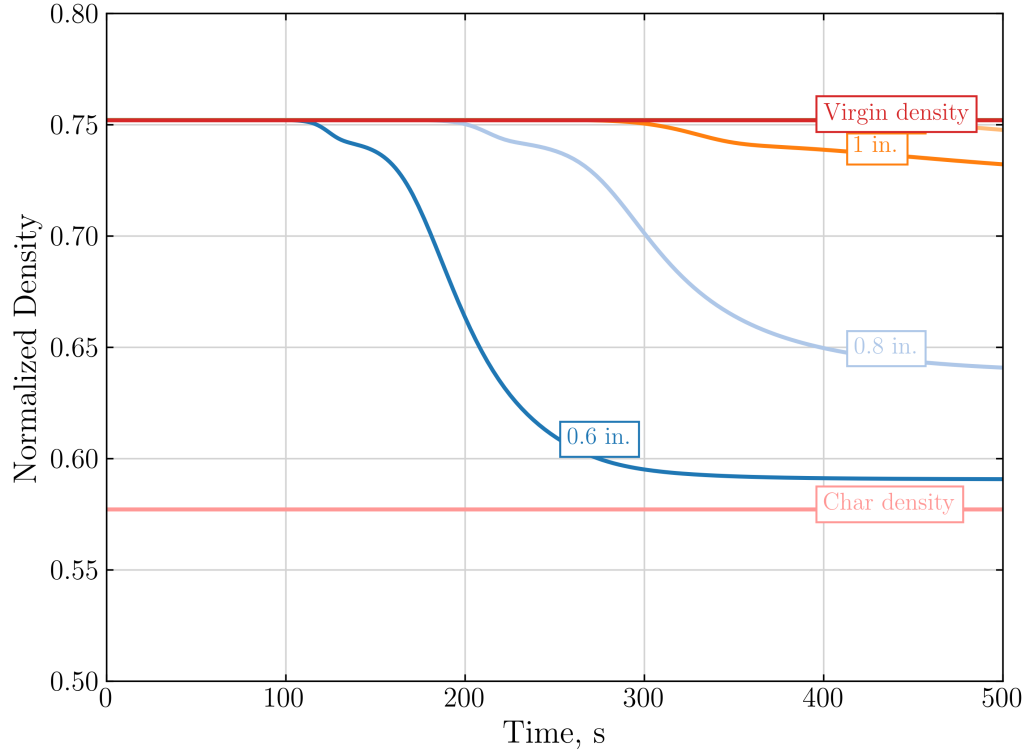
Figure 6.4: Insulation layer density profiles along centerline of HEEET panel.

scaled by a negative constant with an offset term:

$$Y_v = \left(\frac{\rho_v}{\rho_s}\right)(1-\beta) \tag{6.1}$$

6.3   Structural response results

The HEEET material has orthotropic material properties, which implies that the expansion or contraction due to thermal loading will be different along the three orthogonal directions. Interestingly, the HEEET recession layer material exhibits a negative CTE component in the Warp direction, which indicates that the material will contract in the Warp direction when it is heated. The Weft and TTT directions of the recession layer have a positive CTE component and experience expansion when heated.
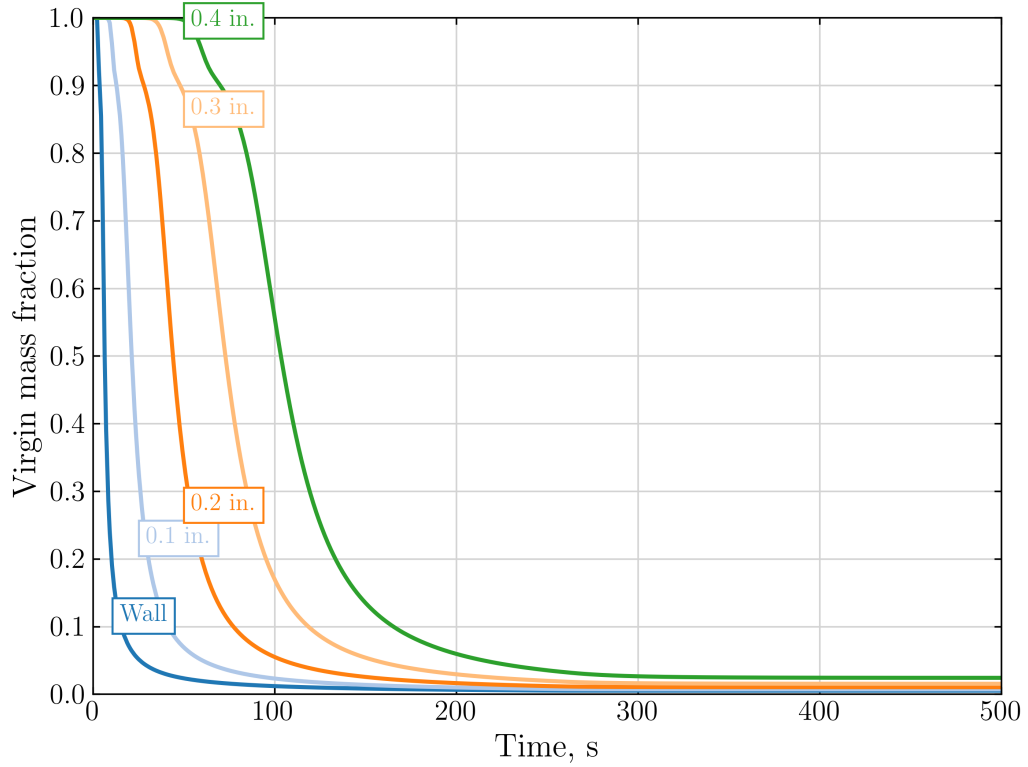
Figure 6.5: Recession layer virgin mass fraction profiles along centerline of HEEET panel.

For reference, the normalized recession CTE components are shown in Table 6.2. The normalization factor is the maximum of the magnitude of the three CTE components. The TTT component will exhibit the largest deformation due to thermal loading, followed by the Warp and Weft directions.

Table 6.2: Normalized CTE for recession layer material .

Direction	Normalized CTE
Warp	-0.113
Weft	0.083
TTT	1.0

For the insulation layer material, all three CTE components are positive, indicating the insulation layer will expand in all three directions when it is heated. Table 6.3 shows the normalized insulation layer material CTE components. For comparative purposes, the normalization factor used here is the same as that of the recession layer.
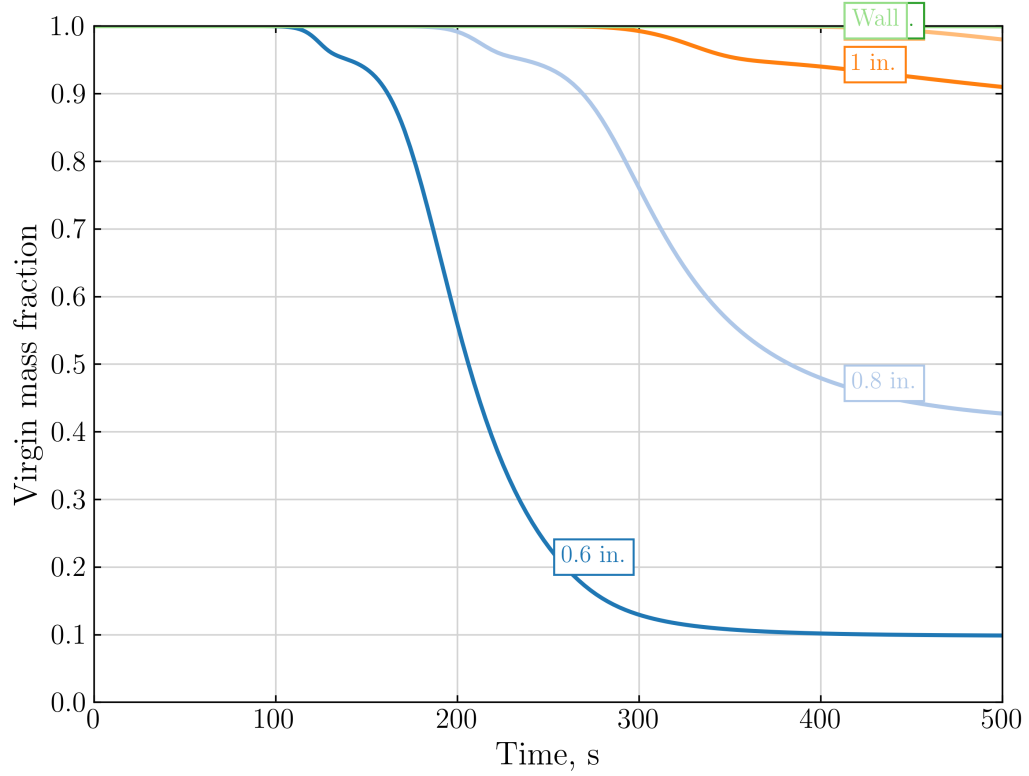
Figure 6.6: Insulation layer virgin mass fraction profiles along centerline of HEEET panel.

Like the recession layer material, the insulation layer material's TTT direction will also exhibit the largest deformation due to thermal loading. However, the Weft direction will exhibit a larger deformation than that of the Warp direction, the opposite of what is observed in the recession layer.

Table 6.3: Normalized CTE for insulation layer material

Direction	Normalized CTE
Warp	0.019
Weft	0.162
TTT	0.893

Figure 6.9 presents the normalized temperature contours at four times. The temperatures are again normalized by the radiative equilibrium temperature. The heating is well contained in the in-plane direction during the duration of testing. Since the thermal strain is effectively a scaled version of temperature, the contours for ther-
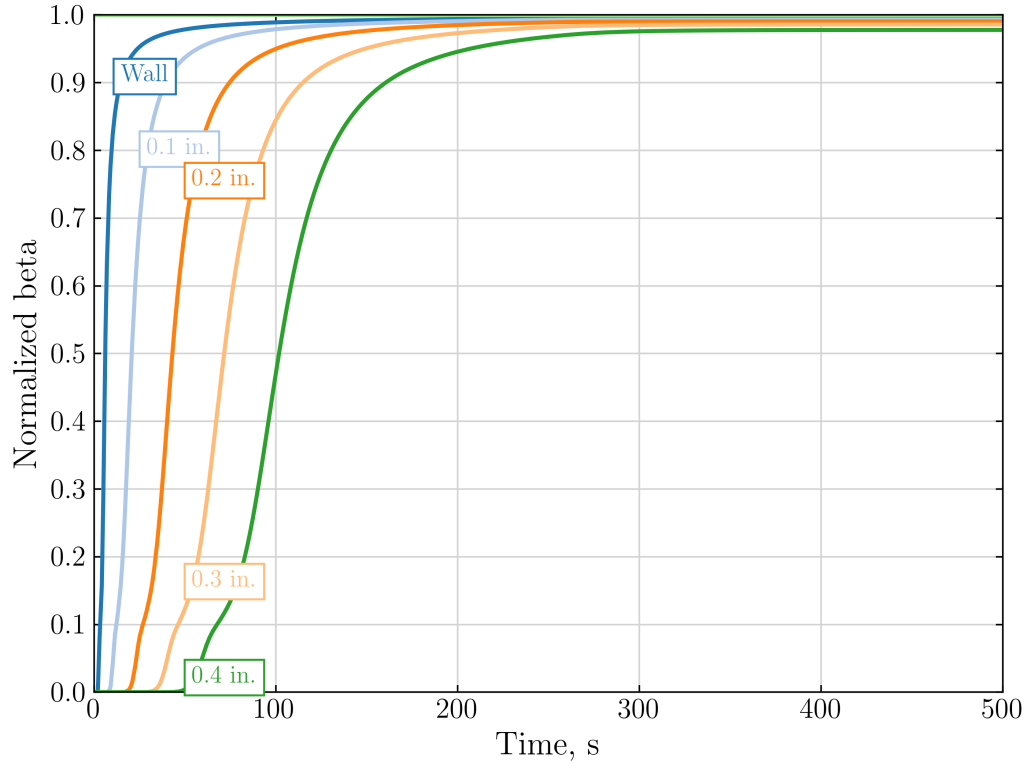
Figure 6.7: Recession layer extent of reaction along centerline of HEEET panel.

mal strain will be analogous and not presented here. These contours provide a more complete picture of what is occurring in the material as a whole, and how the thermal loading, which is concentrated within a small region of the overall material, may impact the deformation of the overall material.

The recession layer has a larger TTT CTE and because the experiment is set up to fully char the recession layer material, most of the deformation due to thermal expansion in the overall dual layer system is expected to originate from the centerline region of the recession layer. The effects on the structural response will propagate into the rest of the material instantly due to the relatively small mechanical time scale.
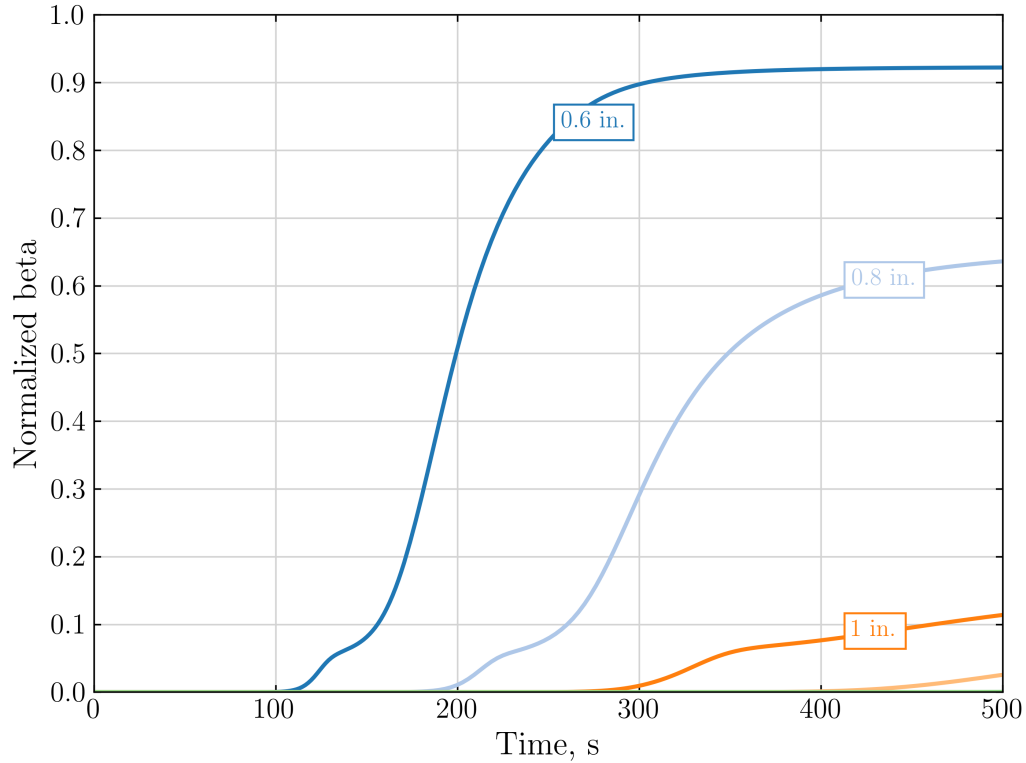
Figure 6.8: Insulation layer extent of reaction along centerline of HEEET panel.

6.3.1 Results under constant stiffness assumption

Initial quasi-steady simulations are performed under the assumption that the stiffness does not change with temperature as a baseline metric for the stiffness reduction analysis in the subsequent section.

Due to the uncertainties in the measurements and predictions of temperature during the cooling phase of the testing, the focus is on comparisons during the heating phase. From the thermal analyses in Chapter IV, it is also clear that discrepancies between simulation results and measurements still exist for the deeper and off-center locations when using inferred thermal conductivities and spatial radiative heat flux boundary condition. These discrepancies are not significant enough to substantially affect the stiffness reduction analyses here, especially given that the majority of the thermal loading is concentrated in the region where there is a high degree of confidence in the thermal response simulation results.

115
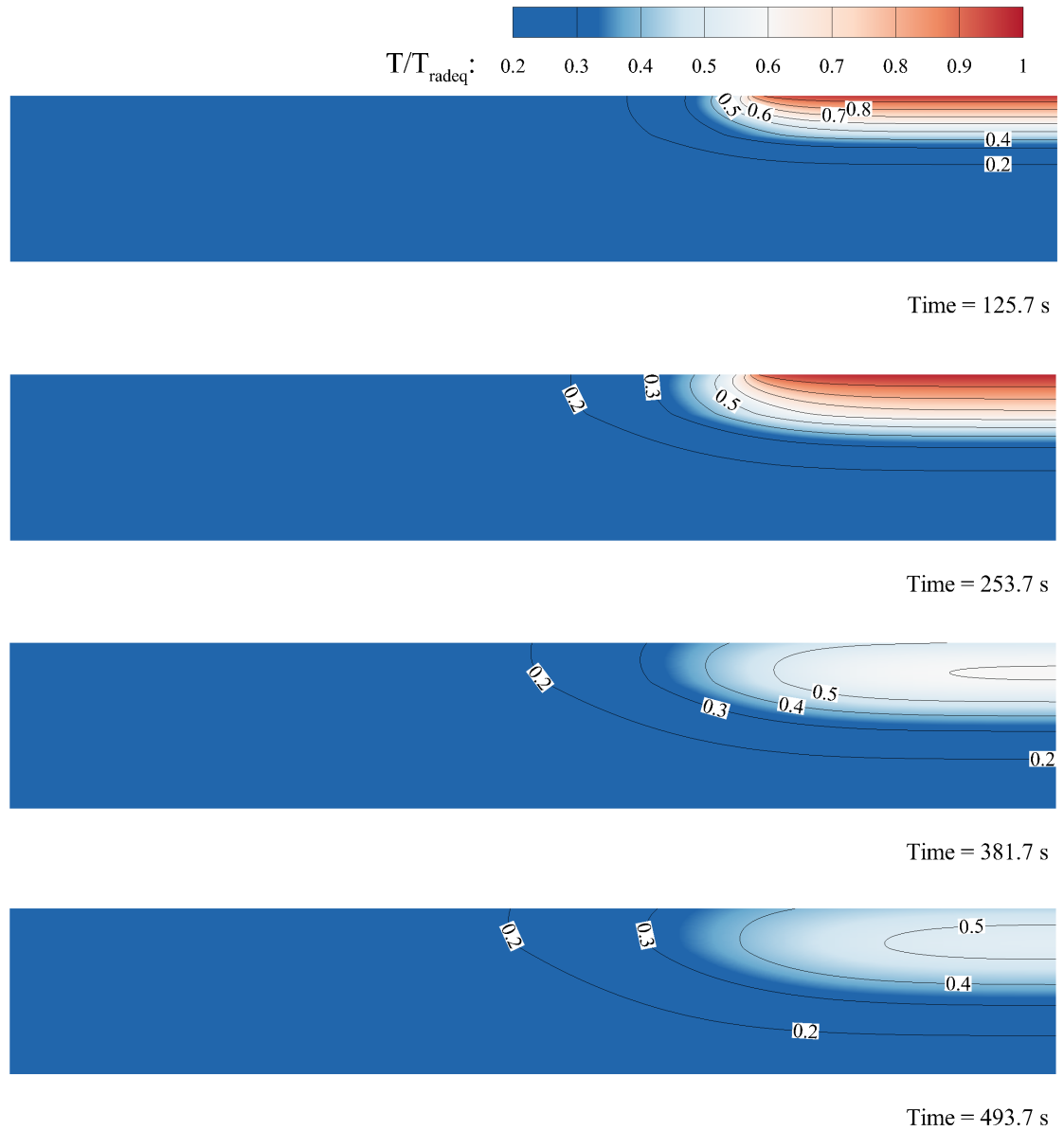
Figure 6.9: Normalized temperature contours using a quarter geometry.

Figures 6.10-6.12 present the comparisons between SG measurements and simulation predictions under a constant stiffness assumption. The results here are for Acreage 01, where a constant load ramp is applied at approximately 28 s for 10 s. In the experiment, this ramp is achieved by applying a constant displacement rate to the actuator and inner load points. In the simulation, a temporal displacement boundary condition is applied.

SG2 and SG4 did not register readings for both Acreage 01 and Acreage 04 panels. Therefore, the comparisons are performed exclusively for the SG3, SG1 and SG5, and SG6 and SG7 locations shown in Fig. 6.1, where the latter two groupings are symmetrically distributed along the Warp direction. All strain results are normalized by the maximum magnitude of the strain observed in either the simulation results or measurements.

While symmetrically distributed, notable differences in the SG1 and SG5, SG6 and SG7 measurements are observed. There are several possible causes for the discrepancy, namely,

- asymmetry in the experimental setup,

- tolerance and uncertainties in the SGs devices,

- HEEET weave asymmetry due to manufacturing process and weaving material,

all of which could contribute to the asymmetry in the measurements. However, for SG1 and SG5 in particular, there appears to be a consistent and approximately constant offset in the results after 38 s. It is unclear what the source of the discrepancy is attributed to, but it is unlikely that (noisy) uncertainties in the SGs instruments could produce a homogeneous discrepancy of this kind.

For the HEEET panels under purely thermal conditions, IR camera data showed asymmetry in the surface heating profiles, so it is possible that the HEEET panels under combined mechanical and thermal loading also experienced the asymmetry in the surface heating profile. In the HEEET panels under purely mechanical conditions, asymmetry was also observed in the SG measurements at room temperature, indicating that there is asymmetry in the four-point-bending apparatus. It is likely that a significant portion of the discrepancy in the readings between the symmetrically placed SGs originated from these two asymmetries associated with the experimental setup.

117

In both the measurements and simulation results, the recession and insulation surfaces are shown to remain in compression and tension for the entire duration. Initially, at zero time, the HEEET panel is in its preloaded state from the four-point-bending mechanism. Unsurprisingly, in its initial state, the simulation results and measurements are identical when using the inferred room temperature stiffness properties.

As time progresses, the continuous radiative heating transferred to the material propagates multi-dimensionally in the Warp, Weft, and TTT directions, increasing the temperature and thus thermal strain. A large internal thermal stress field, proportional to the temperature shown in Fig. 6.9, results in structural deformation in the rest of the material.

The tensile thermal stresses are generated along the TTT and Weft directions, and compressive thermal stresses are generated along the Warp direction, all of which are occurring only within the vicinity of the centerline region of the recession layer material. For the insulation layer material, tensile thermal stresses are expected in all directions in the centerline region, but, comparatively, these stresses are much smaller due to the lack of temperature change and significantly smaller stiffness in the insulation layer material.

For the SG1 and SG5 locations, the simulation results show that the strain increases monotonically from approximately -0.15 to -0.1 prior to the load ramp. For the same timeframe, the measurements indicate that the response is approximately constant. After the load ramp, the simulation results indicate a gradual, approximately monotonic, increase in strain from approximately -0.63 at 38 s to -0.59 at 250 s. The experimental results exhibit less monotonicity, but also a net increase in strain from approximately -0.75 and -0.81 to -0.68 and -0.82, respectively.

For the SG3 location, which is at the centerline of the insulation layer surface, a similar increase in strain from -0.15 to -0.1 is observed in the simulation results.

The experimental response here indicates a net decrease in strain from -0.15 to -0.19. After the load ramp, the simulation results show a gradual, approximately monotonic, decrease in strain from -0.84 to -0.9 at 250 s, while the experiment exhibited a concave bowlike response.

For the locations on the recession layer surface, a monotonic increase in the strain is observed in the pre-ramp phase from approximately 0.7 to 0.13, while the measurements indicate the strain response is approximately constant. After the ramp, a convex bowlike shape is observed in the measurements, while the simulation results show a gradual, approximately monotonic, decrease in strain from 0.36 to 0.28.

Comparisons between the simulation results and experimental measurements generally show that the simulation predicts the recession and insulation surfaces to exhibit larger compression and tension, respectively, than that observed in the measurements. This is intuitive as thermal stresses, under a constant stiffness assumption, are amplified in the simulations, whereas, in the experimental environment, stiffness degradation is likely occurring, mitigating the thermal contribution to the total strain.

Another observation in support of the presence of stiffness degradation is the slope of the curves during the load ramp phase. During this time, the inner load points are further displaced into the insulation layer at a constant displacement rate to achieve a larger mechanical load using the four-point-bending apparatus. The slope of the simulation predictions in all three figures during the load ramp are smaller than that indicated by the measurements, suggesting that stiffness degradation has occurred prior to and during the load ramp as the magnitude of the slope during the load ramp is inversely proportional to the stiffness. The inverse proportionality comes from the fact that a constant displacement rate is applied, which increases the load linearly with respect to time. When comparing a material with and without stiffness degradation, the material without any degradation is expected to better withstand the additional loading, resulting in a smaller change in deformation, which is clearly

observed at all measurement locations.

Another observation for the strain response at the SG1/SG5 (off-center) and SG3 (centerline) locations is that the temporal evolution of the measurements and predictions are almost identical for the simulation results before the load ramp, but are different for the measurements at the two locations. A much larger discrepancy is observed between the off-center and centerline SG measurements after 30 s when compared to the simulation predictions. It is posited that this is attributed to stiffness degradation and the effects of thermal strain, which, additively, are expected to contribute to differences in off-center and centerline SG measurements on the insulation surface.

Another interesting observation is that the pre-ramp and after-ramp phases are generally monotonic in the predictions, whereas the experimental measurements indicate a horizontal bow-like shape in the SG3, SG6, and SG7 locations. It is unclear if this is due to stiffness reduction, experimental uncertainties, or unmodeled physics. A more in-depth discussion will follow in the next subsection.

The key takeaway here is that the results indicate stiffness degradation is occurring when the material is heated. In particular, as the temperature contours in Fig. 6.9 indicate, the majority of the degradation is located in the recession layer and within the vicinity of the centerline. Mild degradation is expected in the insulation layer nearby the interface between the two layers. The next subsection is focused on presenting the stiffness degradation studies.

6.3.2 Stiffness degradation studies

The studies in the preceding section indicate that stiffness degradation is occurring within the material and hypothesized to be primarily in the recession layer material. This section explores the phenomenon using a similar constrained optimization strategy that was introduced in Chapter IV, and compares the inferred stiffness reduction
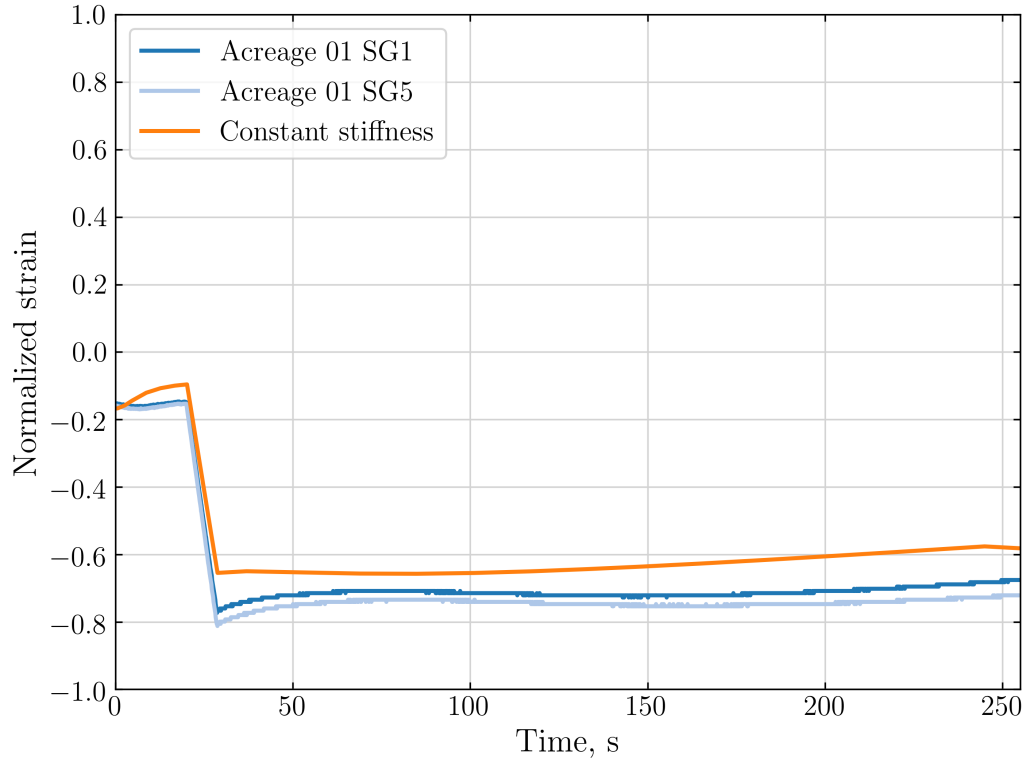
Figure 6.10: Comparison of SG1 and SG5 measurements with predictions.

factors to Carbon Cloth Phenolic (CCP).

The PSO algorithm for inferring stiffness degradation factors is shown in Algorithm 23. Lines 1 through 8 are the initialization procedure of the algorithm. Lines 1 and 2 initialize the particle's current and best known positions randomly using a uniform distribution, where lo and hi represent the minimum and maximum stiffness reduction factors, which are set to 0.1 and 1.0, respectively. Position here is the stiffness reduction factor at 100 K temperature intervals from the minimum and maximum temperatures observed in the thermal response. Lines 4 through 6 assess whether the current particle's best known position yields a smaller objective, $f(\cdot)$, than the swarm's current best position, $\boldsymbol{g}$. If it does, the swarm's best solution, $\boldsymbol{g}$, is updated.
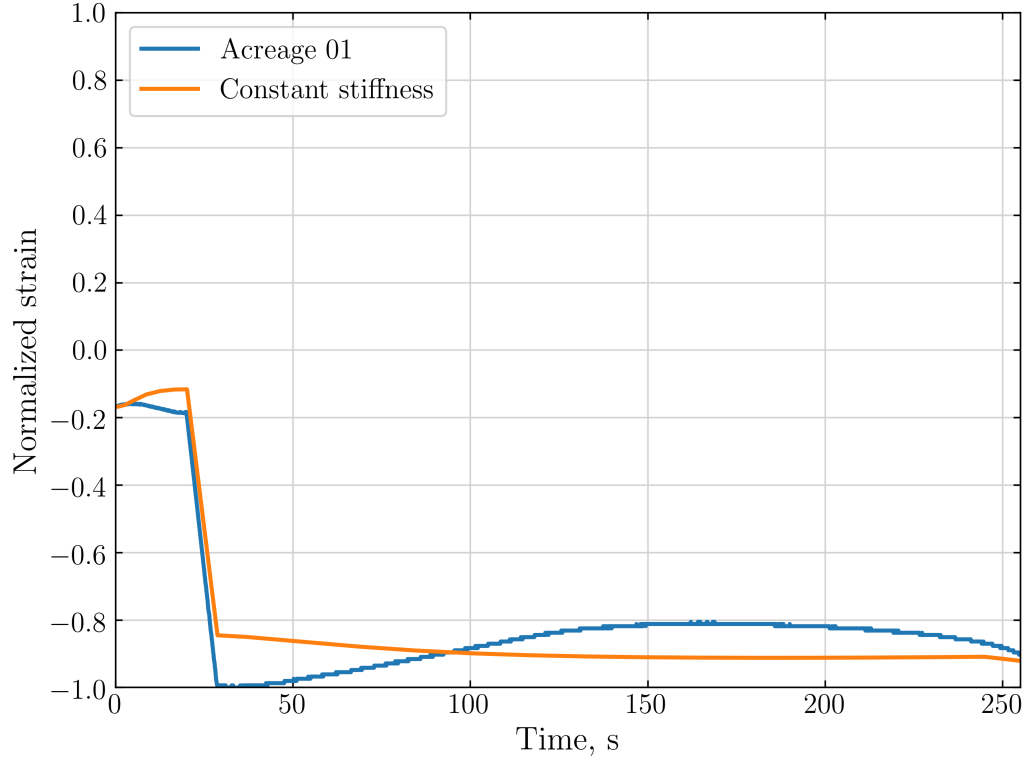
Figure 6.11: Comparison of SG3 measurements with predictions.

The function $f(\cdot) : \mathbb{R}^{|T|} \to \mathbb{R}$ is the objective function, defined as,

$$\arg\min f\left(\boldsymbol{g}\right) \tag{6.2}$$

$$\text{s.t. } 0.1 \leq g_i \leq 1.0 \quad \forall i = 1, \ldots, |T| \tag{6.3}$$

$$f(\boldsymbol{g}) = \|S_e - S_p(\boldsymbol{g})\|^2 \tag{6.4}$$

where $\boldsymbol{S}_e$ and $\boldsymbol{S}_p(\boldsymbol{g})$ are the temporal experimental and simulation response of SG1, SG3, SG5, SG6, and SG7. The variable $|T|$ represents the number of temperature segments, or the number of stiffness reduction factors being inferred. Evaluating the objective function is computationally expensive as it involves executing the thermo-structural solver.

Line 7 of the algorithm initializes the particle's velocity, $\boldsymbol{v}_i$, according to a uniform distribution. The particle's velocity governs the direction and magnitude in the multi-

122
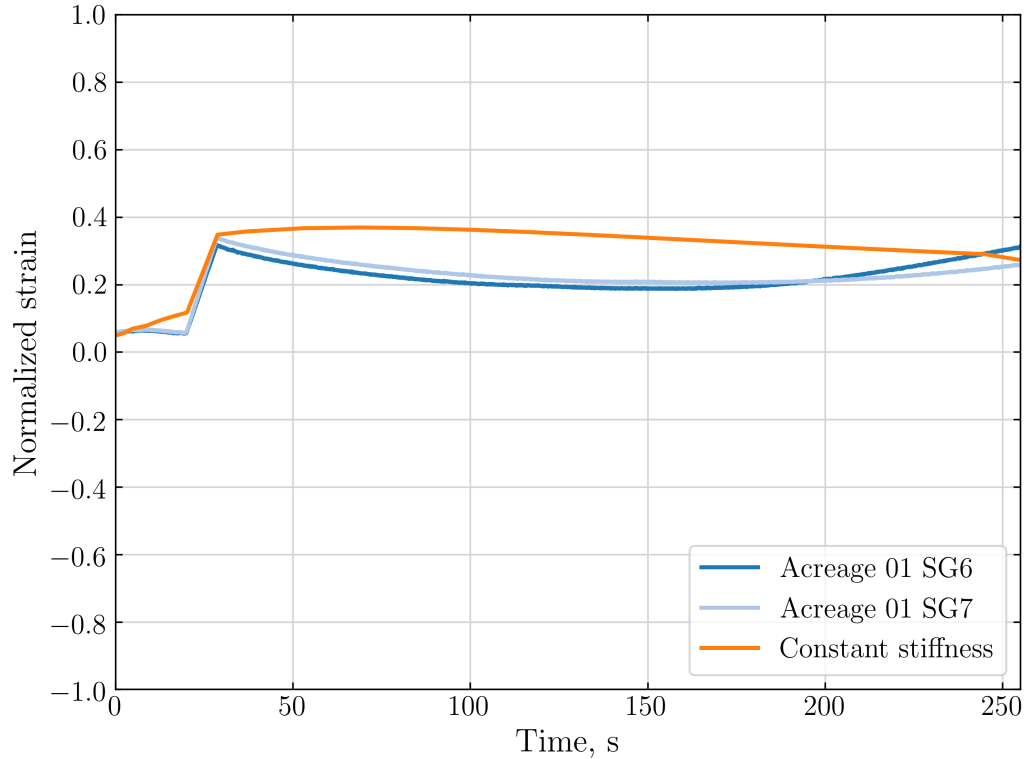
Figure 6.12: Comparison of SG6 and SG7 measurements with predictions.

dimensional search space.

Lines 9 through 23 are the essence of the PSO algorithm. The criterion of the while loop assesses whether the relative decrease in the objective function between each iteration exceeds some user-defined threshold, ϵ. If it does, then the algorithm proceeds to the next iteration. If it does not, it may terminate if the previous n iterations also did not exceed ϵ, otherwise it proceeds to the next iteration. The variable n is user-defined and chosen to be five. Higher values of n did not appear to change the trajectory of the optimization algorithm.

Inside the while loop, there are two nested loops over all particles in the swarm and the number of temperature segments. The velocity is updated on line 13 after random sampling r_p, r_s from a uniform distribution bounded by zero and unity. Parameter ω, ϕ_i, ϕ_s are chosen by the user. On line 15, the particle's current position is updated based on $0 < \alpha \leq 1$, the learning rate. Lines 16 through 21 update the particle's and

swarm's current best positions, if necessary.

Initial studies indicate that the high dimensionality of the problem poses convergence challenges. In particular, it is very difficult to achieve appreciable convergence when considering the data after the load ramp (i.e., after approximately 38 s). Based on discussions with HEEET experimentalists, it is hypothesized that the bowlike shape of the strain response after 38 s is partly due to changes in CTE as a function of temperature and not due to stiffness reduction, and the response prior to 38 s is dominated by the mechanical loading and stiffness degradation. Hence, to infer stiffness degradation, the response prior to 38 s is given the most emphasis. The complexity of the problem is reduced substantially under this reasonable assumption. The size of the dataset used for inference is $\sim \mathcal{O}\left(10^3\right)$, and the number of dimensions is $\sim \mathcal{O}\left(10^1\right)$.

An additional complexity in solving the optimization problem to infer the stiffness degradation of the material is uncertainty in the convexity of the objective function. Similar to inferring thermal conductivity in the previous chapter, it is again possible that a converged solution may be locally optimal, but not globally optimal. To mitigate this concern, the algorithm is executed multiple times with different randomization of the initial positions to observe whether identical solutions are achieved. The multiple executions result in the same stiffness reduction factors; however, if different converged solutions are obtained, the solution that results in the smaller objection would have been taken as the global solution.

To avoid overfitting during the inference procedure, the SG3 results are disregarded for inference purposes. Only the results at the SG1/SG5 and SG6/SG7 are used. In particular, because these SGs are symmetrically distributed yet with notable discrepancy in measured values, they are averaged for the purposes of performing inference.

```
 1  for each particle i ∈ swarm do
 2  │    Initialize particle's position $\boldsymbol{p}_i \sim U(lo, hi)$
 3  │    Initialize particle's best known position $\boldsymbol{b}_i$ to $\boldsymbol{p}_i$
 4  │    if $f(\boldsymbol{b}_i) < f(\boldsymbol{g})$ then
 5  │    │    $\boldsymbol{g} \leftarrow \boldsymbol{b}_i$
 6  │    end
 7  │    Initialize particle's velocity $\boldsymbol{v}_i \sim U\left(-\left|hi - lo\right|, \left|hi - lo\right|\right)$
 8  end
 9  while criterion is not met do
10  │    for each particle i ∈ swarm do
11  │    │    for each dimension d ∈ T swarm do
12  │    │    │    Random sample $r_p, r_s \sim U(0, 1)$
13  │    │    │    Update particle's velocity
       │    │    │        $\boldsymbol{v}_{i,d} \leftarrow \omega\boldsymbol{v}_{i,d} + \phi_i r_p \left(\boldsymbol{b}_i - \boldsymbol{p}_i\right) + \phi_s r_s \left(\boldsymbol{g} - \boldsymbol{p}_i\right)$
14  │    │    end
15  │    │    Update particle's position $\boldsymbol{p}_i \leftarrow \boldsymbol{p}_i + \alpha\boldsymbol{v}_i$
16  │    │    if $f(\boldsymbol{p}_i) < f(\boldsymbol{b}_i)$ then
17  │    │    │    $\boldsymbol{b}_i \leftarrow \boldsymbol{p}_i$
18  │    │    │    if $f(\boldsymbol{b}_i) < f(\boldsymbol{g})$ then
19  │    │    │    │    $\boldsymbol{g} \leftarrow \boldsymbol{b}_i$
20  │    │    │    end
21  │    │    end
22  │    end
23  end
```

The inferred stiffness reduction factors are plotted and compared against CCP in Fig. 6.13. In previous studies at NASA, CCP was hypothesized to be a baseline metric for evaluating the inferred stiffness reduction factors. Both materials are primarily composed of carbon and phenolic, with both having a similar quantity of carbon, so there is a notable similarity in the substructure. However, there are also numerous differences. First, the amount of phenolic resin infused in each material is substantially different. Another major difference is that HEEET is an orthotropic material composed of a 3-D weave, whereas CCP is composed of a plain weave. So while fundamentally similar in the carbon composition, there are notable differences that will substantially affect the properties of the two materials.

The CCP factors are defined at six different temperatures. As shown, CCP reaches

its minimum stiffness reduction factor of 0.4 at a normalized temperature of 0.28.

Comparatively, the inferred stiffness reduction factors for HEEET decrease monotonically with temperature, whereas an increase in stiffness is observed for CCP when char temperatures are reached. The monotonicity in the inferred HEEET stiffness reduction factors beyond char temperatures is not a surprising result as the carbon substrate continues to soften. It is suspected that the difference in behavior in CCP and HEEET is due to the weave architecture, amount of phenolic resin infusion, and the dual layer components.

For HEEET, the majority of the stiffness degradation is observed to occur between the normalized temperature range of 0.15 to 0.6. The majority of the phenolic resin decomposition is occurring in this temperature range, where it is therefore intuitive for most of the degradation to occur.

Beyond a normalized temperature of 0.8, it appears that the stiffness reduction factor begins to stabilize, possibly reaching a minimum factor asymptotically. However, there is no experimental data to confidently infer the reduction factor beyond a normalized temperature of 1.0, and therefore this statement is currently only conjecture.

6.3.3   Structural response results using inferred stiffness

Figures 6.14-6.16 compare the experimental measurements to the simulation results using the inferred stiffness reduction factors. For each of the SG locations, the slope of the normalized strain response using the inferred stiffness is in much closer agreement with the experimental response. In particular, the slope is visibly steeper, as the HEEET material is more susceptible to deform when it is degraded. The predictions in the pre-ramp phase are also in much closer agreement with the experimental response.

For SG1 and SG5 locations in the pre-ramp phase, the normalized strain response

126
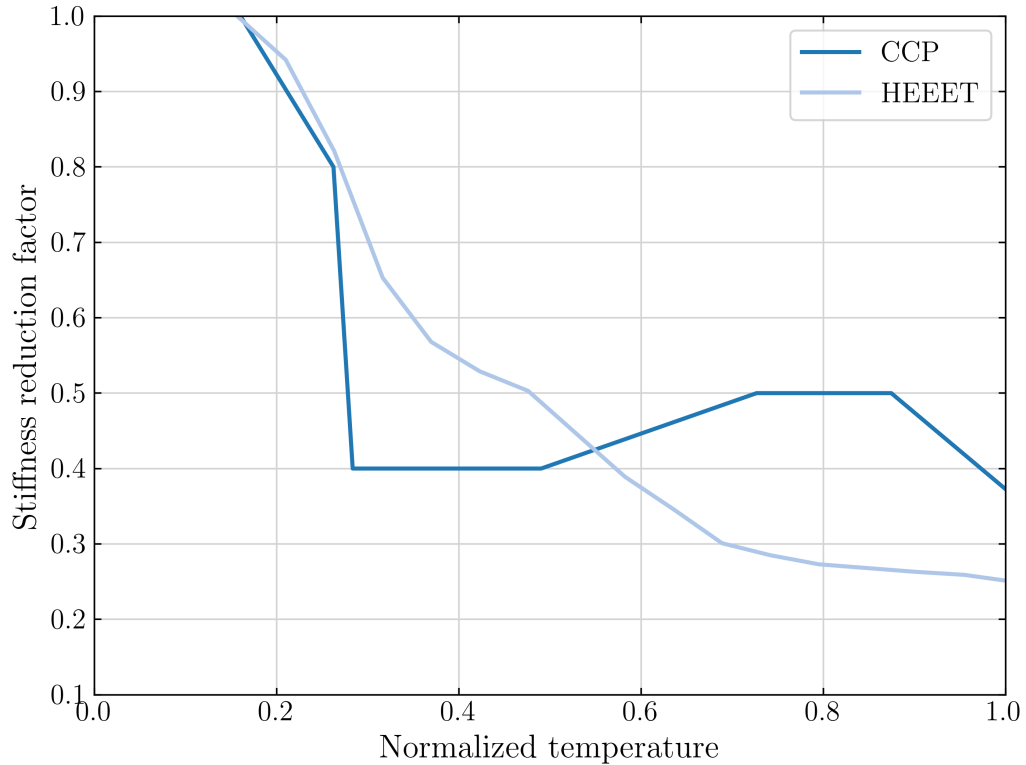
Figure 6.13: Comparison of inferred stiffness reduction factors vs. stiffness reduction factors for CCP.

using the inferred stiffness reduction factors increases to -0.15 compared to -0.1 without accounting for stiffness degradation. At the SG3 location, the monotonicity in the pre-ramp phase has vanished when accounting for stiffness degradation. A similar observation can be made for the SG6 and SG7 locations.

After the load ramp phase, discrepancies between the simulation results using the inferred stiffness and experimental measurements still exist. For the SG3 location, it appears the simulation predictions using the inferred stiffness and constant stiffness are shifted by a constant factor from 38 s to 250 s. For the SG1, SG5, SG6, and SG7 locations, the discrepancy between the two simulation results increases with time. The simulation predictions are again unable to capture the bowlike profile exhibited after 38 s.

It is hypothesized that the bowlike response could be partly attributed not to
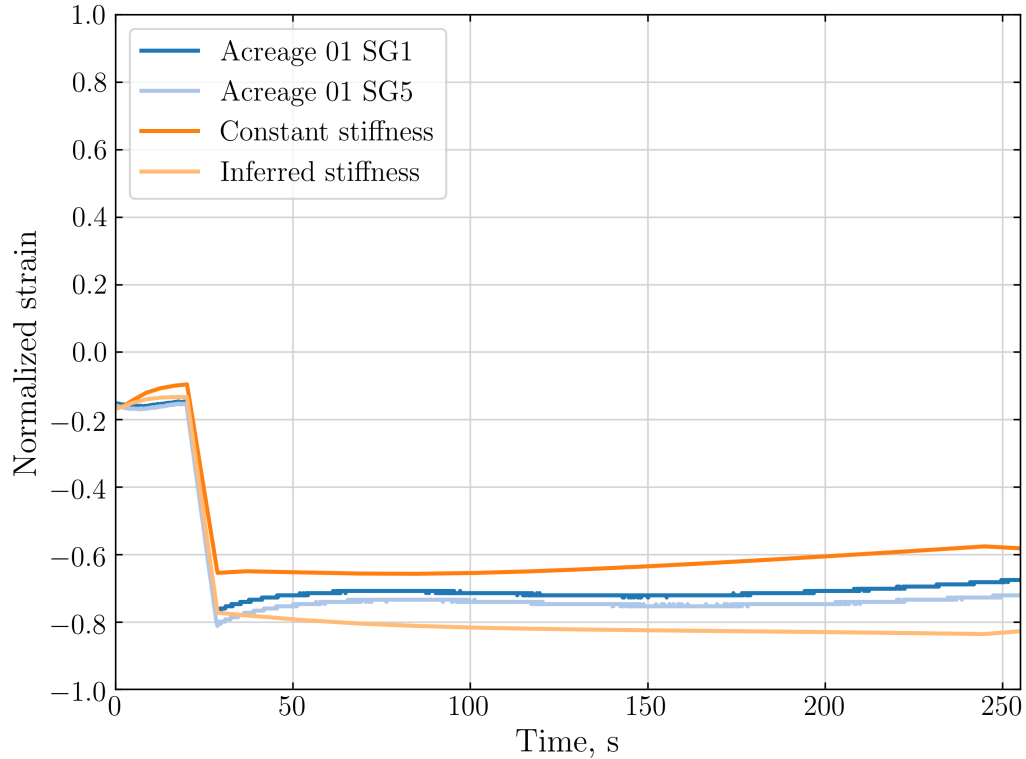
Figure 6.14: Comparison of SG1 and SG5 measurements with predictions using inferred stiffness.

stiffness degradation, but to variations in CTE with temperature. However, inferring CTE as a function of temperature is a very complex problem, even when compared to inferring stiffness. One of the primary difficulties is that HEEET is an orthotropic material, and unlike orthotropic elastic modulus, there are no mathematical relations between each CTE component, so it is an even higher dimensional inference problem. This poses convergence and, more importantly, uniqueness issues when it comes to solving a similar optimization problem for CTE inference.

However, some general statements can be confidently made about CTE behavior at elevated temperatures based on inspecting Figs. 6.14-6.16. First, in the simulation results using an inferred stiffness on the insulation surface, an under-prediction is observed. Physically, the simulation result is suggesting that on the insulation surface, a larger compressive strain in the Warp direction is predicted than is indicated by
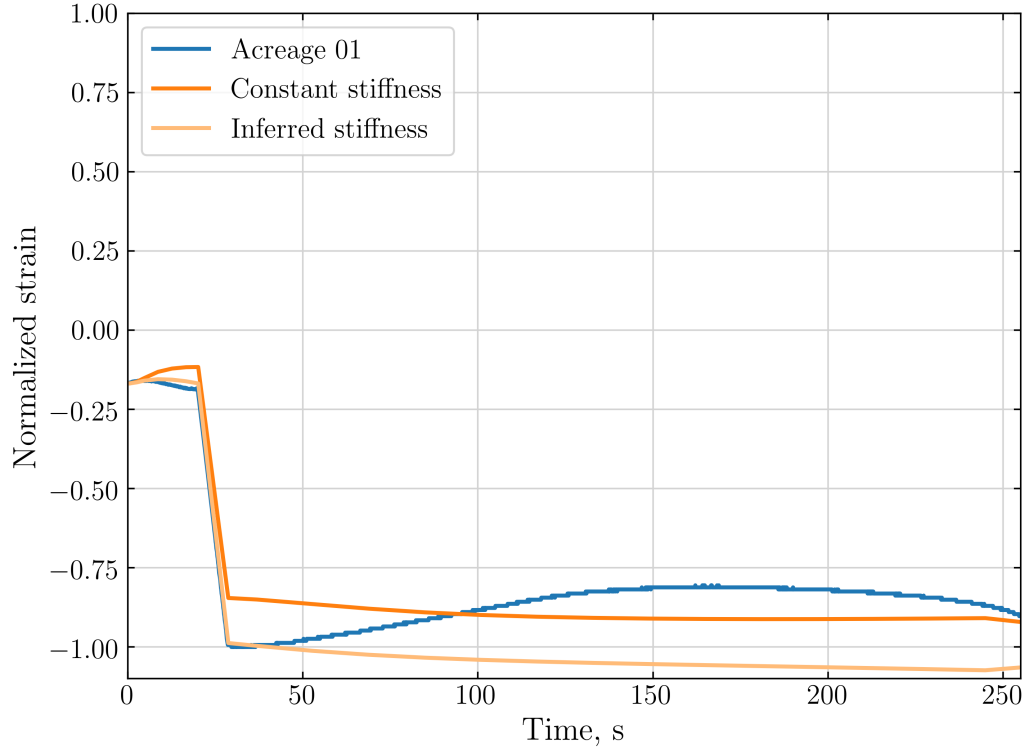
Figure 6.15: Comparison of SG3 measurements with predictions using inferred stiffness.

the SG measurements. Intuitively, increasing the Warp component of the insulation layer material's CTE will result in less compression (or more expansion).

Second, for the recession layer's surface strain response, an over-prediction is observed in the simulation results until approximately 200 s, at which point, an under-prediction is observed. Physically, and for the majority of the after load ramp phase, the simulation result is suggesting that the recession surface is experiencing a larger predicted tensile strain than indicated by the measurements. Decreasing the Warp component of the recession layer material's CTE will result in less expansion. However, a reduction of CTE in the temperature range of interest would be surprising given that the CTE of carbon fiber based materials have been shown to increase with temperature, e.g., in [45]. Given that the discrepancy is relatively small, and that there are experimental uncertainties and asymmetry (e.g., the SG6 and SG7 experimental response exhibit asymmetry), it is further possible that the discrepancy

129
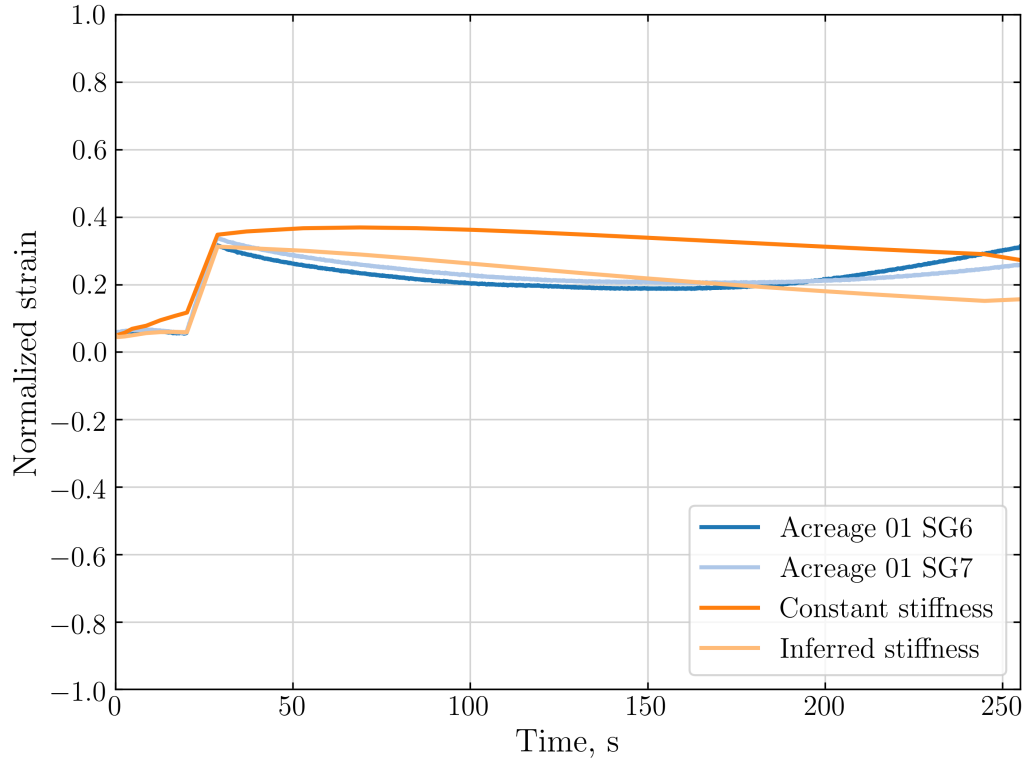
Figure 6.16: Comparison of SG6 and SG7 measurements with predictions using inferred stiffness.

here is not primarily due to a change in CTE with temperature, but again due to experimental uncertainties.

Figures 6.17-6.19 present the normalized experimental strain measurements at the analogous locations for the Acreage 04 panel, which exhibited two load ramp phases. These figures are provided for the purpose of supporting the experimental asymmetry and uncertainty claim. For the measurements on the recession surface, it is clear that there was, again, asymmetry, but also that there was a growing discrepancy between the SG6 and SG7 locations, with the measurements at the latter location failing to exhibit the bowlike response observed in the SG6 location. Based on these results, it is not conclusive if CTE is changing with temperature and if the bowlike response is due to changes in CTE as a function of temperature. Parametric studies of CTE as a function of temperature do not support a bowlike response in the strain predictions.
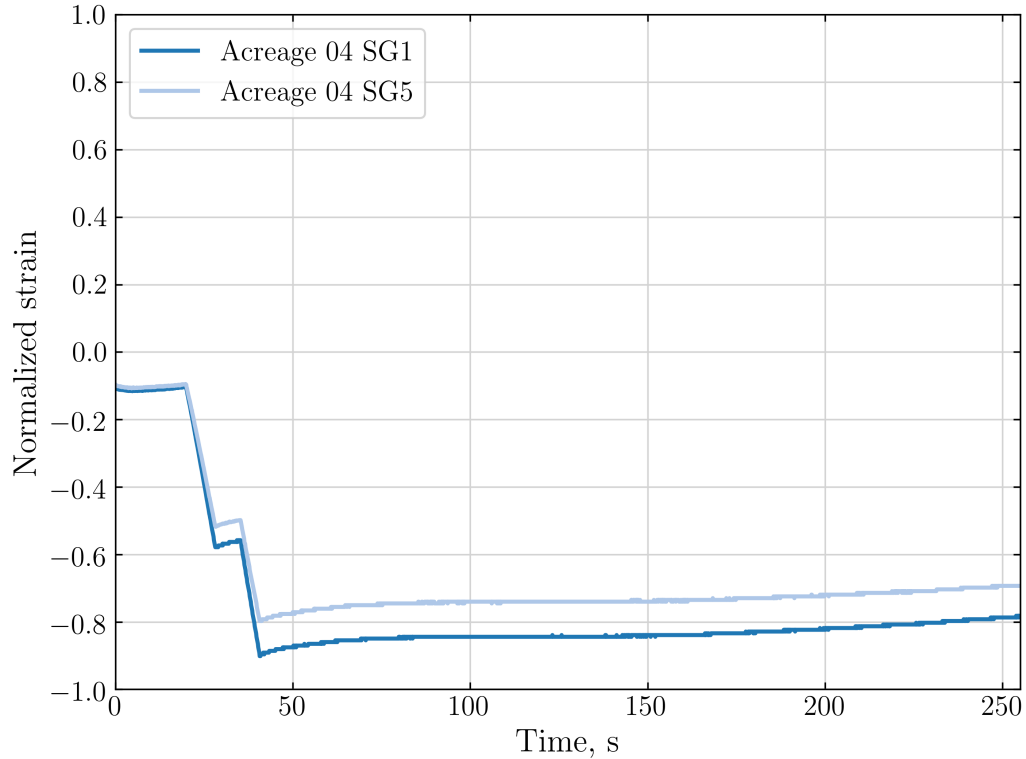
Figure 6.17: Acreage 04 experimental measurements for SG1.

6.4 Chapter Summary

In this Chapter, coupled thermo-structural modeling of the HEEET material is presented. The coupling was performed under a quasi-steady assumption as the structural response of HEEET equilibrates many orders of magnitude faster than that of its thermal response. At the end of each time step, the temperature field computed by Icarus is transferred to the linear elasticity solver for computing the strain and displacement field due to simultaneous thermal and mechanical loading.

Initial studies under a constant stiffness assumption resulted in poor agreement between predictions and measurements. The key takeaway from the initial studies are that stiffness degradation is occurring as the simulation results overpredicted the deformation on the recession and insulation layer surfaces of HEEET.

The next set of studies focused on studying the stiffness degradation of HEEET as it is heated. The are two key takeaways from these studies. First, stiffness degradation
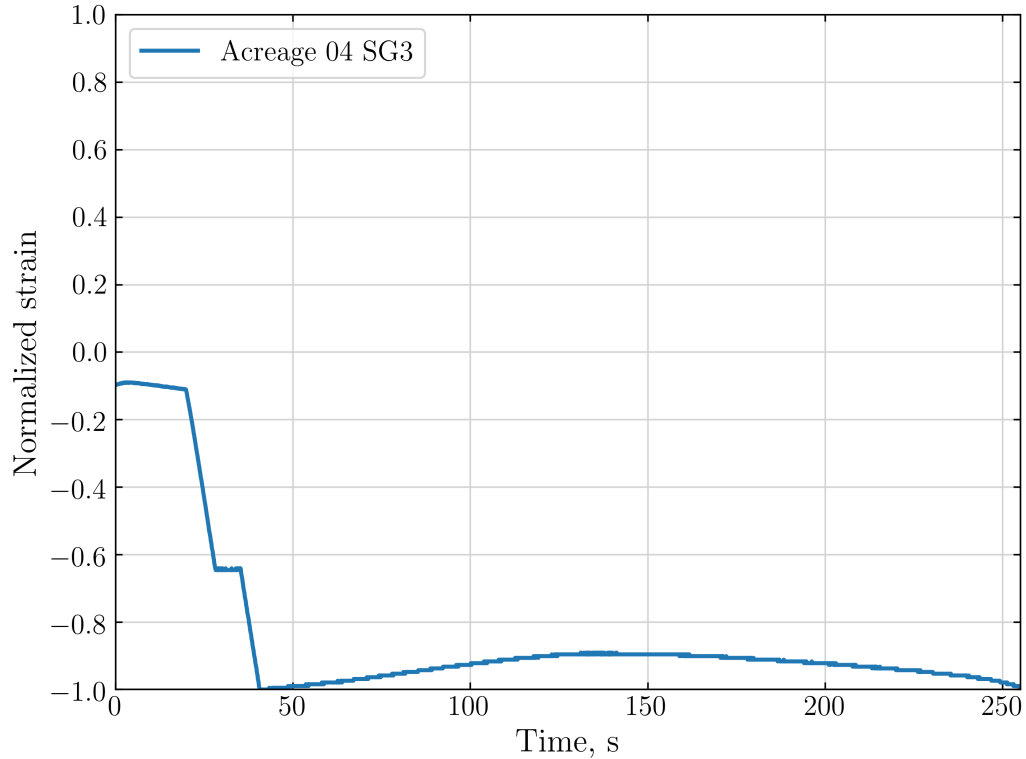
Figure 6.18: Acreage 04 experimental measurements for SG3.

is occurring primarily within the recession layer material, and the inferred stiffness reduction factors, at lower temperatures, are similar to known reduction factors of Carbon Cloth Phenolic (CCP). The inferred factors exhibit a monotonic decrease in stiffness until the radiative equilibrium temperature. Conversely, CCP results indicated that the material stabilizes or increases in stiffness once char temperatures are reached. Second, the experimental measurements are subject to many uncertainties and asymmetries, but these are unlikely to significantly impact the inferred factors.

The primary contribution from these studies are the inferred stiffness reduction factors for HEEET, which provide the TPS community with higher fidelity modeling capability for research and design purposes. As HEEET is widely considered the next generation of TPS for heat intensive planetary exploration missions by NASA, advancing physicochemical modeling capabilities is critical for ensuring mission safety and performance.
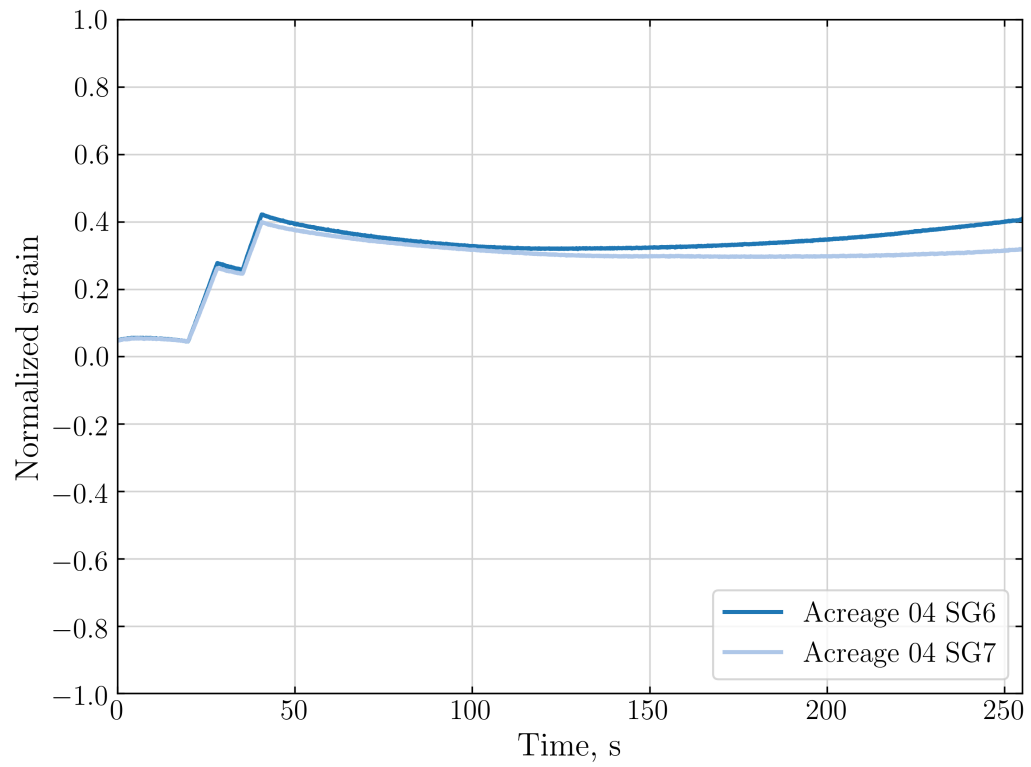
Figure 6.19: Acreage 04 experimental measurements for SG6 and SG7.

CHAPTER VII

Conclusions and Future Work

This chapter sequentially summarizes the results and research presented in the preceding chapters. The latter part of the chapter provides a succinct description of the unique contributions and possible directions for future work.

7.1 Summary

The extreme heating conditions experienced by planetary entry probes or vehicles during atmospheric entry necessitates a well-designed Thermal Protection System (TPS). TPS can be classified as either ablative or non-ablative, with the former class of TPS materials typically used in extreme conditions and the latter in comparatively more benign environments. Ablative TPS was the focus of the research.

For decomposing ablative TPS, the temperature increase results in phase changes and thermochemical removal of material from the surface, which collectively provide the desired relief of heat load to the in-depth material and the underlying vehicle. The internal phenolic resin decomposes at high temperatures through an endothermic process and produces pyrolysis gases that flow through the pores of the TPS displacing the hot boundary layer gas away from the material, and carries some of the internal energy out of the material.

In addition to these thermal-induced effects, structural effects are also important.

Processes such as spallation, cracking, stiffness degradation, and TPS deformation may contribute to mechanical failure or influence thermal performance due to the multi-physics coupling.

The Woven Thermal Protection System (WTPS) concept, the focus of the work, is a relatively new class of ablative TPS, and was introduced in the early 2010s as a mass efficient, tailorable, and effective TPS for future missions with severe heating environments that has performance advantages over traditional TPS materials such as the Phenolic Impregnated Carbon Ablator (PICA) and Heritage Carbon Phenolic (HCP). A WTPS is typically composed of carbon, silica, and/or phenolic yarns woven together in a 3-D or planar architecture with or without resin infusion, allowing for a material with tailorable properties (e.g., thermal conductivity, density, porosity, permeability) and material composition.

The Heatshield for Extreme Entry Environment Technology (HEEET) is, perhaps, the primary NASA technology that makes use of WTPS and is the primary focus of the work in this thesis. The HEEET is a dual-layer WTPS composed of an outer layer designed to be recession-resistant and made from a fine, dense weave of carbon yarns and an inner lower density insulating layer that consists of a blend of carbon and phenolic materials. Both layers are infused with a low density phenolic resin and are mechanically interlocked together multi-dimensionally.

The development cycle of viable TPS uses two critical approaches: experimental testing facilities and simulation modeling tools. Experimental facilities such as arc jets and laser heating facilities (e.g., the Laser Hardened Materials Environmental Laboratory (LHMEL)) were two primary experimental tools used for studying HEEET. Simulation models have the potential to enable a cost-efficient and comprehensive (in terms of modeling capability of multi-physics phenomena) analysis of TPS that is typically not afforded by experimental testing.

The research here focused on the thermal and structural response modeling of

HEEET in a radiant heating environment at the LHMEL facility. The experimental measurements served as validation data sets for assessing the performance of the simulation models and for inferring material properties.

The structural response modeling was performed using a finite volume linear elasticity solver developed as part of the dissertation that supports Dirichlet, Neumann, and Mixed boundary conditions. The assumption that WTPS behaves linearly and elastically is a reasonable assumption based on tensile testing and small deformations expected during usage. The cell-centered displacement gradients in the linear elasticity solver is computed using least squares. The resulting discretization results in a sparse linear system that were solved using the generalized minimal residual method with a geometric algebraic multigrid preconditioner.

The thermal response modeling was performed using Icarus, a 3-D material response code under development at the NASA Ames Research Center. Icarus uses an unstructured finite-volume discretization of the conservation equations governing the in-depth heat transfer and solid material decomposition within a decomposing material. The energy equation is the classical transient heat conduction equation with the addition of a non-linear convective term for modeling pyrolysis gas transport. A three-component Arrhenius-based decomposition model was used for HEEET. Temperature-dependent properties of HEEET were linearly interpolated between its virgin and char states.

The thermo-structural coupling was performed under a quasi-steady assumption, with the suitability of the assumption governed by Boley's number being much greater than unity. For HEEET and the environmental conditions, Boley's number was determined to be $\mathcal{O}\left(10^3\right)$, validating the use of the quasi-steady coupling. In the quasi-steady approach, the temperature field was computed by Icarus and transferred to the linear elasticity solver to compute deformation due to simultaneous mechanical and thermal loading.

As the linear elasticity and Icarus solvers are relatively new, verification of the solvers were necessary to ensure that the governing equations are being solved correctly. For the linear elasticity solver, convergence and order of accuracy analyses were conducted through comparisons with classical problems (e.g., cantilever beam deflection) with known analytical solutions and through a more comprehensive Method of Manufactured Solutions (MMS) analysis. The verification studies showed that the solver was approximately second order accurate, spatially, and that the numerics were implemented correctly. For Icarus, comparisons with FIAT, a well-established 1-D material response code, on a HEEET sample under representative LHMEL conditions showed that the two solvers were in close agreement, verifying that the numerics in Icarus relevant for the research were implemented correctly.

The remaining three chapters focused on presenting the thermal, structural, and coupled thermo-structural analyses of the HEEET in the LHMEL environment, respectively. The experiments conducted in the LHMEL facility provided a rich suite of experimental data for evaluating the thermal, structural, and coupled thermo-structural modeling. In the LHMEL facility, the HEEET panels were tested inside a vacuum chamber. For the thermal testing, a 20 kW fiber laser was used either at full or half power to heat the recession layer in the vicinity of the centerline under a CO_2 purge. The CO_2 purge was employed to ensure a chemically inert environment as surface ablation was not desired in the testing. A four-point-bending apparatus was installed within the vacuum chamber to apply mechanical loading to the HEEET panel. Thermocouples (TCs), strain gauges (SGs), and Linear Variable Differential Transformers (LVDTs) were used to measure internal temperature and surface deformation.

Icarus was used for the thermal analyses. A radiative heat flux boundary condition was applied on the surface of direct laser exposure. The remaining surfaces were either adiabatic or free to reradiate. Initial comparisons between simulation re-

sults and measurements indicated that the magnitude and uniformity of the radiative heat flux boundary condition resulted in predictions that underestimated top-level TC measurements within the vicinity of the centerline and overestimated at further off-center locations. The comparisons necessitated a reconstruction of the magnitude and spatial distribution of the heat flux boundary condition, where it was shown that a 20% increase in the centerline heat flux and a supergaussian profile resulted in much improved agreement between simulation results and measurements. However, comparisons showed that, at deeper TC locations, the agreement was poor. The reason was hypothesized to be that the material model, particularly the temperature dependent orthotropic thermal conductivity, used was not representative of the current HEEET material and environmental conditions. A Particle Swarm Optimization (PSO) optimization strategy was used to infer the temperature-dependent orthotropic thermal conductivity of HEEET. The inference showed that a 20-40% and 50% reduction in char and virgin conductivity from the initial properties in the Through the Thickness (TTT) and In Plane (IP) directions were necessary to achieve improved agreement. The inferred properties were used to model a separate HEEET panel under a higher heating condition to cross-validate the inferred properties. Results indicated that by using the inferred properties, the Mean Squared Error (MSE) between the simulation results and measurements generally decreased by approximately an order of magnitude.

In the initial structural response modeling of HEEET at room temperature, stiffness properties derived from a HEEET panel manufactured from a 13 in. weave were used. However, the panels tested in recent experimental testing of HEEET were manufactured from a 24 in. tighter weave, which was hypothesized to be stiffer. Initial comparisons between simulation results and measurements validated the hypothesis as the simulation response indicated significantly larger deformations on the recession layer surface than exhibited by the measurements. Comparisons for the response on

the insulation surface indicated acceptable agreement. An inverse analysis showed that increasing the stiffness of the recession and insulation layers by 130% and 10% resulted in simulation predictions that achieved the best agreement with measurements.

The final results chapter focused on coupled thermo-structural modeling. The HEEET specimen was subjected to combined four-point-bending mechanical and thermal loading. Initial studies under the assumption that stiffness is temperature-independent (i.e., no stiffness degradation) resulted in poor agreement between predictions and measurements. It was evident from the comparisons that stiffness degradation was occurring as the simulation results showed that the material deformed less than indicated by the measurements. Stiffness degradation studies showed that the HEEET stiffness decreased monotonically with temperature in the temperature range studied. At the higher end of the temperature range, the stiffness appeared to be asymptotically converging; however, it is not conclusive from the current studies whether HEEET truly converges at higher temperatures, or if, perhaps, HEEET could exhibit an increase in stiffness at higher temperatures. The stiffness reduction factors for HEEET were compared with stiffness reduction factors for Carbon Cloth Phenolic (CCP), which is a similar material to HEEET, but with notable differences. The comparisons showed that at lower temperatures, the behavior of HEEET and CCP were similar, but the (REDACTED FOR NOW)The observation was expected to be attributed to the known differences between the two materials.

Substantial progress on modeling WTPS was made in this work, but there remains important challenges such as uncertainties of properties outside of the heating rates and temperature range modeled. From the results, it appeared that fundamental material properties have changed in different HEEET weaves, which is an important consideration for future manufacturing of HEEET weaves. The LHMEL experimental results were critical for inferring the stiffness reduction factors from a macroscopic

139

analysis. A more ideal experiment for inference could involve additional testing of HEEET at different heating rates, different environments, and higher temperatures, which would be more comprehensive for model validation and material property inference.

7.2 Contributions

The major objective of this dissertation was to model HEEET in pure thermal, structural, and combined thermo-structural environments, to compare the results with experimental measurements, and to improve the modeling based on the comparisons. The unique research contributions can be succinctly described as

- Development of a structural response and coupled thermo-structural response simulation software tailored for modeling WTPS: An anisotropic linear elasticity model was implemented within a thermal response solver and was developed, verified, and assessed to model WTPS.

- Inferring room temperature stiffness properties: The linear elasticity solver was used to infer room temperature stiffness properties of a 24 in. weave that were not previously available. The simulation results when using the inferred properties demonstrated excellent agreement with experimental measurements on a HEEET panel that was not used for inference, alleviating the concerns for overfitting to data used for inference.

- Improved material model for HEEET: The Icarus thermal response solver was used to model HEEET in a radiant heating environment. The solver was further used to infer the temperature-dependent orthotropic virgin and char thermal conductivity of the recession and insulation layers of HEEET. When using the inferred properties, agreement between simulation results and measurements for in-depth temperature generally improved by at least 90%.

- Developed stiffness degradation model for HEEET: The Icarus and linear elasticity solvers were used to model HEEET under combined mechanical and thermal loading conditions. The modeling results produced a stiffness degradation model that, when used to model HEEET, resulted in predictions that agree much better with experimental measurements.

All of these contributions are useful in informing WTPS design, research, and experimental efforts, in particular, the design of HEEET for future space exploration missions.

7.3   Future Work

The thermal response modeling of the HEEET ignored the effects of pyrolysis gas transport as it was expected to be minimal based on the HEEET being a very low porous material and the uncertainties in the permeability. Future work could focus on microscale modeling to determine the permeability of HEEET and assess the degree to which pyrolysis gas transport affects the thermal response in the macroscopic model. Parametric studies of different levels of resin infusion could be performed to assess the relationship between the level of resin infusion and reduction in temperature to better guide future design efforts.

Another area for future work is to model HEEET under disparate heating conditions. A historical challenge in TPS modeling is attributed to the uncertainties in the char properties of the TPS material. The uncertainty is primarily a result of the heating conditions and environment, where the same material at the same temperature can exhibit different properties under different heating rates and environments. While the temperature-dependent thermal conductivity inferred in this work was shown to extrapolate with confidence to a higher heating rate, it is possible that the extrapolation may become poorer in more extreme environments. Experimental and ensuing

simulation validation studies should be performed to assess the inferred properties at more extreme heating rates. If the assessment indicates that the inferred properties do not extrapolate well to more extreme heating rates, then a heating rate-dependent model is another possible direction for future work.

A unique aspect of this dissertation is the focus on modeling WTPS, where there is currently limited studies in the literature. The focus here was on HEEET as it is the primary TPS that makes use of WTPS and the availability of experimental measurements for model validation; however, other NASA technology developmental efforts such as the Adaptive Deployable Entry Placement Technology (ADEPT) and 3-D Multifunctional Ablative TPS (3D-MAT) also use WTPS. Modeling these two systems under combined thermo-structural conditions would better inform the overall effort of increasing the fidelity of WTPS modeling.

From a model validation perspective, the LHMEL experimental results were limited. Dedicated experiments could be performed that are specifically designed to provide data for model validation; however, there still remains the challenge of ensuing the model input parameters (e.g., boundary conditions, material properties) are accurate and representative of the tested material and conditions. A comprehensive approach could entail an iterative process between the inference of input parameters and model validation, with dedicated experiments designed for each task.

Exploring stiffness degradation at a higher temperature range is another direction for future work aligned with the preceding suggestion. Due to the absence of experimental measurements at greater temperatures, it is not conclusive from the current studies how HEEET degrades at even greater temperatures. It is possible that the monotonicity would disappear at higher temperatures or asymptoticity would be observed.

Lastly, for NASA to rely on simulation tools for the design of heatshields using WTPS, simultaneous modeling of the flowfield, gas-surface interactions, and material

response is needed. To date, there has been no research conducted for WTPS in a fully coupled environment. The development of a fully coupled model remains a challenge in the TPS modeling community, but is a critical step in developing simulation tools of the highest fidelity.

BIBLIOGRAPHY

BIBLIOGRAPHY

[1] E. Venkatapathy, Modern advances in ablative tps, International Planetary Probe Workshop 10, San Jose, CA, 2013.
URL https://ntrs.nasa.gov/citations/20140000871

[2] B. Laub, E. Venkatapathy, Thermal protection system technology and facility needs for demanding future planetary missions, International Workshop on Planetary Probe Atmospheric Entry and Descent Trajectory Analysis and Science, Noordwijk, Netherlands, 2004.
URL http://adsabs.harvard.edu/full/2004ESASP.544..239L

[3] J. D. Feldman, E. Venkatapathy, C. Wilkinson, K. J. Mercer, Development of an Ablation 3D Quartz/Cyanate Ester Composite for the Orion Spacecraft Compression Pad, in: SAMPE TP15-0195, The Composites and Advanced Materials Expo (CAMX), Dallas, TX, 2015.
URL https://ntrs.nasa.gov/archive/nasa/casi.ntrs.nasa.gov/20190002016.pdf

[4] D. Ellerby, T. Boghozian, D. Driver, J. Chavez-Garcia, M. Fowler, P. Gage, M. Gasch, G. G., C. Kazemba, C. Kellermann, S. Langston, J. Ma, M. Mahzari, Heatshield for extreme entry environment technology (heeet) development and maturation status, Tech. Rep. 20180001478, NASA, Moffett Field, California (2018).

[5] E. Venkatapathy, K. Hamm, I. Fernandez, J. Arnold, D. Kinney, B. Laub, A. Makino, M. McGuire, K. Peterson, D. Prabhu, D. Empey, I. Dupzyk, L. Huynh, P. Hajela, P. Gage, A. Howard, D. Andrews, Adaptive Deployable Entry and Placement Technology (ADEPT): A Feasibility Study for Human Missions to Mars. arXiv:https://arc.aiaa.org/doi/pdf/10.2514/6.2011-2608, doi:10.2514/6.2011-2608.

[6] F. S. Milos, Y.-K. Chen, M. Mahzari, Arcjet tests and thermal response analysis for dual-layer woven carbon phenolic, Journal of Spacecraft and Rockets 55 (3) (2018) 712–722. doi:10.2514/1.A34142.

[7] A. Ellerby, E. Venkatapathy, P. Gage, M. Stackpoole, M. Gasch, K. Petersen, Z. Young, K. C., M. M., O. Nishioka, P. C., S. Splinter, S. Langston, C. Kellerman, J. Williams, D. Prabhu, B. Libben, F. Milos, M. Fowler, D. Driver, G. Palmer, G. Gonzales, E. Boghozian, J. Chavez-Garcia, R. Miller, A. Murphy,

K. Boston, J. Beverly, E. Frye, W. Geouge, K. Mclain, J. O'Connell, T. O'Neil, G. Shanks, M. Thornblom, J. Tury, K. Bloxom, D. Duncan, W. Johnston, L. O'Donnell, M. Roth, S. Walker, Heatshield for extreme entry environment technology (heeet) thermal protection system (tps), Tech. Rep. ARC-E-DAA-TN69963, NASA, Moffett Field, CA 94035 (September 2019).
URL https://ntrs.nasa.gov/api/citations/20190031964/downloads/20190031964.pdf

[8] A. Martin, L. C. Scalabrin, I. D. Boyd, High performance modeling of atmospheric re-entry vehicles, Journal of Physics: Conference Series 341 (1) (2012) 012002. doi:10.2514/1.T4202.

[9] D. Brownlee, The stardust mission: Analyzing samples from the edge of the solar system, Annual Review of Earth and Planetary Sciences 42 (1) (2014) 179–205. arXiv:https://doi.org/10.1146/annurev-earth-050212-124203, doi:10.1146/annurev-earth-050212-124203.
URL https://doi.org/10.1146/annurev-earth-050212-124203

[10] J. P. Grotzinger, J. Crisp, A. R. Vasavada, et al., Mars science laboratory mission and science investigation, Space Science Review 170 (1) (2012) 5–56. arXiv:https://doi.org/10.1146/annurev-earth-050212-124203, doi:10.1007/s11214-012-9892-2.
URL https://doi.org/10.1146/annurev-earth-050212-124203

[11] F. S. Milos, Y.-K. Chen, Ablation and thermal response property model validation for phenolic impregnated carbon ablator, Journal of Spacecraft and Rockets 47 (5) (2010) 786–805. doi:10.2514/1.42949.

[12] H. Alkandry, I. D. Boyd, A. Martin, Coupled flow field simulations of charring ablators with nonequilibrium surface chemistry, in: 44th AIAA Thermophysics Conference, 2013, p. 2634. doi:10.2514/6.2013-2634.

[13] F. S. Milos, Y.-K. Chen, Ablation, thermal response, and chemistry program for analysis of thermal protection systems, Journal of Spacecraft and Rockets 50 (1) (2013) 137–149. doi:10.2514/1.A32302.

[14] A. Riccio, F. Raimondo, A. Sellitto, V. Carandente, R. Scigliano, D. Tescione, Optimum design of ablative thermal protection systems for atmospheric entry vehicles, Applied Thermal Engineering 119 (2017) 541–552. doi:10.1016/j.applthermaleng.2017.03.053.

[15] F. S. Milos, Galileo probe heat shield ablation experiment, Journal of Spacecraft and Rockets 34 (6) (1997) 705–713. doi:10.2514/2.3293.

[16] J. T. Needels, P. J. Gage, D. T. Ellerby, E. Venkatapathy, K. H. Peterson, J. C. V. Kam, Application of Risk Informed Decision Making to a Highly Reliable Three Dimensionally Woven Thermal Protection System for

Mars Sample Return. arXiv:https://arc.aiaa.org/doi/pdf/10.2514/6.2020-0709, doi:10.2514/6.2020-0709.

[17] R. Mattingly, L. May, Mars sample return as a campaign, in: 2011 Aerospace Conference, 2011, pp. 1–13. doi:10.1109/AERO.2011.5747287.

[18] D. Z. Dang, E. C. Stern, I. D. Boyd, Structural response modeling of a woven thermal protection system, Journal of Thermophysics and Heat Transfer 0 (0) (0) 1–8. arXiv:https://doi.org/10.2514/1.T6051, doi:10.2514/1.T6051.
URL https://doi.org/10.2514/1.T6051

[19] P. G. Cross, I. D. Boyd, Two-dimensional modeling of ablation and pyrolysis with application to rocket nozzles, Journal of Spacecraft and Rockets 54 (1) (2017) 212–224. doi:10.2514/1.A33656.

[20] Y.-K. Chen, F. S. Milos, Ablation and thermal response program for spacecraft heatshield analysis, Journal of Spacecraft and Rockets 36 (3) (1999) 475–483. doi:10.2514/2.3469.

[21] A. Martin, I. D. Boyd, Non-darcian behavior of pyrolysis gas in a thermal protection system, Journal of Thermophysics and Heat Transfer 24 (1) (2010) 60–68. doi:10.2514/1.44103.

[22] L. Scalabrin, I. Boyd, Numerical Simulation of Weakly Ionized Hypersonic Flow for Reentry Configurations. arXiv:https://arc.aiaa.org/doi/pdf/10.2514/6.2006-3773, doi:10.2514/6.2006-3773.

[23] M. J. Wright, G. V. Candler, D. Bose, Data-parallel line relaxation method for the navier-stokes equations, AIAA Journal 36 (9) (1998) 1603–1609. doi:10.2514/2.586.

[24] G. V. Candler, H. B. Johnson, I. Nompelis, V. M. Gidzak, P. K. Subbareddy, M. Barnhardt, Development of the US3D Code for Advanced Compressible and Reacting Flow Simulations. arXiv:https://arc.aiaa.org/doi/pdf/10.2514/6.2015-1893, doi:10.2514/6.2015-1893.
URL https://arc.aiaa.org/doi/abs/10.2514/6.2015-1893

[25] J. C. Schulz, E. C. Stern, G. E. Palmer, H. J. B., Icarus user manual: Release v1.2.0, (in press) NASA/TP-2020-220510, NASA Ames Research Center (2020).

[26] R. Fu, H. Weng, J. F. Wenk, A. Martin, Thermomechanical coupling for charring ablators, Journal of Thermophysics and Heat Transfer 32 (2) (2018) 369–379. doi:10.2514/1.T5194.

[27] R. Fu, H. Weng, J. F. Wenk, A. Martin, Thermal expansion for charring ablative materials, Journal of Thermophysics and Heat Transfer 34 (1) (2020) 57–65. doi:10.2514/1.T5718.

[28] K. W. Morton, E. Suli, Finite Volume Methods and their Analysis, IMA Journal of Numerical Analysis 11 (2) (1991) 241–260. doi:10.1093/imanum/11.2.241.

[29] S. Balay, S. Abhyankar, M. F. Adams, J. Brown, P. Brune, K. Buschelman, L. Dalcin, V. Eijkhout, W. D. Gropp, D. Kaushik, M. G. Knepley, D. A. May, L. C. McInnes, R. T. Mills, T. Munson, K. Rupp, P. Sanan, B. F. Smith, S. Zampini, H. Zhang, H. Zhang, PETSc users manual, Tech. Rep. ANL-95/11 - Revision 3.9, Argonne National Laboratory (2018).
URL http://www.mcs.anl.gov/petsc

[30] C. Moyer, R. Rindal, An analysis of the coupled chemically reaction boundary layer and charring ablator, Tech. rep., National Aeronautics and Space Administration (1968).

[31] A. Amar, Modeling of one-dimensional ablation with porous flow using finite control volume procedure, Ph.D. thesis, North Carolina State University (2006).

[32] A. J. Amar, B. F. Blackwell, J. R. Edwards, Development and verification of a one-dimensional ablation code including pyrolysis gas flow, Journal of Thermophysics and Heat Transfer 23 (1) (2009) 59–71. arXiv:https://doi.org/10.2514/1.36882, doi:10.2514/1.36882.
URL https://doi.org/10.2514/1.36882

[33] B. A. Boley, Approximate Analyses of Thermally Induced Vibrations of Beams and Plates, Journal of Applied Mechanics 39 (1) (1972) 212–216. doi:10.1115/1.3422615.

[34] W. Nowacki, Progress in Thermoelasticity, Applied mechanics series, Państw. Wyd. nauk., 1969.
URL https://books.google.com/books?id=l64hAQAAIAAJ

[35] K. Salari, P. Knupp, Code Verification by the Method of Manufactured Solutions, Tech. rep., Sandia National Laboratories (06 2000).

[36] R. Suliman, O. F. Oxtoby, A. G. Malan, S. Kok, An enhanced finite volume method to model 2d linear elastic structures, Applied Mathematical Modeling 38 (7-8) (2014) 2265–2279. doi:10.1016/j.apm.2013.10.028.

[37] S. P. Timoshenko, G. N. Goodier, Theory of Elasticity, McGraw-Hill, 1970. doi:10.1017/S036839310012471X.

[38] E. Ellerby, Overview of heatshield for extreme entry environment technology (heeet), Tech. Rep. ARC-E-DAA-TN73549, NASA Ames Research Center (2019).
URL https://ntrs.nasa.gov/archive/nasa/casi.ntrs.nasa.gov/20190031969.pdf

[39] M. Mahzari, R. D. Braun, Time-dependent mars entry aeroheating estimation from simulated in-depth heat shield temperature measurements, Journal of Thermophysics and Heat Transfer 27 (3) (2013) 435–446. doi:10.2514/1.T3986.

[40] A. R. Conn, K. Scheinberg, L. N. Vicente, Introduction to Derivative-Free Optimization, Society for Industrial and Applied Mathematics, USA, 2009. doi:10.1137/1.9780898718768.

[41] J. Kennedy, R. Eberhart, Particle swarm optimization, in: Proceedings of ICNN'95 - International Conference on Neural Networks, Vol. 4, 1995, pp. 1942–1948 vol.4. doi:10.1109/ICNN.1995.488968.

[42] J. Snoek, H. Larochelle, R. P. Adams, Practical bayesian optimization of machine learning algorithms, in: F. Pereira, C. J. C. Burges, L. Bottou, K. Q. Weinberger (Eds.), Advances in Neural Information Processing Systems 25, Curran Associates, Inc., 2012, pp. 2951–2959.
URL http://papers.nips.cc/paper/4522-practical-bayesian-optimization-of-machine-learning-algorithms.pdf

[43] T. Hastie, R. Tibshirani, J. Friedman, The Elements of Statistical Learning, Springer Series in Statistics, Springer New York Inc., New York, NY, USA, 2001. doi:10.1007/978-0-387-84858-7.

[44] R. Kohavi, A Study of Cross-Validation and Bootstrap for Accuracy Estimation and Model Selection, Vol. 2, 1995, pp. 1137–1145.
URL https://dl.acm.org/doi/10.5555/1643031.1643047

[45] C. Pradere, C. Sauder, Transverse and longitudinal coefficient of thermal expansion of carbon fibers at high temperatures (300–2500k), Carbon 46 (14) (2008) 1874 – 1884. doi:https://doi.org/10.1016/j.carbon.2008.07.035.
URL http://www.sciencedirect.com/science/article/pii/S0008622308003837